QUEENSLAND UNIVERSITY OF TECHNOLOGY

SCHOOL OF PHYSICAL AND CHEMICAL SCIENCES

IMAGING AND RADIATION INTERACTIONS OF POLYMER GEL DOSIMETERS

Submitted by Jamie Vincent Trapp to the School of Physical and Chemical Sciences, Queensland University of Technology in partial fulfilment of the requirements of the degree of Doctor of Philosophy

March, 2003

Keywords

X-ray computed tomography

Gel dosimetry

Radiotherapy

Image processing

Uncertainty

Linear attenuation coefficient

Abstract

Aim

The past two decades have seen a large body of work dedicated to the development of a three dimensional gel dosimetry system for the recording of radiation dose distributions in radiation therapy. The purpose of much of the work to date has been to improve methods by which the absorbed dose information is extracted. Current techniques include magnetic resonance imaging (MRI), optical tomography, Raman spectroscopy, x-ray computed tomography (CT) and ultrasound. This work examines CT imaging as a method of evaluating polymer gel dosimeters.

Apart from publications resulting from this work, there has been only two other journal articles to date reporting results of CT gel dosimetry. This indicates that there is still much work required to develop the technique. Therefore, the aim of this document is to develop CT gel dosimetry to the extent that it is of use to clinical and research physicists.

Scope

Each chapter in this document describes an aspect of CT gel dosimetry which was examined; with Chapters 2 to 7 containing brief technical backgrounds for each aspect. Chapter 1 contains a brief review of gel dosimetry.

The first step in the development of any method for reading a signal is to determine whether the signal can actually be obtained. However, before polymer gel dosimeters can be imaged using a CT scanner, imaging techniques are required which are employable to obtain reliable readings. Chapter 2 examines the various artifacts inherent in CT which interfere with the quantitative analysis of gel dosimeters and a method for their removal is developed. The method for artifact reduction is based on a subtraction technique employed previously in a feasibility study and a system is designed to greatly simplify the process. The

simplification of the technique removes the requirement for accurate realignment of the phantom within the scanner and the imaging of calibration vials is enabled.

Having established a method by which readings of polymer gel dosimeters can be obtained with CT, Chapter 3 examines the CT dose response. A number of formulations of polymer gel dosimeter are studied by varying the constituent chemicals and their concentrations. The results from this chapter can be employed to determine the concentration of chemicals when manufacturing a polymer gel dosimeter with a desired CT dose response.

With the CT dose response characterised in Chapter 3, the macroscopic cause of the CT signal is examined in Chapter 4. To this end direct measurement of the linear attenuation coefficient is obtained with a collimated radiation source and detector. Density is measured by Archimedes' principle. Comparison of the two results shows that the cause of the CT signal is a density change and the implications for polymer gel dosimetry are discussed.

The CT scanner is revisited in Chapter 5 to examine the CT imaging techniques required for optimal performance. The main limitation of the use of CT in gel dosimetry to date has been image noise. In Chapter 5 stochastic noise is investigated and reduced. The main source of non-stochastic noise in CT is found and imaging techniques are examined which can greatly reduce this residual noise. Predictions of computer simulations are verified experimentally.

Although techniques for the reduction of noise are developed in Chapter 5, there may be situations where the noise must be further reduced. An image processing algorithm is designed in Chapter 6 which employs a combination of commonly available image filters. The algorithm and the filters are tested for their suitability in gel dosimetry through the use of a simulated dose distribution and by performing a pilot study on an irradiated polymer gel phantom.

Having developed CT gel dosimetry to the point where a suitable image can be obtained, the final step is to investigate the uncertainty in the dose calibration. Methods used for calibration uncertainty in MRI gel dosimetry to date have either assumed a linear response up to a certain dose, or have removed the requirement for linearity but incorrectly ignored the reliability of the data and

fit of the calibration function. In Chapter 7 a method for treatment of calibration data in CT gel dosimetry is proposed which allows for non-linearity of the calibration function, as well as the goodness of its fit to the data. Alternatively, it allows for the reversion to MRI techniques if linearity is assumed in a limited dose range.

Conclusion

The combination of the techniques developed in this project and the newly formulated normoxic gels (not extensively studied here) means that gel dosimetry is close to becoming viable for use in the clinic. The only capital purchase required for a typical clinic is a suitable water tank, which is easily and inexpensively producible if the clinic has access to a workshop.

Table of Contents

List of Figures

Statement of Original Authorship

The work contained in this thesis has not been previously submitted for a degree or diploma at any other higher education institution. To the best of my knowledge and belief, the thesis contains no material previously published or written by another person except where due reference is made.

Signed: _____

Date: _____

Acknowledgments

First of all I would like to acknowledge the support of my supervisor, Dr Greg Michael. Greg's approachability and common sense ensured that I was freely able to express solutions to various problems without fear of ridicule, even when they initially sounded quite 'harebrained'. His scientific aptitude, intelligence and broadmindedness enabled him to immediately see the value of these ideas which were subsequently developed and resulted in some of the major achievements of this project. Rather than dictating what each step in my research would be, he respected my ability to steer the project in directions of my own and gave me the freedom to do so, resulting in my acquisition of valuable scientific skills. His value as a teacher is bourn out by the fact that he gave me the flexibility to alter the project for the sake of my own personal development, for example, the achievements of Chapter 4 originated from my desire to obtain more experience in instrumentation and although it was a change in direction he not only allowed it, but encouraged me. Greg is the type of supervisor who is too rare – one who teaches students to think independently.

The second person I would like to acknowledge is my associate supervisor, Dr Clive Baldock. As an associate supervisor Clive has had a much greater involvement in my project than would be expected. He is a very driven and enthusiastic person who is always striving for results and 'more papers'. His enthusiasm resulted in faster progress of my project in the gel dosimetry portions and he has taught me much about the publication and presentation of results. I appreciate the extra effort he has put into my project, which is not expected from an associate supervisor. I must state that I always dread answering the phone and hearing (in an English accent) "I've read the latest draft of the paper and I've got a few changes I'd like you to make….."

I would also like to thank the various members of the Radiotherapy research group at QUT. These include the postdoctoral research fellows Dr Sven Back and Dr Martin Lepage who invested their time and energy teaching me about gel dosimetry and, more importantly, scientific methodology early in the

project. I also thank Melissa Mather, Tony Venning and Chris Hurley for their moral and professional support, Mangala Jayasekera for giving up his spare time to show me how to make gels, and Dr Yves De Deene for various advice.

I thank Bob Organ, David Pitt and Jim Drysdale from the QUT Faculty of Science Workshop for their excellent workmanship in construction of various apparatus during the project. It should be stated that the workshop is one of the most important components of the faculty, as most of the scientific research could not be completed without the various strange looking apparatus produced down in the basement. If a single research group within the faculty stopped operating there might not be a significant effect on the other groups, however if the workshop stopped operating most of the research groups within the faculty would be crippled.

I thank the numerous other people who have also provided support during the project. These people include George Kolouris, Jaya Dharmasiri, Damon Bennett, Nick Menzies, Kym Nitschke, Brian Thomas, Riaz Akber, Brendan Healey, Phil Back, Elizabeth Stein and any others who I may have missed. These people freely and generously gave the time out of their working day to assist me with access to equipment or to give advice. I also acknowledge the various institutions who allowed me to use their equipment, namely Queensland Radium Institute (Princess Alexandria Hospital, Mater Hospital and Royal Brisbane Hospital), Queensland X-ray (Mater Private Hospital), University of Queensland, and Wesley Hospital.

Finally, I would like to thank my parents who have supported me in many ways since I decided, seven years ago, to leave a ‘good’ job and start university, at 28 years of age, in a field of study of which they’d never heard. I should state that, like most physicists, I am still unsuccessful in explaining to my parents what a physicist does.

Chapter 1: Introduction

Modern radiotherapy techniques such as stereotactic radiosurgery and intensity modulated radiotherapy are designed to deliver highly conformal radiation doses to tumours whilst sparing nearby sensitive tissues from overly large doses. To verify the accuracy of these techniques the radiation dose distribution must be measured. Dosimeters currently in use, such as ionization chambers and thermoluminescent devices have limitations in that they only measure the dose at a point, and radiographic films only measure a 2 dimensional (2D) distribution.

The search for a three dimensional (3D) dosimeter has led to the development of gel dosimeters. Gel dosimeters consist of a gel infused with materials which undergo a measurable change after irradiation (see Section 1.2).

There are numerous methods employed for measuring the post-irradiation change in the properties of gel dosimeters. One such method of analysis is x-ray computed tomography (CT) which measures the amount that radiation is attenuated within the object, i.e. the linear attenuation coefficient, μ. CT measures a 2D 'slice' through an object and is sensitive to small changes in its radiation attenuation properties. The measurement results are normally displayed in a 2D array with each element of the array corresponding to a discreet volume within the object. For ease of interpretation, each measurement is normally displayed on a pixel by pixel basis in greyscale intensity rather than numerically, and the entire measurement is therefore seen as an image of the radiation attenuation properties throughout the slice.

CT has been used to measure numerous objects ranging from the very small, such as cavities in rat bones, to the very large, such as sawmill logs. CT scanners are often purpose built to image objects of certain size ranges. The main area in which CT is used is undoubtedly in medicine and most scanners are commercially built and sold for this purpose. Medical CT scanners can distinguish changes in density within an

object and therefore soft tissue can be imaged in great detail. Furthermore, ‘slices’ (images) through a patient can be stacked to make a three-dimensional image.

A recent feasibility study [1] has shown that CT can be used to image polymer gel dosimeters. These dosimeters are systems designed to measure the 3D spatial dose distributions of radiation fields used in radiotherapy.

1.1 X-ray Computed Tomography (CT)

CT was first developed at the research laboratories of EMI Limited by Dr G. Hounsfield and results from the first scanner were presented at the 1972 Annual Congress of the British Institute of Radiology [2]. The following year a paper was published in the British Journal of Radiology detailing the system [3]. In 1979 Hounsfield jointly received the Nobel Prize for Medicine for his invention.

The advantage that CT has over the traditional x-ray radiograph is that it is a tomographic imaging technique (it produces an image as a single plane through an object) whereas a radiograph image shows all planes superimposed, which greatly reduces the contrast in the image (for example, a chest x-ray shows lungs, bone and soft tissue all superimposed). Because CT obtains separate images of each plane there is no superimposition of objects and low contrast regions are subsequently seen with greater ease.

1.1.1 CT Image Acquisition Process

CT works by reconstructing an image from x-ray projection data taken through an object at several hundred different angles. X-rays are produced by an x-ray tube, transmitted through the object as beams and are attenuated depending upon the amount and composition of the different materials through which the x-ray beam passes. X-rays are transmitted for each angle and detected by several hundred detectors, thus simulating several hundred beams. Each simulated beam is called a ray sum. For monoenergetic x-rays in a homogenous object the intensity, I of the beam transmitted through the object is:

$$I = I_0 \, e^{-\mu t} \qquad 1.1$$

where I_0 is the number of x-rays incident on the object and t is the thickness of the object. The more realistic situation of a polychromatic beam and heterogeneous object is discussed in Chapter 2. The intensity of each x-ray beam transmitted is measured by a detector. The intensity measurement results are then placed in a one dimensional vector called a projection, which represents the attenuation profile of the object for a particular angle as seen in Figure 1.1.

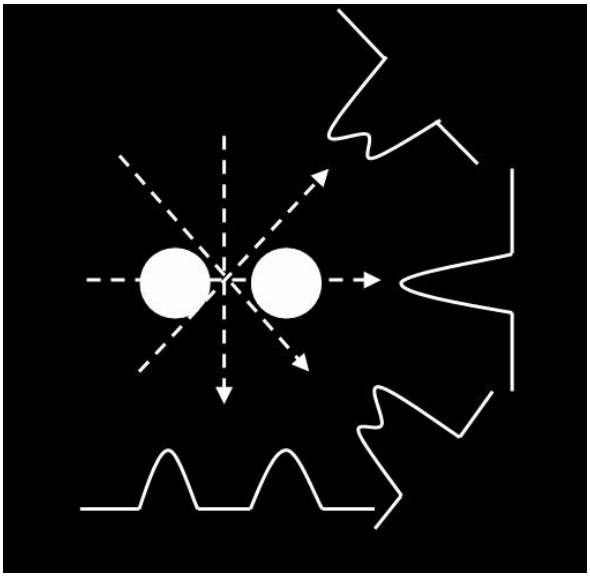

Figure 1.1 Attenuation profiles of an image of two circles taken at 4 angles. Each profile is called a projection.

When projections are acquired over several angles they are placed in matrix form to produce a sinogram (Figure 1.2). An inverse radon transform is performed on the sinogram and an image is obtained. The image is a map of the different radiation attenuation properties throughout the object. The inverse radon transform process is called ‘filtered back projection’. Back projection is the process of ‘smearing’ each projection data across the image plane by sharing the value of each ray sum among all of the pixels corresponding to the voxels through which the ray has passed. The process of back projection does not result in a perfect representation of the original object; each point in the image will be surrounded by a starburst pattern which degrades contrast and blurs edges. To improve the image the projections are convolved with a filter function prior to back projection and the entire process is termed ‘filtered back projection’. The final image will be a greyscale image and is a map of the radiation attenuation properties within the object.

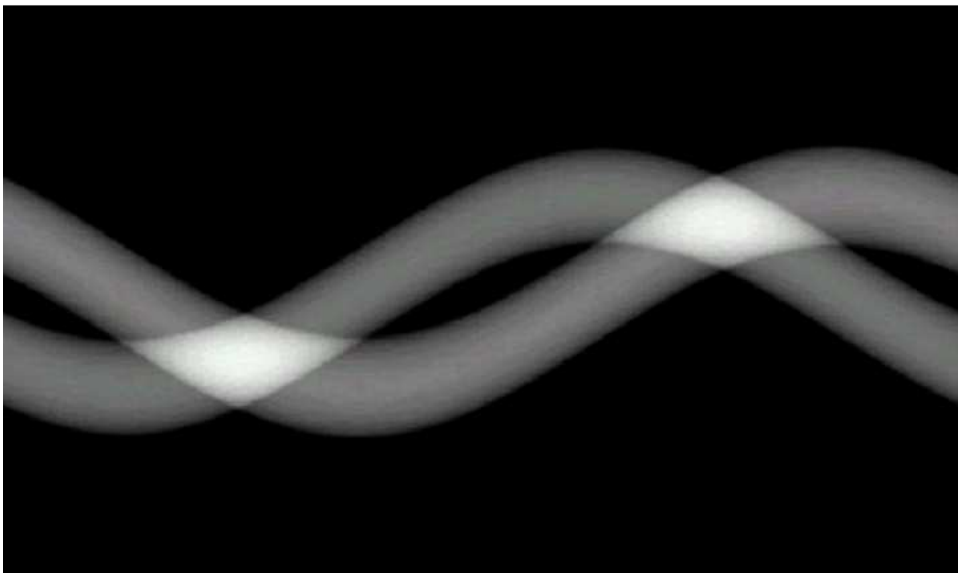

Figure 1.2 Sinogram of the two circles seen in Figure 1.1.

More detailed description of various aspects of CT image acquisition will be given in Chapters 2 and 5. For a general description of CT see Michael, 2001 [4] and for detailed technical descriptions of the processes of CT image acquisition see Newton, 1981 [5].

1.2 Gel Dosimetry

Gel dosimeters consist of a gel infused with radiation sensitive materials. After irradiation a measurable change is induced in the active materials which are held in position by the gel matrix, thus preserving a spatial record of the irradiation. The gel usually consists of water mixed with a gelling agent such as gelatin, agarose or polyvinyl alcohol (PVA). The radiation sensitive materials to date have mainly been Fricke solutions or monomers; however many formulations have been investigated and no doubt several more will show radiation sensitivity in future research.

Gel dosimeters have several advantages over current techniques. Not only are they a 3D dosimeter, but the dosimeter itself is also the phantom and hence does not perturb the dose distribution ‘behind’ the point of measurement. Because gels are manufactured as a liquid and then allowed to set they can be poured into containers of varying shape and can thus easily become anthropomorphic phantoms. Finally, gel

dosimeters show some degree of radiological tissue equivalence resulting in more accurate modelling of a radiation dose distribution.

1.2.1 Brief History

In 1950 Day and Stein infused gelatin and agar gels with decolorized methylene blue and phenol-indo dyes and observed colorization after irradiation [6]. It was later observed that irradiation induces polymerisation in crystalline acrylamide [7]. In 1957 Andrews *et al* used a chloral hydrate-agar gel for depth dose measurements with x-rays and electrons [8]. When irradiated the chloral hydrate forms HCl thus changing pH and electrical conductivity, which can be visualised by adding an acid-base indicator, or measured with a pH electrode or conductivity electrode pair. It was reported that, due to diffusion effects, measurements needed to be taken soon after irradiation. The invasive measurement techniques available at the time (probes) and the requirement to remove large samples from the gel were detrimental to spatial resolution [8].

In 1984 Gore *et al* used magnetic resonance imaging (MRI) to measure the post-irradiation oxidative conversion of ferrous ions, Fe^{2+} to ferric ions, Fe^{3+} [9] and proposed that the solution be infused into a gel to record spatial distribution of radiation doses. This paper initiated research into gel dosimetry by many groups throughout the world and gel dosimetry became a burgeoning field of medical physics.

A limitation in Fricke gel dosimeters is that the ferric ions diffuse throughout the gel leading to a degradation in spatial dose information within hours of irradiation [10]. In 1993 and 1994 Maryanski *et al* published two papers reporting investigation of a gel infused with radiation sensitive polymers which give rise to an MRI signal after irradiation, and which does not suffer the diffusion problems of Fricke gel dosimeters [11, 12]. A patent was obtained by Maryanski *et al* for the formulation of polymer gel dosimeters [13] resulting in a commercial gel dosimeter becoming available. In 1996 it was reported that the optical properties of gel dosimeters change after irradiation [14, 15] and an optical scanner was developed using a similar geometry to first generation x-ray computed tomography (CT) scanners [16]. Optical scanners are now commercially available and several groups have built their own

scanners. Fourier Transform Raman Spectroscopy was used in 1998 to examine post-irradiation changes in polymer gel dosimeters [17]. In 2000 a feasibility study into the suitability of CT of polymer gel dosimeters was published and it was found that CT can be effectively used as a method for extraction of absorbed dose information [1]. In 2002 a study revealed that absorbed dose information can be obtained from a gel dosimeter through the use of ultrasound [18].

One of the limitations of polymer gel dosimetry is that molecular oxygen will inhibit the processes leading to polymerization, requiring special manufacturing and handling procedures (see next section). In 2001 Fong *et al* investigated and reported a new polymer gel formulation which could be manufactured in normal atmospheric conditions, thus greatly simplifying the production to the point that polymer gel dosimeters can now be made on the bench top without the requirement to purchase specialized equipment, although it should be noted that these gel dosimeters still require an oxygen barrier once produced [19]. It is anticipated that this development is a major step towards the widespread clinical use of gel dosimeters.

Since 1984 there has been a proliferation of research into gel dosimetry from groups throughout the world. In 1999 the First International Workshop on Radiation Therapy Gel Dosimetry [20] took place in Lexington, USA and in 2001 the 2nd International Conference on Radiation Gel Dosimetry took place in Brisbane, Australia. A third conference is planned for 2004 at the International Atomic Energy Agency in Vienna, Austria.

1.2.2 Polymer Gel Dosimeters

Polymer gel dosimeters consist of monomers mixed into a gel solution. The most widely used monomer to date has been Acrylamide (AA) mixed with the cross linker N,N'-methylene-bis-acrylamide (BIS) [11] although other chemicals have been used such as 2-Hydroxyethylacrylate (HEA) [21] and 1-vinyl-2-pyrrolidinone [22]. Upon irradiation free radicals released during the radiolysis of the water within the gel initiate polymerisation and cross-linking of the monomers. The amount of free radicals released is proportional to the dose received by the gel dosimeter and the resultant amount of polymer formed is therefore also proportional to dose until an upper limit is reached. After the upper dose limit is reached consumption of

monomers results in a saturation effect and the amount of polymerisation asymptotes to some upper level [17].

Oxygen is an efficient scavenger of free radicals [23] and must be purged from polymer gel dosimeters prior to irradiation or the polymerisation process will be inhibited [11, 12, 24-26]. This results in the requirement for specialized equipment, manufacturing procedures and post-manufacture handling and has been a disadvantage of using polymer gel dosimeters. Production of polymer gel dosimeters is achieved either by sealing the chemicals in mixing flasks and flushing the gel and flask with nitrogen followed by pumping the gel from the preparation flask into the phantom [12, 24], or by enclosing the chemicals and phantom in a glovebox flushed with nitrogen or argon and completely preparing the polymer gel dosimeter within. Mixing procedures for gelatin gels normally involve soaking the gelatin in water and heating to approximately 50°C under continual stirring followed by adding the monomers and stirring until they are dissolved [24]. For agarose gels the same procedures are followed however the water and agarose mixture is heated to above 90°C to allow the agarose to mix with the water and the solution is then cooled to 50°C before adding the monomers. After the gel dosimeter is mixed it is poured into a phantom before gelation occurs.

After a polymer gel dosimeter is manufactured it must remain oxygen free until it is irradiated and polymerisation has occurred. Phantom wall materials must therefore have a low permeability to oxygen. Plastic and Perspex phantoms show signs that oxygen can penetrate into the gel and degrade the dose information [12, 27] whereas glass and Barex (BP Chemicals) have shown to have low oxygen permeability for the purposes of polymer gel dosimetry [27, 28].

Dose information can be extracted from polymer gel dosimeters by several methods. Post-irradiation changes in the relaxation rates of water protons allow MRI measurements to be made. MRI was the method used by Maryanski in 1994 [29] and has resulted in the most research activity to date. Scattering of light by polymer gel dosimeters is related to the amount of polymerisation which in turn is related to the absorbed dose [14]. This light attenuation property has been investigated and used to produce optical tomography systems based on first and second generation CT configurations [16, 30]. Raman spectroscopy has been employed to investigate the

inelastic scattering of light from the different vibrational modes of the monomers and polymers in irradiated polymer gel dosimeters [17, 31-34]. Post-irradiation changes in the linear attenuation coefficient, μ in polymer gel dosimeters has enabled extraction of information by x-ray computed tomography (CT) [1, 35, 36]. Changes in acoustic properties have shown that ultrasound is a promising imaging modality for polymer gel dosimeters [18]

A disadvantage of polymer gel dosimeters is the difficulty in ensuring that the system remains free of oxygen. A new formulation of acrylic dosimeter was reported by Fong *et al* in 2001 which contains oxygen scavengers and can be manufactured in normal atmospheric conditions [19]. This formulation consists of methacrylic acid, copper (II) ions, ascorbic acid, hydroquinone, gelatin and water and is given the acronym MAGIC [19]. Other formulations of normoxic gel dosimeters are currently under investigation. To date, measurements have been made using MRI [19, 37] and ultrasound [38].

1.3 Aims

CT has many advantages over existing methods of extracting dose information from gel dosimeters. One such advantage is that many radiotherapy clinics already possess CT scanners for treatment planning purposes and hence there is no requirement to purchase specialised equipment. Although MRI is also available to many clinics, image plane inhomogeneities and lengthy imaging times are included in the current limitations, as well as the requirement that gel dosimeters must be brought to a stable temperature prior to MRI imaging [39, 40]. The combination of the recently developed normoxic gel dosimeters and the availability and simplicity of CT may lead to the widespread clinical use of gel dosimeters for accurate dose distributions of radiation therapy treatments.

Prior to this project there has been very limited research published regarding CT imaging of gel dosimeters. In fact, there had been only one journal paper which was a feasibility study of the technique [1]. Since then, besides the work published as a result of this project, there has been only one additional journal paper on the subject [36].

There is a need to develop suitable CT imaging techniques for gel dosimetry to ensure that the radiation dose information can be accurately and precisely measured and reported. Therefore, the aim of this project is to develop and advance CT imaging techniques for gel dosimetry.

Chapter 2: Artifact Reduction

2.1 Introduction

CT as an imaging modality is susceptible to numerous artifacts. In clinical CT of humans many of the artifacts will not adversely affect the image to the extent that they interfere with a radiologist's diagnosis. It is seen in following chapters that a different approach to CT is available when imaging gel dosimeters rather than patients, in that stochastic noise can be greatly reduced by drastically increasing the x-ray exposure time without the necessity of keeping radiation dose to a minimum. Furthermore, it will be shown that in CT gel dosimetry artifacts which would normally be hidden by the background stochastic noise in clinical CT become more pronounced. These artifacts must be either removed or corrected to improve the accuracy of dose measurements within a gel dosimeter and to improve the signal to noise ratio.

This chapter examines some of the artifacts that adversely affect the accuracy of quantitative CT measurements and a phantom is designed and used in the implementation of a method for the reduction of these artifacts. The phantom designed in this chapter provides an imaging method suitable for investigation of the response of gel dosimeters when imaged within calibration vials (Chapter 3). More advanced techniques are be developed in Chapter 5 which are suitable for imaging dose distributions within gel dosimetry phantoms.

2.2 Background

Artifacts in CT can be broadly classified as spectral effects, geometric artifacts, reconstruction errors, or hardware related errors. The following section briefly describes the artifacts relevant to CT gel dosimetry.

2.2.1 Spectral Effects

As stated in Chapter 1 x-rays are produced and projected through an object. Some of the x-rays will be attenuated and some will be transmitted through the object. For a monoenergetic beam in a homogenous object the number of x-rays transmitted is given by Equation 1.1. When the object is heterogeneous, i.e. consisting of materials of different μ, Equation 1.1 becomes:

$$I = I_0 \, e^{-\int_0^t \mu(x)dx} \qquad 2.1$$

The x-ray source in a CT scanner is a rotating anode, tungsten target and an x-ray tube and hence the beam is polyenergetic. The linear attenuation coefficient is energy dependent, and as the beam passes through the object the lower energy x-rays within the beam will be attenuated at a faster rate than those of higher energy. The mean energy of the beam will therefore increase as it passes through the material [41] and the process is termed 'beam hardening'. Due to the increase in mean beam energy and the fact that μ is energy dependent, the effective μ of the material, μ_{eff} will decrease as the beam traverses the material. The effective linear attenuation coefficient at distance *y* in a homogenous material can be derived as [41]:

$$\mu_{eff} = \frac{\int I_0(E)\mu(E)e^{-\mu(E)y}dE}{\int I_0(E)e^{-\mu(E)y}dE} \qquad 2.2$$

where there are $I_o(E)\,dE$ photons entering the object in the energy range E to $E + dE$. For the polyenergetic beam Equation 2.1 becomes:

$$I = I_0 \, e^{-\int_0^t \mu_{eff}(x)dx} \qquad 2.3$$

After the beam exits the object it falls upon a detector which measures the exit beam intensity, i.e. *I*. The incident beam intensity, I_0, is also measured with a reference detector. The logarithm of the intensity ratio:

$$\ln\left(\frac{I_0}{I}\right) = \int_0^t \mu_{eff}(x)dx \qquad 2.4$$

is called the ray-sum, i.e. it is the sum of attenuation coefficients along the ray path. A number of ray-sums are acquired to form an attenuation profile through the object at a particular orientation. Each attenuation profile is called a projection.

Once a number of projections have been acquired an inverse radon transform is performed on the data to produce an image. This process is termed image reconstruction. The image is a map of μ_{eff} throughout the object. The value of each pixel is scaled to the linear attenuation coefficient of water, μ_{water} and given the term CT Number, H and expressed in Hounsfield units:

$$H = 1000\frac{\mu_{eff} - \mu_{water}}{\mu_{water}} \qquad 2.5$$

The changing value of μ_{eff} throughout the object results in a decrease in H radially inwards from the edges of the image of the object. This in turn results in incorrect values for H causing inaccuracies in quantitative applications of CT such as gel dosimetry. Figure 2.1 is a CT image of a 25 cm diameter phantom filled with water. Beam hardening can be seen as the lighter pixels around the inside edge of the phantom and as a decrease in CT values at the object edge in the accompanying profile. This form of beam hardening artifact is referred to as the ‘cupping’ artifact.

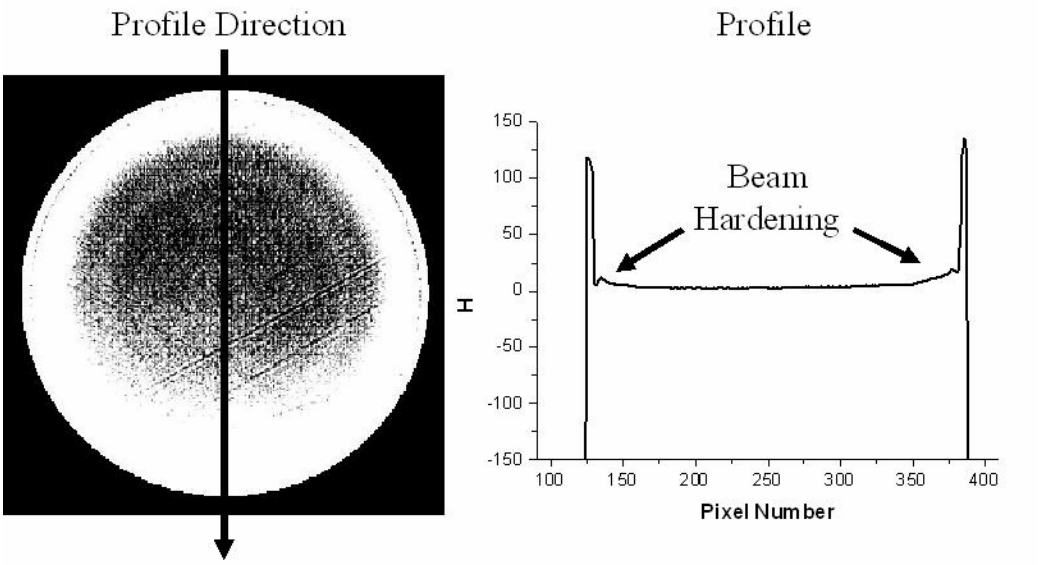

Figure 2.1 CT image of a 25 cm diameter water filled phantom. The beam hardening cupping artifact can be seen as a darkening of the image radially inwards from the edge of the phantom. The profile shows this as a decrease in pixel values away from the phantom edge

A further consequence of beam hardening in CT is the nonlinearity of detected photon counts. In the ideal case of a narrow monoenergetic beam transmitted through a homogenous medium and counted with a reliable detector, the value of logarithm of I is proportional to ρt [42], where ρ is the density of the medium. However, as beam hardening occurs along the path length of the beam, the change in μ_{eff} causes the beam to become more penetrating, which results in a relative increase in $log\ I$ with respect to ρt. This results in an error adding an additional term to the exponential term in Equation 2.1 [42]:

$$I = I_0\, e^{-\mu_m \rho t + A \rho^2 t^2} \qquad 2.6$$

where A is a constant and directly related to the homogeneity of the spectrum [43] and μ_m is the mass attenuation coefficient, i.e. $\mu_m = \mu/\rho$.

The effect is further enhanced through scatter and detector nonlinearity. Figure 2.2 is copied directly from [42] and demonstrates how the nonlinearity of detected photon counts results in streak artifacts occurring between objects. The illustration is that of two rods with projections at 0° and 90°. The error is proportional to $\rho^2 t^2$ and hence is four times larger in view 0 where the rods are superimposed than in view 90

where they are separate [42]. This inconsistency in the error results in streaks occurring between the two rods when the image is reconstructed [44].

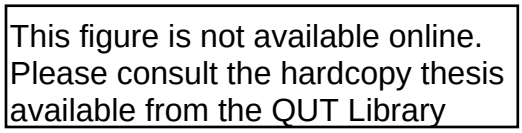

Figure 2.2 The error in view 0 is four times that of view 90 resulting in a streak between the two rods (Joseph (1981)).

2.2.2 Geometric Artifacts

CT images are reconstructed as inverse radon transforms of projection data. If the projection data consists of an infinite number of projections, each consisting of an infinite number of ray-sums with negligible beam widths the image could be reconstructed without geometric error [42]. However, in the practical situation of a clinical scanner there is a limit to the number of ray-sums and projections which can be acquired, plus the x-ray beam and detector are of a finite width. Therefore, CT data acquisition becomes an issue of sampling.

The most significant sampling problem in CT is that of aliasing. Aliasing occurs in signal processing when there are too few measurements taken of a signal. The Nyquist theorem states that an alternating signal must be measured at least twice per cycle to avoid aliasing [45]. If it is measured at a rate less than this, information regarding the waveform between measurements will be lost. The measurement will

result in the true frequency being recorded as a lesser frequency, thus causing an aliasing error.

Fourier analysis of images shows that sharp edges such as water/air interfaces have stronger high frequency components than soft edges [42]. In CT any frequency greater than half the maximum sampling frequency of each scanner will be aliased as a lower frequency. This results in not only a limit to available spatial resolution on a scanner, but will also cause the appearance of fine streaks from sharp edges in a CT image and contributes to a finely structured moiré pattern in the background [42].

2.2.3 Hardware Related Errors

When a CT image is reconstructed from projection data, the reconstruction algorithm generally does not allow for the occurrence of fluctuations in individual detector efficiency throughout the time of the scan. These variations represent an error in the measurements and may be propagated through the reconstructed image in some generations of CT scanners..

Figure 2.3 is an example of how a faulty detector affects a CT image. The graph on the left is a simulation of noiseless projection data where two banks of six adjacent detectors each have a 5% deficiency in their counts. Uniform projection data should produce an approximately uniformly reconstructed image (apart from Moire patterns). The reconstructed image (Figure 2.3b) shows two ring artifacts which result from the defective detectors. In quantitative CT this can result in errors which are shown later in this chapter.

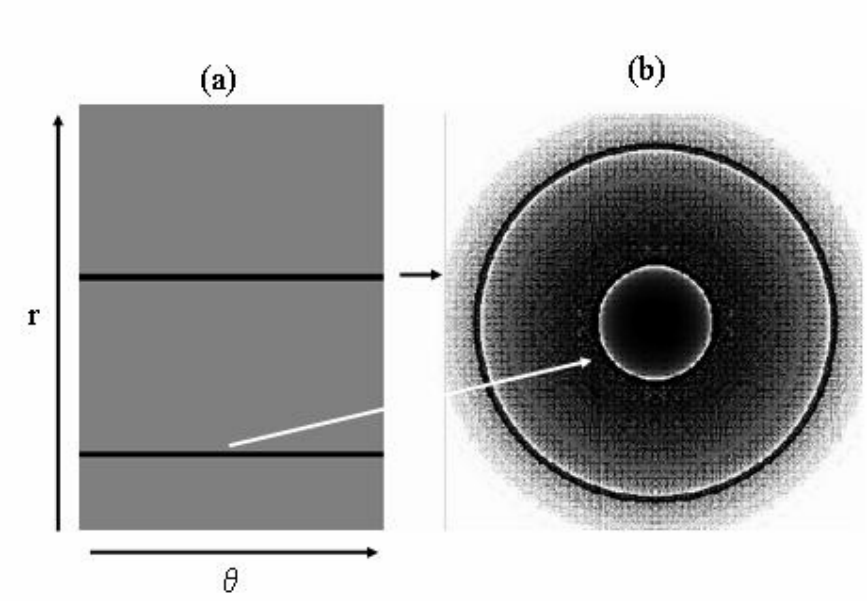

Figure 2.3 The effect of faulty detectors on a reconstructed image. The image on the left is the projection data with two banks of faulty detectors which translate to the rings seen in the reconstructed figure on the right.

2.3 Imaging Techniques

2.3.1 Subtraction of Artifacts

The artifacts outlined above contribute to erroneous results in quantitative CT and must be removed or reduced. One method of reducing artifacts is image subtraction. Subtraction of artifacts has been previously employed in gel dosimetry [1]. This previous method required the production of a second gel dosimeter in an identical phantom which was imaged in the same position as the original phantom. This method requires extremely accurate realignment of the second phantom and thus imaging of calibration vials can be difficult. Also required is the production of two phantoms and twice the volume of gel dosimeter, doubling the monetary expense. In this work a tank was designed as an alternative imaging method to simplify the process and eliminate the requirement for a second gel dosimeter and phantom.

The tank consists of a 25 cm diameter cylindrical water tank with a square access tank seen in Figure 2.4. The entire gel dosimetry phantom is placed inside the water tank and an image is acquired near the front face of the cylinder (as indicated in Figure 2.4). The gel phantom is then withdrawn a few centimetres along the tank and

an image is acquired of only water in the same location relative to the tank and table. The water only image is then subtracted from the gel phantom image. Figure 2.5a shows an image of calibration vials filled with polymer gel dosimeter complete with beam hardening and ring artifacts. The image is windowed to a level suitable for viewing the artifacts. The pixel values within the gel vials are greater than the upper limit of the window; hence they appear in this image as white. Figure 2.5b shows the image of the tank filled with water only, also with beam hardening and ring artifacts, and the image on the right shows the resulting final difference image after subtraction of the water image from the image of the gel vials. It can be seen in the final image (Figure 2.5c) that the beam hardening cupping artifact and ring artifacts have been removed. The nonlinear streak artifacts seen between calibration vials in the original image remain in the final image due to the fact that they are not present in the subtracted water image. The streak artifacts do not extend to the region within the vials and can therefore be disregarded in this instance.

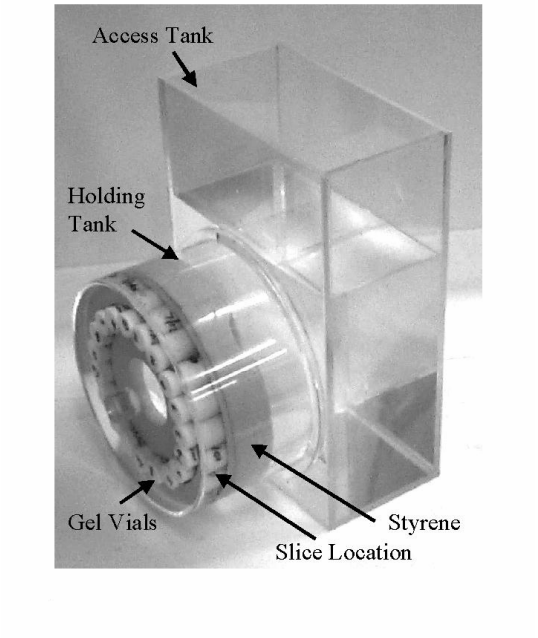

Figure 2.4 Water tank for CT imaging of gel dosimeters. The tank consists of a cylindrical water tank and a rectangular access tank. The phantom (calibration vials in this case) is placed in the cylindrical tank.

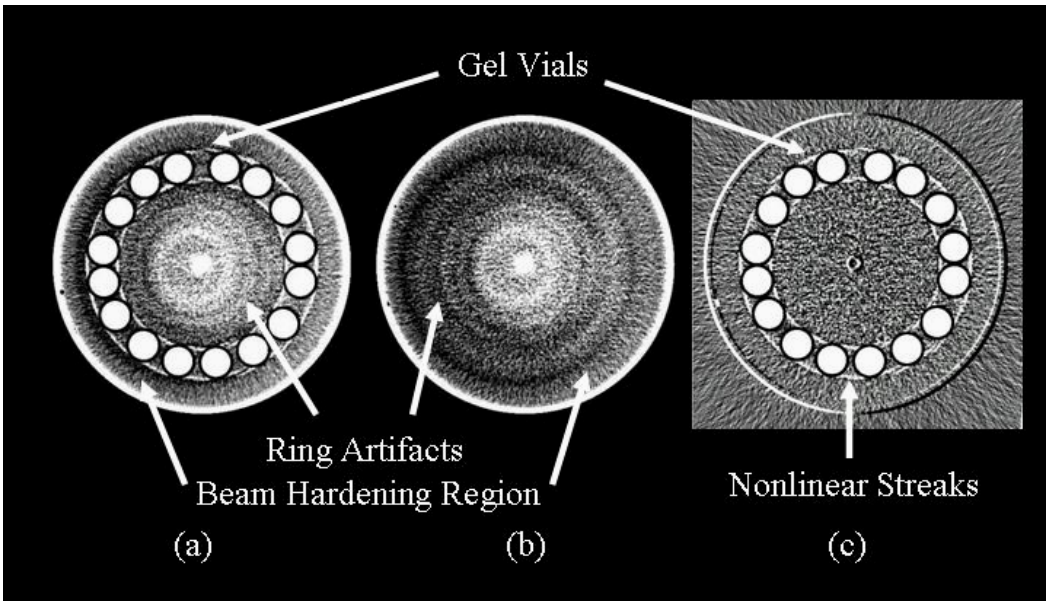

Figure 2.5 Subtraction of artifacts from a CT image. The image on the left is that of the calibration vials, the centre image is of water, and the image on the right is the difference image.

The requirement for the tank to be filled with water is due to beam hardening and geometric artifacts. The main effects of beam hardening are normally present within 2 cm of air/water or air/Perspex boundaries [46]. Figure 2.6a shows the image of a 2.5 cm diameter calibration vial filled with a homogenous gel which was acquired with the vial in air, and it can be clearly seen in the profile that there is a relatively large variation in CT number within the vial which introduces a significant uncertainty into any measured CT number of the gel. Figure 2.6b shows the same calibration vial imaged in water and the variation in CT number is not seen. To further reduce the risk of interference in measurements due to beam hardening a gel dosimetry phantom (or calibration vials) should be placed no closer than 2 cm from the Perspex tank wall.

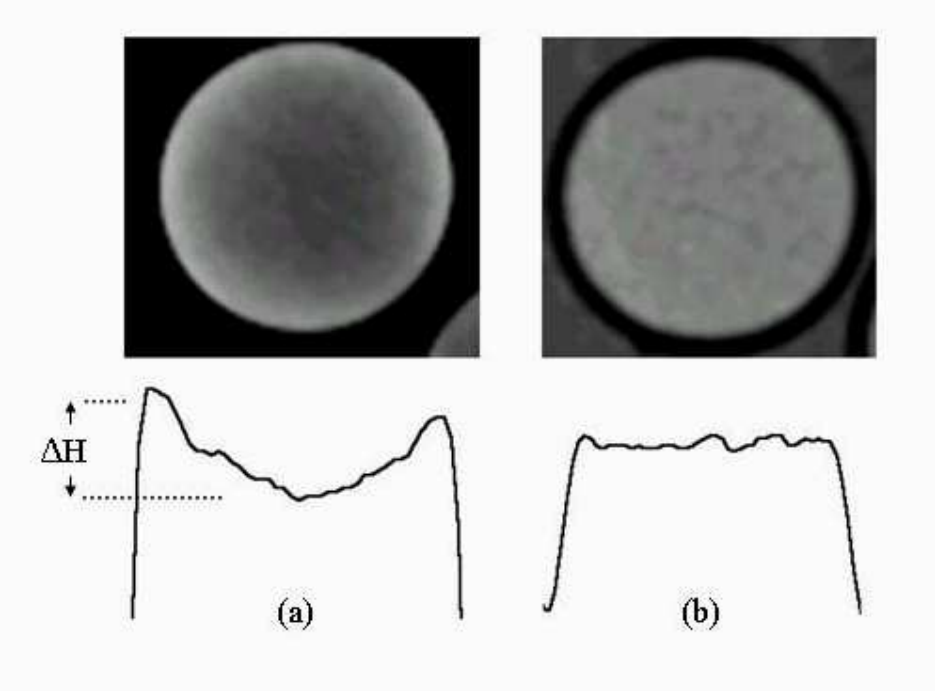

Figure 2.6 Comparison of a calibration vial imaged in air (left) and in water (right). The profiles below the images show that the beam hardening apparent in the first image is greatly reduced in the second.

For optimal performance of the subtraction technique the tank should not be moved relative to the CT scanner gantry at any stage during imaging. The effectiveness of the method relies on the beam hardening and ring artifacts being superimposed in the original and water images. The purpose of the access tank is so that the gel phantom can be removed without moving the tank.

Figure 2.7 shows example calibration graphs obtained using the tank. In the image of the vials (Figure 2.7a) it is evident that in addition to beam hardening and ring artifacts there is a gradient in CT number from left to right (the background pixels become darker), indicating a possible fault with the scanner or poor detector calibration. The uncorrected graph (Figure 2.7b) shows the result obtained from the original image, and Figure 2.7c shows the result obtained after the subtraction. The figures clearly show the necessity for the subtraction. The uncorrected calibration graph shows that the gradient has resulted in a large inaccuracy. The corrected calibration graph shows that the expected exponential behaviour (see Chapter 3) has been restored.

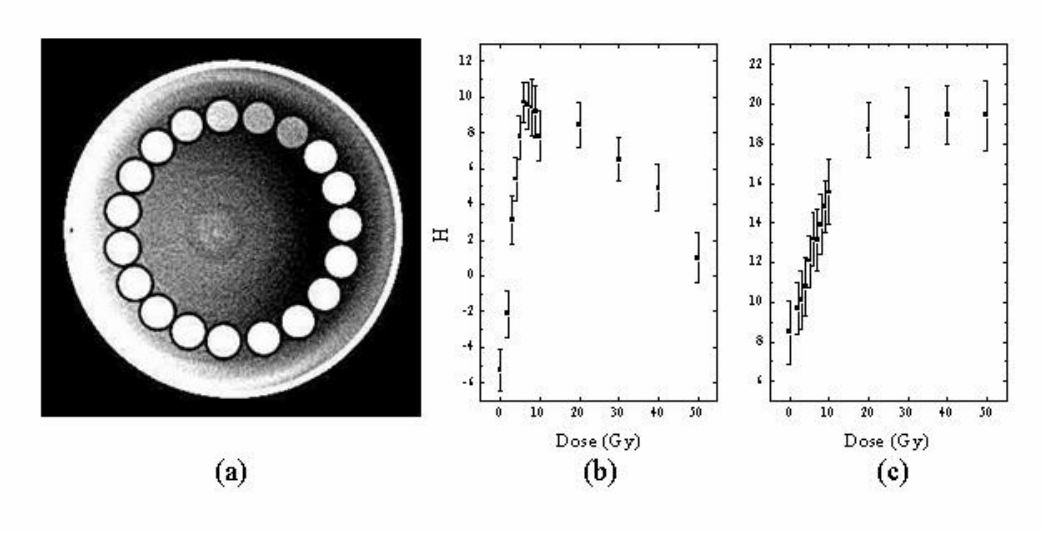

Figure 2.7 Calibration graphs taken from the image on the left. The first graph (b) is uncorrected and the second graph (c) has been corrected through subtraction of a water image.

2.3.2 Phantom Wall Materials

Beam hardening causes the greatest error near the air/phantom boundary and in the previous section a technique was devised to minimize the cupping effect. The subtraction technique works well when the material inside the water tank is close to homogenous. However when there are inhomogeneities in the original image which have a significantly different μ to water, the energy dependence of equation 2.2 ensures that beam hardening streak effects will occur within the inhomogeneity. As seen in Chapter 3 gel dosimeters have values of μ which are relatively close to that of water even when irradiated, so there should be relatively little error caused by beam hardening due to the gel itself. However, phantom wall materials may contribute errors. For example Figure 2.8 shows the effect of using a glass walled gel container. The image is of a homogenous polymer gel dosimeter inside a glass flask, which has been imaged inside the water tank described previously. Beam hardening can be seen in the close-up of the vial (Figure 2.8b) as a darkening of pixels towards the centre of the vial. The profile on the right quantitatively shows the effect with a decrease in pixel values in the centre of the vial.

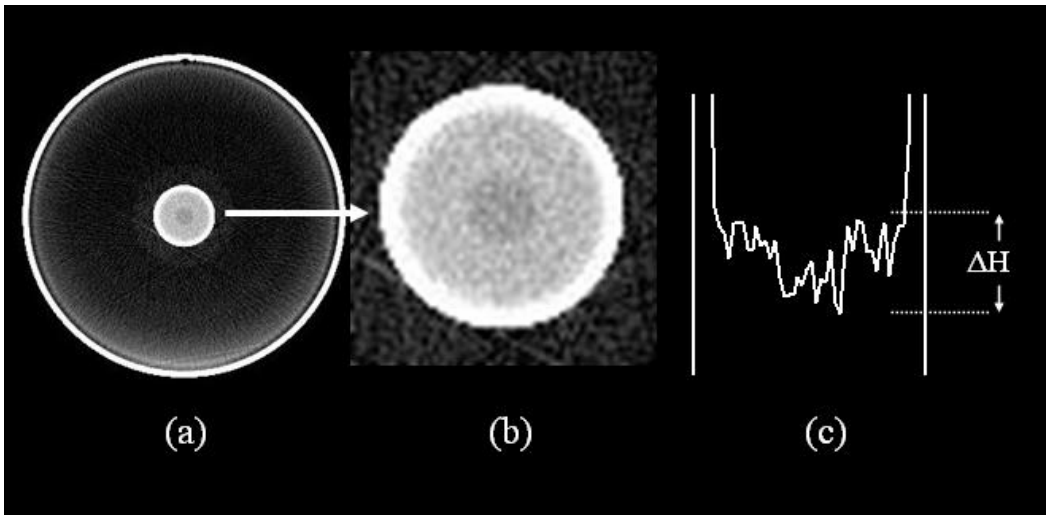

Figure 2.8 Image of a glass flask containing gel. The image on the left is the flask in the water tank, the image in the centre is a close-up of the flask, and the image on the right is a profile through the flask.

In summary, to minimize beam hardening within a gel dosimetry phantom, wall materials should be manufactured from materials with μ values close to that of water.

2.4 Chapter Summary

CT is susceptible to many artifacts. Some of these artifacts are relevant to CT imaging of gel dosimeters and can introduce errors into a measurement. A specialised water tank has been designed and constructed to correct most errors due to the artifacts. Artifacts which do not occur in the background subtraction (water) image such as non-linear streaks and beam hardening due to certain phantom wall materials will not be subtracted, however these artifacts can be reduced by using wall materials which have μ values close to that of water.

The work in this chapter has been published in the journal 'Physics in Medicine and Biology' [35]

Chapter 3: CT Dose Response

3.1 Introduction

In chapter 2 methods were established whereby quantitative measurements of gel dosimeters can be made using CT. Basic measurements can now be made using calibration vials to characterise the post-irradiation changes in CT signal.

In this chapter polymer gels of various compositions are manufactured and irradiated to various doses. Measurements of the gels are made in a clinical CT scanner and the signal is examined.

3.2 Background

It has been shown in the literature that post-irradiation changes in polymer gel dosimeters give rise to a CT signal which is approximately linear up to a dose of 15 Gy and that an image of the dose distribution can be produced [1]. Investigations into the MRI signal of post-irradiation changes have assumed a quasi-linear response up to approximately the same dose, however when greater doses are delivered strong deviations from linearity are observed [47-51]. There has been no previous study into the CT signal after high doses have been delivered, nor has there been any previous investigation into the effect of variations in chemical composition. This chapter examines the effects of high doses and varying chemical concentrations on the CT signal of polymer gel dosimeters.

The following terms are defined according to accepted nomenclature [52]. The CT dose-response *(r)* of a polymer gel is defined as the reading of the dosimeter *(H)* after a particular dose has been delivered. The CT dose-sensitivity is defined as *dr/dD.*

3.3 Methods and Materials

3.3.1 Polymer Gel manufacture

Polymer gel dosimeters were manufactured with varying concentrations of acrylamide (AA) (Sigma Aldrich, Sydney), N,N'-methylene-bis-acrylamide (BIS) (Sigma Aldrich, Sydney) and hydroxyethylacrylate (HEA) (Sigma Aldrich, Sydney) comonomers dissolved in a matrix of aqueous gelatin (300 bloom) (Sigma Aldrich, Sydney) or agarose (FMC Bioproducts, Rutherford) as shown in Table 3-1. The gels were produced in a nitrogen filled glovebox using methods previously described [24]. After production, all gels except HEA1 were poured into 20 ml polyethylene liquid scintillator vials (diameter 27 mm, wall thickness 1 mm, length 60 mm)(Packard, Meriden). Plastic vials were used instead of glass vials to minimize x-ray beam hardening artifacts during imaging. MAGAS1 was produced on the benchtop by another researcher as an example of a normoxic gel and contained the concentrations of chemicals listed in Table 3-1. HEA1 was a gel previously produced by another researcher using the above methods and is included only to illustrate that a CT signal can be obtained with gels of that composition. It was several weeks old at the time of use and was melted and poured into the vials prior to imaging. The procedures stated in the following paragraph do not apply to HEA1.

As discussed in Chapter 1 the scavenging of free radicals by oxygen [23] potentially inhibits radiation-induced polymerisation in polymer gel dosimeters contained within plastic walled phantoms [12, 27]. To minimise this effect the vials were heat sealed in pouches made from 0.1 mm thick Barex sheets (Arbo Plastic Ltd, Switzerland) prior to removal from the nitrogen atmosphere of the glovebox used for manufacture. Barex has low permeability to oxygen [53] and was previously used for manufacture of polymer gel dosimetry phantoms [54]. The use of this material ensured that the vials were kept in an oxygen free atmosphere.

The pouches containing the vials of polymer gel were then cooled in water at approximately 10°C for approximately 1-2 hours until a visual inspection revealed that they had set. They were subsequently kept at room temperature and irradiated in their Barex pouches after a further 1 hour.

Table 3-1 Composition and measurement results of the various gel dosimeters examined.

Polymer Gel Dosimeter	Monomers by % weight			Gelling Agent by % weight		Water by % weight	CT Dose Sensitivity (Linear Region) ($H\ Gy^{-1}$)
	BIS	AA	HEA	Gelatin	Agarose		
PAG1	3	3		2		92	0.78 ± 0.03
PAG2	3	3		3.5		90.5	0.87 ± 0.03
PAG3	3	3		5		89	0.71 ± 0.02
PAG4	3	3		6.5		87.5	0.59 ± 0.02
PAG5	3	3		8		86	0.54 ± 0.01
PAG6	1	1		5		93	0.26 ± 0.02
PAG7	2	2		5		91	0.40 ± 0.04
PAG8	5	5		5		85	1.14 ± 0.04
PAG9	6	6		5		83	1.43 ± 0.05
PAA1	3	3			1	93	1.2 ± 0.1
PAA2	4	4			1	91	1.3 ± 0.1
HEA1	4		2	5		89	1.0 ± 0.2
MAGAS1	0.01 mM $CuSO_4$ 9 % Methacrylic Acid 0.09 % Ascorbic Acid			8		82	0.34 ± 0.02

3.3.2 Irradiation

The polymer gel dosimeters were irradiated in their Barex pouches at a dose rate of 12 Gy per minute up to 50 Gy in a ^{60}Co Gammacell 200 (Atomic Energy of Canada Ltd) which had previously been calibrated [55]. It has been shown previously that the dose response of polymer gel dosimeters is energy independent in the energy range of clinical irradiations [56]. The gels were removed from the pouches and exposed to oxygen after three days as the majority of the polymerisation reactions have occurred by that time [26, 49, 57, 58]. Exposure to oxygen stabilised the polymer gel dosimeter ensuring all samples experienced the same conditions post-polymerisation. Exposure was achieved by removal of the lid of the vials for approximately 5 minutes at both three and four days after irradiation. Longer exposure times were avoided to prevent dehydration of the polymer gel dosimeters. The vials were then left for at least two days prior to imaging to allow diffusion of oxygen throughout the entire gel.

3.3.3 Imaging

Imaging was performed using a Picker PQ5000 CT scanner. The gel vials were placed in the water tank as seen in Figure 2.4. The highest kV (140 kV) and tube current (400 mA) available were used with an exposure time of 1.5 seconds. This allowed a large number of photons to reach the CT detectors thereby reducing stochastic noise [59]. To further reduce stochastic noise, twenty 5-mm slices (of the same slice) were acquired and averaged for each polymer gel dosimeter composition, effectively increasing the mAs by twenty times. Imaging time using this method was approximately 10 minutes.

The images were transferred to a personal computer and processed using the image processing toolbox in MATLAB™ software (The Mathworks, Inc). Circular regions of interest (ROI) of 230 pixels were drawn in the area of the image corresponding to the polymer gel dosimeter inside the vials.

3.4 Results

Figures 3.1-3.5 show the CT-dose response of the gels. Uncertainty in each data point of the figures is small due to the sampling of a large number of pixels and error bars have subsequently been omitted. Also shown are mono-exponential functions fitted to the experimental data for visualization purposes. It is visually apparent that a mono-exponential function fits all curves well. The function is of the form:

$$H = y + A\exp\left(\frac{-D}{t}\right) \qquad 3.1$$

where *y*, *A*, and *t* are the fit parameters of the function. In the lower dose regions of the figures a steady increase in signal is seen as monomers are consumed. The asymptotic behaviour seen at higher doses is a saturation effect arising due to fewer remaining monomers available for consumption [49].

Previous literature has shown that a bi-exponential calibration can also be fitted to the data when measuring the dose response with MRI [49] incorporating a positive exponential term into Equation 3.1. The extra exponential term arises due to the presence of small amounts of oxygen competing with the polymerisation process. In the case of the polymer gel dosimeters produced for this chapter chi-square and P values are lower for mono-exponential than bi-exponential fits.

In scanning polymer gel dosimeters using MRI it is common practice to obtain a calibration graph from a linear fit to the quasi-linear increase of R_2 at low doses. A divergence from linearity has been repeatedly observed [47-51], however an assumption of linearity is often still used for a limited dose range. To investigate whether a linear fit could be assumed for CT of polymer gel dosimeters, a chi-square test was performed on the exponential and linear fits in the 0-10 Gy region for gelatin gels and 0-8 Gy region for agarose gels. The linear fit was shown to have the lowest chi-square value. These regions were therefore approximated as linear and are referred to as the 'linear region' for the remainder of this chapter. The linear region is shown in the inserts in Figures 3.1-3.5 with linear functions fitted to the data.

In the case of a clinical phantom irradiation most irradiations would not exceed the doses of the linear region or calibration will become overly complex. Figure 3.6 shows the data for PAG3 in the linear region with the various functions fitted to the data. The lowest chi-square value was obtained for the linear fit indicating that although mono-exponential and bi-exponential functions approximately fit the data over a large dose range the true model of the dose response is yet another function, which indicates that there may be another variable(s) besides remaining monomer and oxygen concentration.

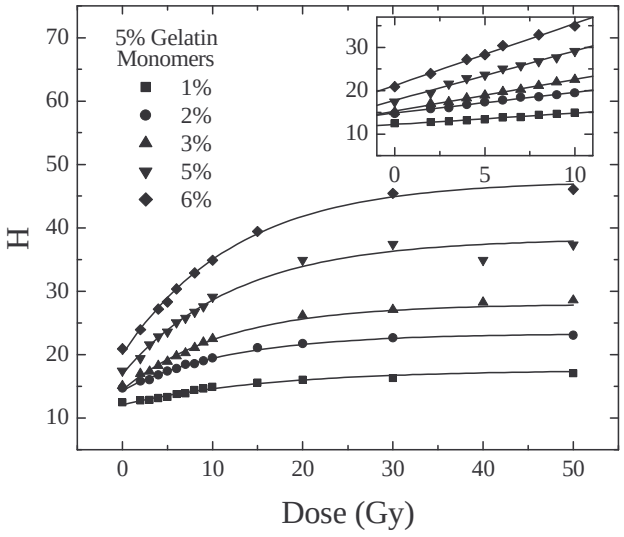

Figure 3.1 Dose response of PAGs with varying monomer concentrations.

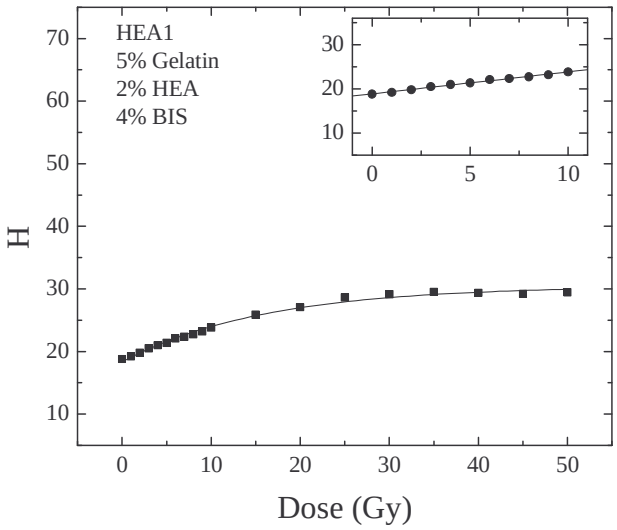

Figure 3.2 Dose response of HEA1.

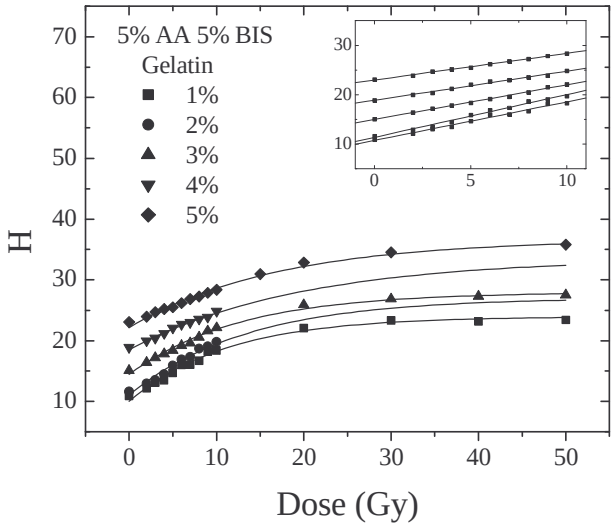

Figure 3.3 Dose response of PAGs with varying gelatin concentration.

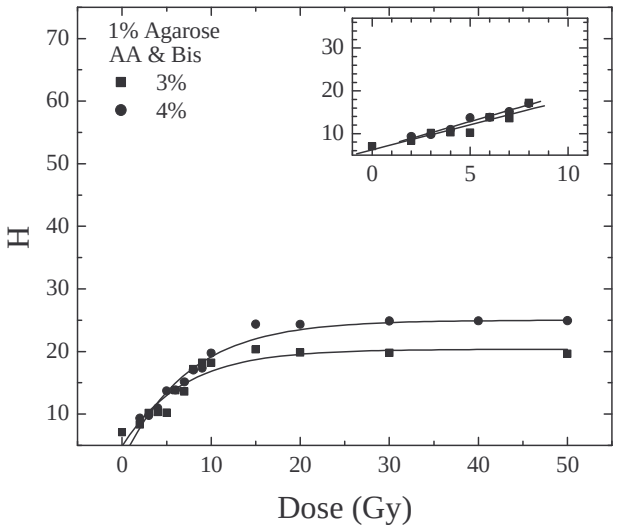

Figure 3.4 Dose response of PAA1 and PAA2.

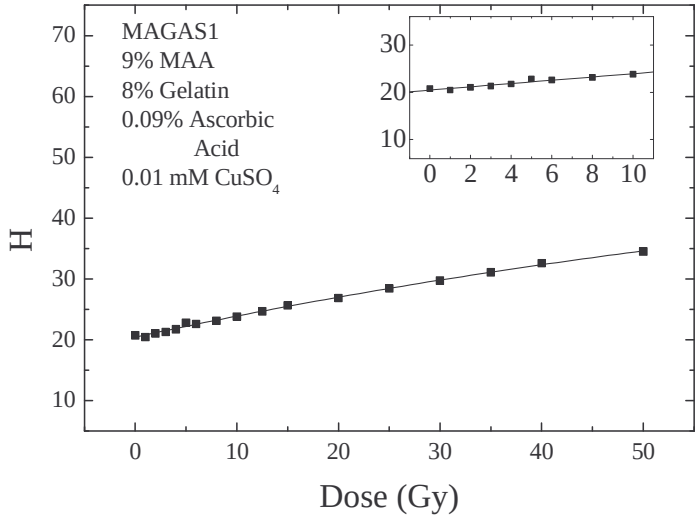

Figure 3.5 CT dose response of MAGAS1.

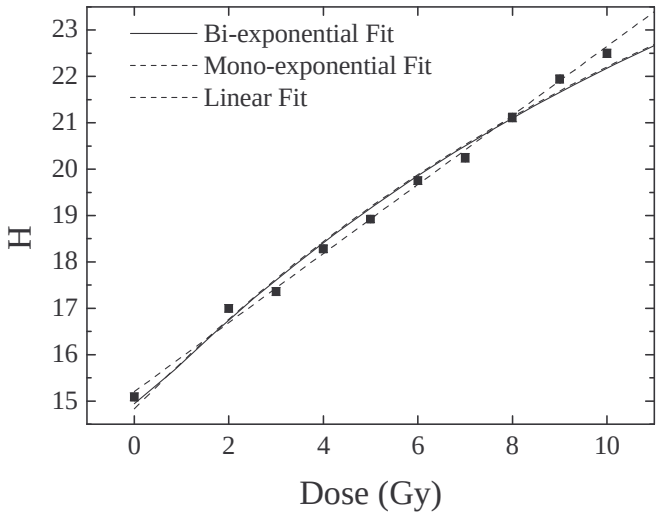

Figure 3.6 Data for PAG3 in the 0-10 Gy region with various functions fitted.

A comparison of Figures 3.1-3.3 and Table 3-1 shows that varying monomer concentrations (AA + BIS) affects both the overall CT-dose response and the CT-dose sensitivity. The CT-dose sensitivity can be increased by increasing the monomer concentration (Figure 3.1), with the limit being the ability to physically manufacture gels with high concentrations of monomers. Figure 3.2 shows that the monomers can be changed from AA to HEA and a response can be obtained with sensitivity close to that obtained with PAG.

A variation in the gelatin concentration (Figure 3.3) predominantly affects only the overall CT-dose response, i.e. the sensitivity and the shape of the curves are very similar; they are only shifted up or down the vertical axis with respect to each other (only '*y*' in Equation 3.1 is affected to any significant extent). If gelatin is replaced by agarose as the gelling agent there is a further increase in CT-dose sensitivity, however the overall CT-dose response tends to be shifted to lower CT numbers and there is a larger scatter of data points resulting in a greater uncertainty in the CT dose sensitivity (see Chapter 7).

The results for a normoxic gel shown in Figure 3.5 indicate that this class of gel dosimeter also produces a response when imaged with CT, however the dose sensitivity is relatively small in comparison to the other gels. Although the

concentrations of the chemicals in the normoxic gel can be varied, the mixture imaged in this chapter is close to that of the most sensitive measured with MRI [60] and it is expected that this will be the same with CT measurements. Figure 3.5 shows that the response for the normoxic gel tends to be approximately linear for a much greater range of doses than the other gel dosimeters investigated; however the total CT number range covered remains the same as for PAG gels. If future research produces a normoxic gel dosimeter with a greater sensitivity this type of gel dosimeter could potentially achieve widespread clinical use, i.e. easily produced 'on the bench top' and easily imaged with a CT scanner.

A previous research study has examined the CT dose response in the linear region and achieved a CT-dose sensitivity of $(0.86 \pm 0.04) \times 10^{-3}$ H Gy^{-1} for a polymer gel dosimeter composed of 5% gelatin, 3% BIS, 3% AA and 89% water [1]. In this work a comparable CT-dose sensitivity of $(0.71 \pm 0.02) \times 10^{-3}$ H Gy^{-1} for the same composition (Table 3-1) was obtained. The variation in dose response between PAGs produced at different research centres can be attributed to differences in production and handling procedures.

3.5 Chapter Summary

It has been demonstrated that the CT dose response of polymer gel dosimeters can be approximated by a linear relationship to doses of at least 10 Gy and an exponential relationship when higher doses are delivered. Varying the concentration of monomers in the polymer gel dosimeter will alter both the CT dose sensitivity and the range of the CT dose response, whereas altering the concentration of gelatin has little effect on these factors except the absolute value of the CT dose response tends to be shifted. Changing the gelling agent from gelatin to agarose results in a greater CT dose sensitivity but it is accompanied by a greater uncertainty due to increased scatter of the data points within the calibration graph. A CT signal can be obtained by using HEA instead of AA. A normoxic gel gave an approximately linear response over the whole dose range measured although the range of CT numbers was close to that of polymer gel. Varying the normoxic gel so that the active ingredients are consumed at a greater rate with increasing dose will provide a useful gel dosimeter which can be manufactured on the bench top and imaged with CT.

The results of this chapter have been published in the journal ‘Physics in Medicine and Biology’ [35] and in conference proceedings [61-64].

Chapter 4: Post Irradiation Photon Attenuation Properties

4.1 Introduction

In the previous chapter it was established that there is an increase in the CT number, *H*, of polymer gel dosimeters after irradiation. Equation 2.5 indicates that the increase in *H* is due to an increase in linear attenuation coefficient, μ. In this chapter the macroscopic cause of the increase in μ is investigated for a polymer gel dosimeter of a commonly used composition.

4.2 Background

From Equation 2.5 it can be seen that a CT image in polymer gel dosimetry can be considered to be a map of μ_{eff} of the polymer gel dosimeter. The change in CT number (the signal) after irradiation will be:

$$\Delta H = \frac{1000}{\mu_w}(\mu_1 - \mu_0) \qquad 4.1$$

where μ_0 and μ_1 are the linear attenuation coefficients of the gel dosimeter before and after irradiation respectively. A derivation of Equation 4.1 is included in Attachment 4.

It has been suggested that in polymer gel dosimetry the change in linear attenuation coefficient may be due to an increase in physical density, ρ post-irradiation [35], which may result in increased uncertainty in the absorbed dose and degradation of spatial resolution.

It is well known that the linear attenuation coefficient can be approximated by [65]:

$$\mu = N_e \sigma_e \rho \qquad 4.2$$

where N_e is the number of electrons per mass unit and σ_e is the cross sectional area per electron. In photon irradiation of gel dosimeters there should be no net addition of electrons and hence N_e will remain constant with irradiation. The mixture rule states that the mass attenuation coefficient, μ/ρ of a chemical compound or mixture can be approximately evaluated from the weighted sum of it's constituent elements [66] and can be written in terms of μ [66]. Above 10 keV errors in the mixture rule which result from ignoring the changes in atomic wave function due to molecular, chemical or crystalline environment of an atom are expected to be negligible [66], hence σ_e can be considered to remain constant. A function relating ΔH to a change in density can be obtained by combining Equations 2.5, 4.1 and 4.2 [67]:

$$\Delta H = \left(H_0 + 1000\right)\left(\frac{\rho_1}{\rho_0} - 1\right) \qquad 4.3$$

where H_0 is the CT number in the polymer gel dosimeter pre-irradiation and where ρ_0 and ρ_1 are the density pre- and post-irradiation respectively.

In this chapter direct measurements of μ and ρ are made to find the relationship between the two properties.

4.3 Materials and Methods

4.3.1 Polymer Gel Dosimeter

The polymer gel composition examined in this portion of the project was a PAG gel consisting of 5% gelatine, 3% bis, 3% AA, and 89% water. This particular combination of chemicals was used because it is one of the most widely used and currently the most representative of the polymer gel dosimeters. The method of production is outlined in Chapters 1 & 3.

After production the polymer gel dosimeters were poured into either polystyrene spectrophotometry cuvettes sealed with plastic stoppers (Sigma Aldrich, Sydney) for μ measurements, or glass volumetric flasks with capillary stoppers for ρ measurements. The particular cuvettes were chosen because they are of high quality and have parallel flat sides. The inner dimension of the cuvettes was measured with Vernier callipers to be 1.005 ± 0.001 cm and the wall thickness was measured to be 0.1050 ± 0.0006 cm where the error is the experimental standard deviation of the mean [68] of measurements of several cuvettes. Three batches of PAG were produced as detailed in Table 4.1.

Table 4.1 Batches of PAG produced for measurement

Sample	Parameter Measured	Day of Measurement (Post Irradiation)
PAG_{10}	μ and ρ	13-21 (ρ and μ measured on same day for each data point)
PAG_{11}	μ	19-25
PAG_{12}	ρ	3

To minimise the effects of oxygen contamination described in Chapter 1 the cuvettes and volumetric flasks were heat-sealed in pouches manufactured from 0.1 mm thick Barex sheets (Arbo Plastic Ltd, Switzerland) prior to removal from the nitrogen atmosphere of the glovebox. Prior to sealing the density flasks in their pouches the capillary stoppers were fixed to the flasks with Cellophane tape (3M, Sydney) to ensure they remained in place. The tape was placed such that it also extended over the hole of the capillary stopper. The low permeability of Cellophane to oxygen [69] gave additional protection from oxygen contamination through the capillary tube should the Barex pouch fail.

The pouches containing the cuvettes and density flasks of PAG were then cooled in a refrigerator at approximately 4 ℃ for 1-2 hours until a visual inspection revealed that they had gelled. They were then subsequently kept at ambient room temperature of 24 ℃ and irradiated in their Barex pouches after a further 1 hour.

4.3.2 Radiation Attenuation Measurements

Linear attenuation coefficient measurements of PAG and distilled de-ionised water were made at room temperature in narrow beam geometry using a steel collimator with lead and steel shielding (Figure 4.1) at the times shown in Table 4.1.

The radiation source used was ^{241}Am (Amersham, Sydney) which has a major photopeak at 59.5 keV [70]. This is close to the effective energy of most CT scanners. Electromagnetic radiation emitted by the source is listed in Table 4.2. Transmitted radiation was detected using a high purity germanium solid state detector (E G & G Ortec, Atlanta USA, model number GLP-25335/07) cooled with liquid nitrogen and with bias voltage of -1500 V. The amplifier used was an EG & G Ortec 572 with coarse gain of 50 and unipolar pulse with shaping time of 6 μs. Full-width-at-half-maximum (FWHM) of the pulse was measured with an oscilloscope to be 3 μs. Power was supplied by an Ortec 459 1500 V high voltage unit, and spectroscopy was performed using a Canberra Spectroscopy Amplifier model 1413 multichannel analyser, MCA (Canberra Industries, Meriden USA). The spectrum was analysed on a personal computer with Aptec MCA Application Multichannel Analyser software (Aptec Engineering Limited, Warrington USA).

Table 4.2 Electromagnetic Transitions of Americium-241 source (Amersham 1986)

This table is not available online.
Please consult the hardcopy thesis
available from the QUT Library

Cuvettes containing PAG dosimeters or de-ionised distilled water were placed in the cavity between the source and detector collimator as shown in Figure 4.1. The number of cuvettes was varied to enable measurement of attenuation through five different path lengths of the radiation beam. Transmission measurements through the same number of empty cuvettes were performed to determine the attenuation due to the cuvette walls.

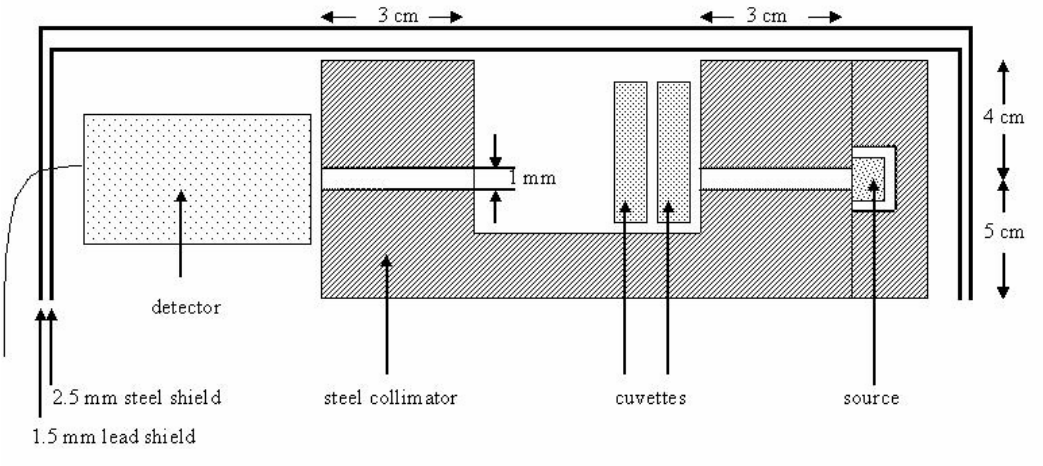

Figure 4.1 Geometry of the collimating apparatus for measurement of linear attenuation coefficient. The entire apparatus is surrounded by 2.5 mm steel and 1.5 mm lead shielding.

Also acquired at various intervals were repeated normalisation count rate measurements (see below) with no cuvettes in the radiation path. It was observed that the normalisation counts could vary by up to 2 percent each time the source was removed and replaced, illustrating the importance of the normalisation procedure. The normalisation also indicated if the set-up geometry changed during measurements through movement during the insertion of the cuvettes in the collimator. This ensured that corrupted measurements could be identified and disregarded in the calculation of μ.. Background counts were recorded with no cuvettes in the collimator.

Analysis of data was performed on a personal computer using Microsoft® Excel (Microsoft Corporation) and Origin® (Microcal Software, Inc).

4.3.3 Calculation of Linear Attenuation Coefficient

Background counts were subtracted from the recorded counts for each measurement. The remaining radiation count was recorded for cuvettes containing gel dosimeter or water and normalised to the count recorded for the same number of empty cuvettes. When a monoenergetic radiation beam passes through a material the intensity of the beam at any point within the material will be:

$$I = I_0 \, e^{-\mu x} \qquad 4.4$$

where I is the intensity of the beam, I_0 is the intensity of the beam incident on the material and x is the thickness of material through which the beam has passed. Taking the logarithm of both sides of Equation 4.4 gives:

$$\ln I = \ln I_0 - \mu x \qquad 4.5$$

i.e. $\ln\left(\frac{I_0}{I}\right) = \mu x$.

A plot of *ln I* against x should result in a linear relationship with a gradient of μ. Accordingly, the corrected value for the log of radiation counts, y was plotted against the radiation path length through the polymer gel dosimeter, t (see Figure 1.1):

$$y(t) = \ln\left(\frac{C_1(A(t)-B)}{C_2(A_0(t)-B)}\right) = \mu t \qquad 4.6$$

where A is the counts with water or PAG dosimeter in the collimator, A_0 is the counts with empty cuvettes in the collimator, B is the background counts, and C_1 and C_2 are the normalisation count rates as discussed in the previous section. The linear attenuation coefficient was calculated as the gradient of a weighted least squares fit of the data.

The uncertainty in y was calculated by a first order Taylor expansion of Equation 4.6 [68]:

$$\sigma_y^2 = \left(\sigma_A \frac{\partial y}{\partial A}\right)^2 + \left(\sigma_{A_0} \frac{\partial y}{\partial A_0}\right)^2 + \left(\sigma_B \frac{\partial y}{\partial B}\right)^2 + \left(\sigma_{C_1} \frac{\partial y}{\partial C_1}\right)^2 + \left(\sigma_{C_2} \frac{\partial y}{\partial C_2}\right)^2 \qquad 4.7$$

The uncertainty in t, σ_t was the experimental standard deviation [68] of repeated measurements. The uncertainty in the other parameters was taken as the square root of the recorded counts [71].

4.3.4 Density Measurements

Density was measured using glass volumetric flasks with capillary stoppers. Each flask was partially filled with polymer gel dosimeter. Density measurements for

each sample irradiated to a particular dose for PAG_{10} were made on the same day as its corresponding linear attenuation coefficient measurement and density for PAG_{12} was measured three days post-irradiation. Measurements were made at room temperature in an air-conditioned room (24°C).

The density of the gel in each flask can be determined from Archimedes' principle. When the flask is partly filled with gel and the remainder filled with water the volume of the flask, V is equal to:

$$V = V_{gel} + V_{wat} = \frac{m_{gel}}{\rho_{gel}} + \frac{m_{wat}}{\rho_{wat}} \qquad 4.8$$

where V_{gel} is the volume of the flask, V_{wat} is the volume of water required to fill the remainder of the flask when the gel is inside, m_{gel} is the mass of gel in each flask, m_{wat} is the mass of water required to fill the remainder of each flask after the gel had been poured inside, and ρ_{gel} and ρ_{wat} are the densities of the gel and water respectively.

Equation 4.8 becomes:

$$\frac{m_{tot}}{\rho_{wat}} = \frac{m_{gel}}{\rho_{gel}} + \frac{m_{wat}}{\rho_{wat}} \qquad 4.9$$

where m_{tot} is the mass of water that each flask could hold with no gel inside. The density of the PAG was subsequently determined by:

$$\rho_{gel} = m_{gel}\left(\frac{\rho_{wat}}{m_{tot} - m_{wat}}\right). \qquad 4.10$$

Uncertainty in the density measurement was calculated using a first order Taylor expansion of equation 4.10.

4.4 Results

4.4.1 Spectrum Analysis

Figure 4.2 is a graph of a typical energy spectrum obtained from the detector/source combination used in this work. All photopeaks listed in Table 4.2 can be identified. Within the spectrum there can also be seen a single x-ray escape peak at 49.5 keV which corresponds to K_α x-ray emission of germanium at approximately 9.9 keV (the main photopeak is 59.5 keV).

Also clearly visible in the spectrum is distortion due to tail pileup in the energy range 50-59 keV and peak pileup in the energy range 75-120 keV. The amplifier operates as a pulse height analysis system, i.e. the energy of a counting event is proportional to the number of electrons ejected and hence counted. Pileup occurs in pulse height analysis systems when the counting equipment counts several photons as one, and records the energy as the combined energy of both photons. Figure 4.2 indicates the occurrence of second order pileup, with no visible evidence of third order pileup above background rates in the spectrum.

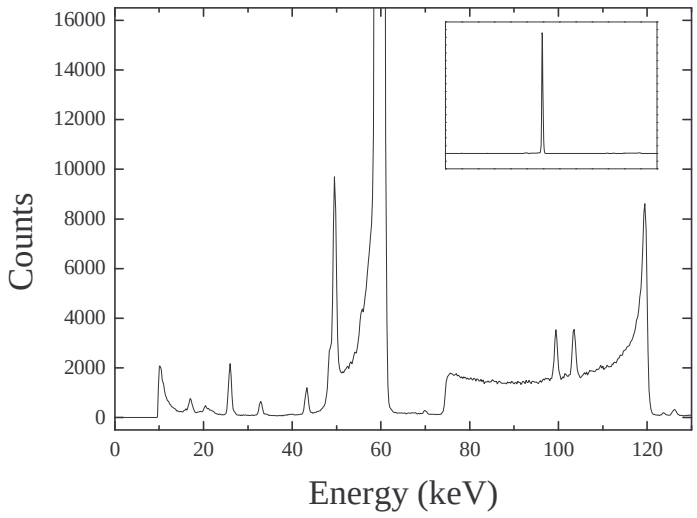

Figure 4.2 Energy spectrum obtained from the ^{241}Am radiation source. The main figure is windowed to show the main features and the insert shows the full spectrum. The features are discussed in the text.

An interesting feature of the spectrum is the lack of pile-up in the range 60-75 keV and can be explained as follows. The Ortec Model 572 Amplifier contains a built in pileup rejecter, which operates as a paralyzable system. Figure 4.3 is a representation of the timing relationship of the amplifier and pileup rejecter signals taken from [72]. In this system a fast logic pulse is generated when a counting event takes place and generates an inspection period. If a second event occurs within this inspection period an inhibit signal is generated to gate off the MCA and thus discard the distorted signal. However, the second event occasionally occurs within the resolving time of the gating circuitry (within the duration of the fast pulse) and it will not be detected as a separate pulse. The MCA then will not be gated off before the second pulse and constructive interference of the pulses occurs, resulting in both pulses being recorded as a single event with increased amplitude (Figure 4.4). The amplitude of the constructively interfering pulse will simply be the combined amplitude of the pulses at a given moment.

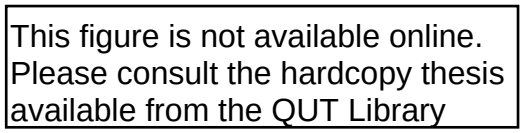

Figure 4.3 Diagram of the timing relationship of the E G & G Ortec 572 amplifier (Ortec 1994). At the occurrence of an event a fast pulse is generated in the gating (CRM) circuit and a 'busy' output occurs for the inspection time of the first pulse. If a second event occurs within this time it falls within the inhibit (INH) output time and will not be counted.

When the second event occurs within a relatively short time period of the first event, the peak of the second pulse will 'sit' close to the peak of the first pulse and the increased amplitude will be large (Figure 4.4), resulting in a larger recorded photon energy. If the second event occurs at a later time the second pulse will 'sit' further along the decaying tail of the first pulse, the constructive interference will be of lesser magnitude resulting in a lower combined pulse height, and the recorded energy will not be as great. Pileup in the spectrum can be seen in the range 75-120 keV because the resolving time of the gating circuitry is not sufficient to reject closely occurring events, i.e. those with large combined amplitudes. The circuitry can only reject events sufficiently spaced apart in time such that the second pulse sits further along the tail of the first, i.e. events with relatively small combined amplitudes. The occurrences which are rejected are those where the combined amplitude of the pulses is 75 keV or less and results in no pileup in this portion of the spectrum.

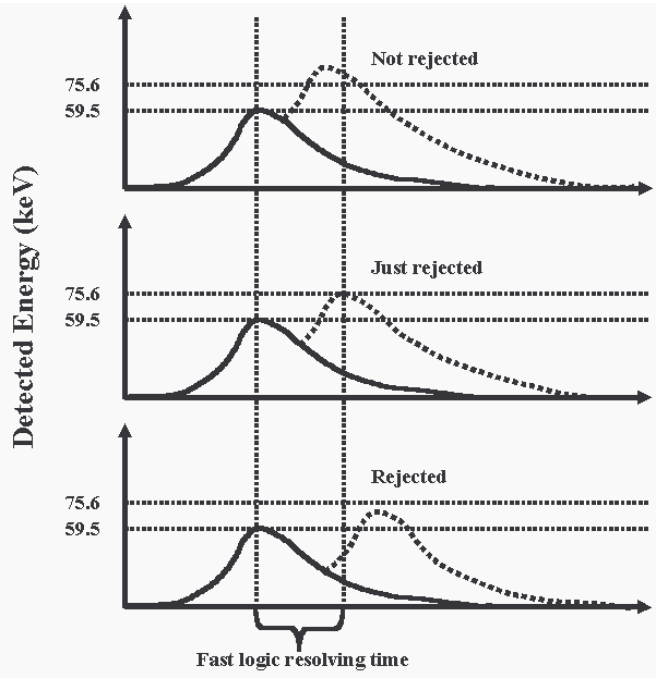

Figure 4.4 Representation of energy derived from pulse height analysis. If two pulses are very close together they will be recorded as a single pulse of high energy. The further apart the pulses are the lower the energy that is recorded. The resolution is described in the text.

The counts which were included for the purposes of attenuation measurements were those within the main photopeak (59.5 keV), those within the single escape peak (49.5 keV), and those within the distorted region (75-120 keV), allowing for counting of pile-up events. The minor photopeaks at 99 keV and 103 keV were not included in the count as they are emitted by the source (see Table 4.2). Dead time losses were corrected with the following equation [71, 73]:

$$r = n\, e^{n\tau} \qquad 4.11$$

where n is the true count, r is the counts registered, and τ is the time constant (the FWHM of the first lobe of the shaped pulse) [71]. Equation 4.11 was solved iteratively to obtain the true counts.

4.4.2 Linear Attenuation Coefficient and Density

Figure 4.5 shows a plot of the log of corrected count rate against the total path length through water as discussed in section 4.3.3. Also shown is a weighted least squares linear fit with a slope of 0.20868 ± 0.00021 cm^{-1}, which is the linear attenuation coefficient for distilled de-ionised water at the time of measurement of

PAG_{11}. As discussed in section 4.3.3 the linear attenuation coefficient was calculated as the gradient of a weighted least squares linear fit to the data.

Figure 4.6 shows the dependence of linear attenuation coefficient on radiation dose for PAG_{10} and Figure 4.7 shows the same for $PAG_{11.}$ A biexponential curve was fitted to the data for visualization purposes only. The CT dose response was discussed in Chapter 3 and as predicted by Equation 4.1 the figures indicate that linear attenuation coefficient has the same response as CT number with increasing dose.

Figure 4.8 shows the measured density for PAG_{10} and Figure 4.9 shows density for $PAG_{12.}$ Biexponential curves have again been fitted to the data for visualization purposes. These figures show that the density of the polymer gel dosimeters appears to increase in a fashion which can be approximated as linear with dose to at least 10 Gy, with further increases in density before reaching an upper plateau after approximately 30 Gy. The change in density with increasing dose appears to show the same response as both linear attenuation coefficient and CT number, confirming the prediction of Equation 4.3.

The density for the unirradiated polymer gel dosimeters were both measured to be 1.021 ± 0.005 g cm^{-3}. A previous study has indicated a density of 1.018 ± 0.001 g cm^{-3} for an unirradiated gel [74]. Differences in results between batches are expected due to small variations in preparation. Since this experimental work was completed and published [75] another study has reported density measurements for a gel dosimeter of the same composition using a gas pycnometer [76]. The study reported density with a range of approximately 1.034 g cm^{-3} for an unirradiated gel to approximately 1.047 g cm^{-3} for a gel with a dose of 50 Gy (compared to the present value of 1.033 ± 0.001 g cm^{-3}). The report attributed the difference as possibly being due to a portion of the gas in the pycnometer dissolving in their sample, thus causing an underestimation of their sample volume [76].

Figure 4.10 is a plot of linear attenuation coefficient against density for PAG_{10}, and Figure 4.11 is a plot of linear attenuation coefficient for PAG_{11} against density of PAG_{12}. A weighted least squares linear fit is shown. The least squares fit in Figure 4.10 has a P value of <0.0001 and r-square value of 0.99605 and Figure 4.11 has a P value of <0.0001 and r-square value of 0.99953**.** This shows that the function

relating absorbed dose to density is proportional to that of the linear attenuation coefficient. The linear attenuation coefficient and density data in Figure 4.11 were acquired at different times (see Table 4.1), indicating that the process in which density is measured is constant over the time range of the experiment.

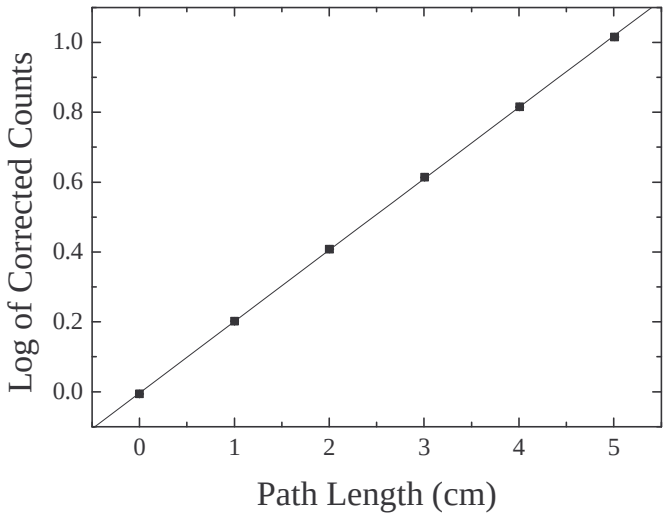

Figure 4.5 Plot of the natural logarithm of corrected counts versus path length. The linear attenuation coefficient is the slope of the graph.

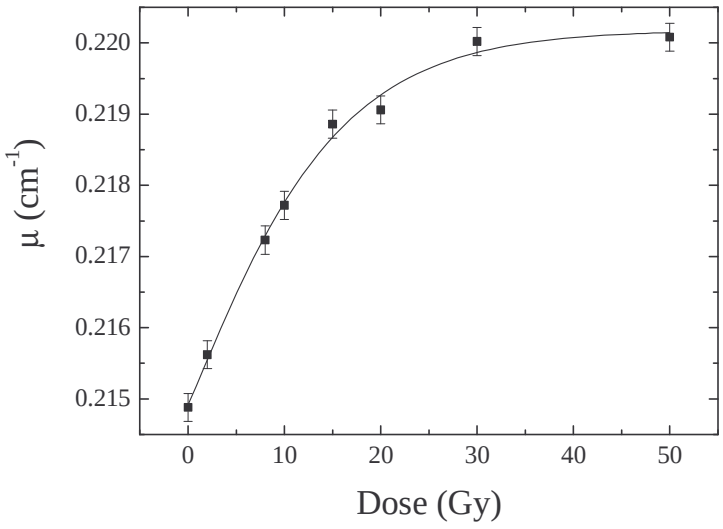

Figure 4.6 Plot of the measured linear attenuation coefficient of PAG_{10}.

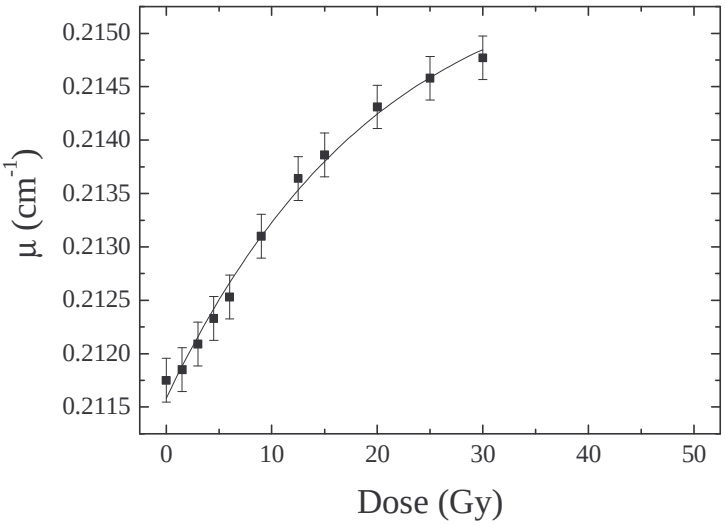

Figure 4.7 Plot of linear attenuation coefficient of PAG_{11}.

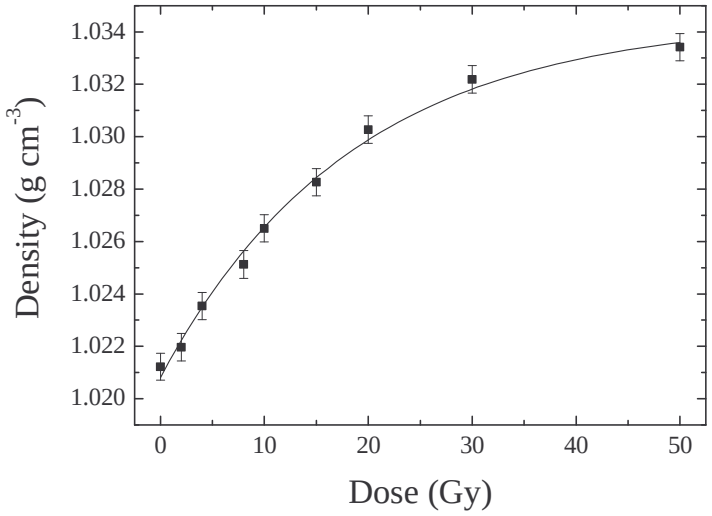

Figure 4.8 Density of PAG_{10}.

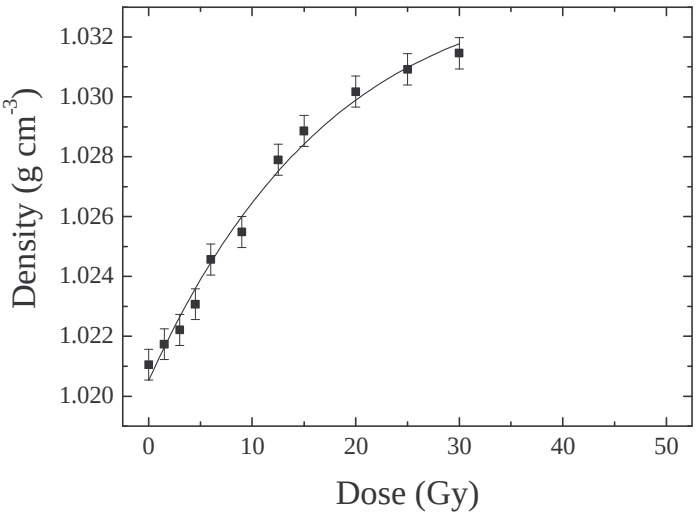

Figure 4.9 Density of PAG_{12}.

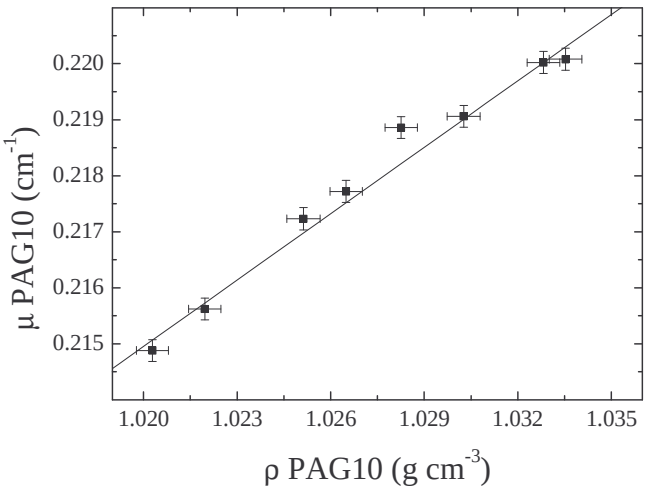

Figure 4.10 Plot of linear attenuation coefficient against density for PAG_{10}. A linear least squares fit has been added with a P value <0.0001 and r-square value of 0.99605.

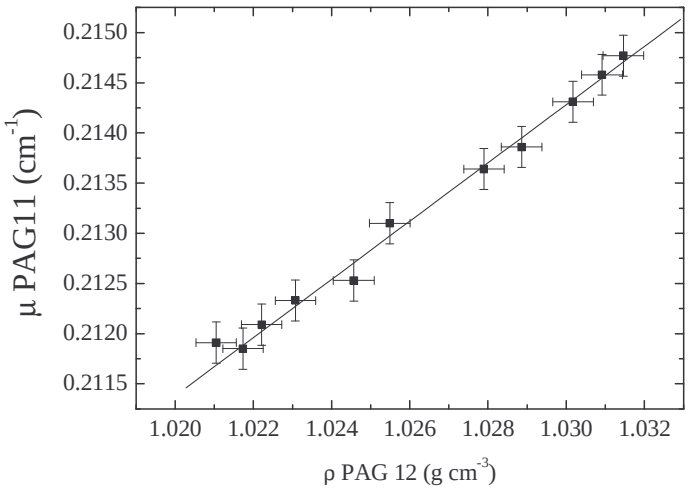

Figure 4.11 Plot of linear attenuation coefficient for PAG11 against density for PAG12. A linear least squares fit is added with a P value <0.0001 and r-square value 0.99953.

4.5 Discussion

It has been shown that linear attenuation coefficient is proportional to density, hence the CT signal is accompanied by a proportional change in density, and a CT image of a polymer gel dosimeter can therefore be considered to be a map of the physical density. As there is no addition of mass during the irradiation the increase in density is due to a decrease in volume and therefore some spatial change will occur within the gel post-irradiation. The decrease in volume indicates that the CT signal and spatial resolution are interdependent; however Figure 4.8 indicates that the density change for a fully polymerised gel is only about 1%. In practical use a polymer gel dosimeter would not be irradiated to full polymerisation or the dose resolution [77] would be degraded [35] (see also Chapter 7) and it is therefore not anticipated that the volume decrease would exceed spatial uncertainty requirements for most applications.

4.6 Chapter Summary

It has been shown that the post-irradiation CT signal of a polymer gel dosimeter is proportional to an increase in density. This results in some spatial

uncertainty and limits the attainable signal hence indicating that spatial resolution and dose resolution are competing factors.

The results of this chapter have been published in the journal ‘Physics in Medicine and Biology’ [75] and in conference proceedings [78-80].

Chapter 5: Imaging Parameters

5.1 Introduction

Chapter 3 established that CT gel dosimetry is a low contrast modality, indicating that image noise is a critical factor in reducing uncertainty in measurements of dose distributions within gel dosimeters. Noise can be reduced either during the image acquisition process through optimisation of scanner settings and procedures, or post acquisition through image processing. This chapter examines noise arising during acquisition and then Chapter 6 examines image processing techniques.

The imaging techniques employed during the previous chapters were sufficient when used to image calibration vials; however they must be improved upon when dose distributions in gel dosimeters are examined. In this chapter a more detailed background of the image acquisition process of CT is given than in previous chapters and techniques are examined to reduce noise arising during this stage of CT gel dosimetry.

5.2 Background

X-ray photons are produced and transmitted through the object being imaged (in this case the gel dosimeter) to be detected by a row of detectors. A portion of the photons will be attenuated by the gel dosimeter and a portion will reach the detectors. The number of x-rays which reach the detector are:

$$I = I_0 \, e^{-\int_{ray} \mu_{eff}(x)dt} \qquad 5.1$$

where I is the number of transmitted photons reaching a detector, I_0 is the number of incident photons in the ray sum, and $\mu_{eff}(x)$ is the effective linear attenuation

coefficient at the point x in the gel dosimeter. The line integral, l in Equation 5.1 can be estimated by:

$$\int_{ray} \mu_{eff}(x)\,dt = -\ln\left(\frac{I}{I_0}\right) = l \qquad 5.2$$

Each detector count can be considered to be a single set of data that obeys Poisson statistics with a variance of [41, 59]:

$$\mathrm{var}(I) = \langle I \rangle \approx I \qquad 5.3$$

In a well-maintained scanner the efficiency of the detectors should be approximately constant and therefore the number of photon flux detected by each detector should be proportional to the number arriving. The count obtained by each detector, I is normalized to I_0 which is the signal obtained by a reference detector (i.e. a detector whose position is such that the object is not in the path of the x-ray beam), and l is obtained. Each l is called a ray sum. The collection of ray sums of the individual detectors obtained for a particular x-ray tube position is referred to as a projection. A projection is an attenuation profile of the object for that particular 'viewing' angle. The source and detectors are then rotated by some small angular increment and the process is repeated.

For a large number of counts, the relative variance in I_0 compared to that in I is small, giving [41, 59]:

$$\mathrm{var}(l) = \mathrm{var}(I)\left(\frac{dl}{dI}\right)^2 \approx I\left(\frac{1}{I}\right)^2 = \frac{1}{I} \qquad 5.4$$

Detectors used in CT scanners are sensitive enough to detect small variations in the photon flux and hence small variations in ray sums. The relative uncertainty in the projection will therefore depend upon the number of photons transmitted through the gel dosimeter. When l along the path length is large, representing a heavily attenuating medium, the relative uncertainty in the photon flux will also be large. As an example, Figure 5.1 shows an exaggerated simulation of the attenuation of photons in a projection through a homogenous circle and the associated uncertainty of the counts. It can be seen that the outer regions of the figure, representing ray sums that

do not pass through the circle, have a smaller uncertainty than the inner regions. From Equation 5.4 it can be seen that increasing the initial number of photons will increase the number of transmitted photons, thereby decreasing the relative uncertainty across the whole projection. In low contrast situations such as gel dosimetry, there is relatively little variation between ray sums, and a large number of photons must be counted to ensure the relative uncertainty in each ray sum is small enough to distinguish the small variations in μ throughout the gel dosimeter.

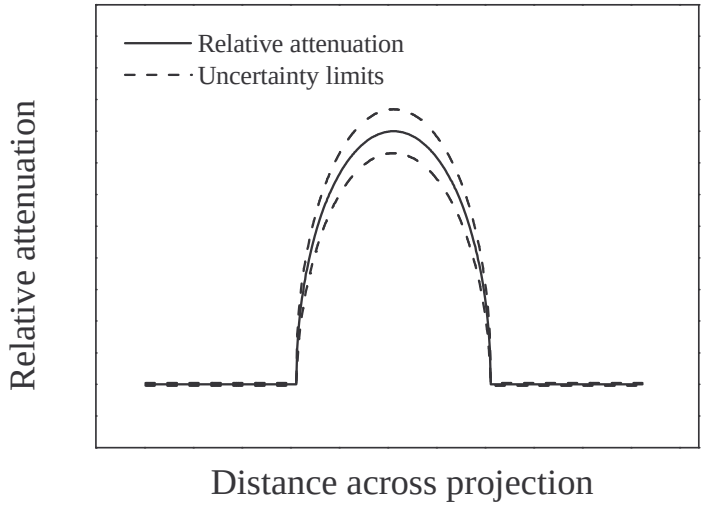

Figure 5.1 Exaggerated relative attenuation profile through an homogenous circle. The dashed lines represent stochastic uncertainty.

When a sufficient number of projections are obtained they form a matrix, with each projection represented by either a column or row. This matrix is termed a sinogram and is the radon transform of a map of the linear attenuation coefficients within the object and its surrounds. This matrix of projection data is then used to reconstruct the image. Upon reconstruction, the net result is the 'smearing' of all projection data (after some manipulation such as filtering) across the image in it's original acquisition geometry. This process causes the noise components in each projection to be propagated across the image in 'spokes' [81], the final result being the effect that noise in one point of the final image is related to noise in other points of the image which have a common ray sum with the point in question. The result is that CT noise is correlated.

The map of the linear attenuation coefficients (the image) is produced through techniques such as filtered back projection or algebraic reconstruction. The production of the map is commonly referred to as 'image reconstruction', however the use of the word 'reconstruction' is misleading as it implies that the image had existed previously, which is not the case. The image is actually the inverse radon transform of the projection matrix, much the same as an MRI image is the inverse Fourier transform of the signal obtained in that modality. However, the convention of referring to the process as reconstruction will be maintained.

Throughout this chapter the signal to noise ratio (SNR) refers to the mean pixel value of a region of interest divided by the standard deviation of the pixel values, σ_H. As stated previously, projection data can be considered to be a series of radiation measurements and as such the variance is given by Equation 5.4, with the measured photon intensity in a particular scanner for each projection dependant upon the electron current within the x-ray tube, *i*, the exposure time for each projection, *s*, and the x-ray photon energies, *E*. The mean pixel value within a region of interest, *p* should not change when the number of counted photons changes, and the SNR is therefore inversely proportional to the number of photon flux. If a number of images are acquired in identical geometry and averaged together, the total number of photons measured is dependent upon the number of images averaged and the SNR becomes:

$$SNR_{proj} = \frac{g(E,i,s,p)}{Var(I)} = \sqrt{n}\ \ g(E,i,s,p) \qquad 5.5$$

where *n* is the number of images averaged and *g* is an arbitrary function. When the images are obtained with identical settings on the same scanner (which is calibrated and well maintained) *g* becomes a constant. The SNR of the average of corresponding projections of a series of images can therefore be approximated as being proportional to the number of images in the series.

5.3 Stochastic Noise

From equation 5.4 it can be seen that stochastic noise can be reduced by counting a large number of photons in each projection. An increase in the photons detected in a CT scanner is achieved through either an increase in photon energy or tube output or both, where tube output in this document refers to tube current, *i* multiplied by exposure time, *s*. Tube output can be increased by increasing either the tube current or the exposure time by averaging several images together. This is a limitation in patient scans as increasing tube output also increases patient dose, however, in gel dosimetry a large number of repeated scans can be obtained without inducing a radiation dose sufficient to cause significant further polymerisation the gel dosimeter. Shown in Figure 5.2 is a plot of the amplitude of total noise in a CT image similar to Figure 2.5 with an increasing number of images averaged together. (The noise in Figure 5.2 is taken from images acquired on a relatively new Picker PQ5000 scanner where ring artifacts are much less prominent than seen in Figure 2.5. Images were acquired using a technique of 140 kV and 600 mAs per slice.) As the number of images averaged together is increased the amplitude of the stochastic noise component shows a $n^{-1/2}$ relationship and a function of that type has been fitted to the figure. This confirms the prediction of a $n^{1/2}$ dependency of SNR as seen by equation 5.5. However, it must be noted that there may be other sources of noise, such as electronic noise, which show the same relationship as stochastic noise with dose. Proof of this for any scanner is obtained by comparison of the number of noise-equivalent quanta (NEQ) which is the total effective number of x-ray quanta detected per unit distance along the projections [82]. NEQ will vary between scanners.

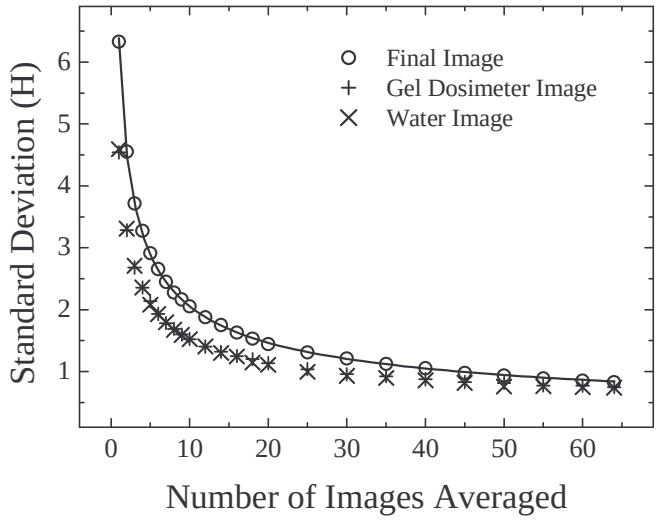

Figure 5.2 Standard deviation of pixel values within the water tank as seen in Figure 2.5. It can be seen that subtraction of one image from another as discussed in Chapter 2 increases the stochastic component of image noise. An inverse square function has been fitted.

Figure 5.2 shows that the subtraction technique described in Chapter 2 causes an increase in the stochastic noise component of an image due to combination of the uncertainties in the gel image and the water image. The stochastic component of noise becomes:

$$\sigma_f = \sqrt{\sigma_i^2 + \sigma_s^2} \qquad 5.5$$

where σ_f, σ_i and σ_s are the amplitudes of stochastic noise in the final image, the initial image, and the subtracted image respectively. Therefore many images must be averaged to ensure that σ_i and σ_s are small enough that σ_f is small in comparison to non-stochastic noise.

5.4 Structured Noise

It can be seen that the noise in Figure 5.2 does not approach zero as the number of images averaged becomes large. This remaining noise is non-stochastic and has been attributed to effects such as CT number quantization and other system noise [83]. The total noise in a CT image is [83]:

$$\sigma_H = \sqrt{\sigma_0^2 + \sigma_f^2} \qquad 5.6$$

where σ_H is the standard deviation in pixel values in the final image and σ_0 is the amplitude of the non-stochastic noise. In this section the cause of non-stochastic noise is investigated through computer simulations and by experiment.

5.4.1 Simulations

Simulations were performed using the Image Processing Toolbox of Matlab® software version 6.0.0.88 Release 12 (The Mathworks, Inc) to examine the effects of pixel size in the final image.

To examine noise in image reconstruction, two simulations were performed. The first simulation represents various field of view (FOV) settings on a scanner during acquisition, and the second simulation represents an acquisition with small pixel sizes after which adjacent pixels are grouped. Projection data through a homogenous circle (the inverse of Figure 5.1) was simulated.

In the first simulation, projection data of 1024 ray sums per projection, with 720 projections were produced and various amplitudes of Gaussian noise were added. The noisy projection data was grouped into pairs of ray sums and pairs of projections, which were averaged, producing data with 512 ray sums per projection and 360 projections. The process was repeated with groups of 4 ray sums and 4 projections to produce data with 256 ray sums per projection and 180 projections. All subsequent sets were produced from the original data set, ensuring that the same random numbers used in the noise generation were applied to all data sets, representing the same simulated photon fluxes. The three data sets were then used to reconstruct three images having pixel matrix sizes of 1024^2, 512^2 and 256^2 respectively. Reconstruction was performed using the inverse radon transform function contained in the Image Processing Toolbox of Matlab® with a ramp filter.

In the second simulation, the first reconstructed image from the first simulation was used (the image reconstructed from the 1024 ray sum per projection data). In this simulation pixels in the reconstructed image were grouped into 2 x 2

pairs and 4 × 4 pairs and averaged to produce larger pixel sizes, again resulting in three images having pixel matrix sizes of 1024^2, 512^2 and 256^2 respectively.

Both simulations produced pixels and images of the same size, however the first simulation represents grouping of data prior to reconstruction (FOV settings varied on the scanner) and the second simulation represents grouping of data after reconstruction (post acquisition).

5.4.2 Experimental Investigation

To experimentally examine the effect of pixel size several images of a 12 cm diameter plastic bottle filled with water were acquired. The images were acquired on a GE CT/*i* scanner with a technique of 120 kV and 100 mAs per slice. Image sets were acquired with a field of view of 25 cm and reconstruction matrix sizes of 256 × 256 pixels and 512 × 512 pixels. The pixels in the image set with 512 × 512 pixels were grouped into 2 × 2 pairs to produce a 256 × 256 matrix, identical to the procedure used for the simulations in the previous section. This allowed comparison of noise to be made for pixels representing the same physical dimensions but obtained by the different methods described in Section 5.4.1. Regions of interest of the same physical location of each image were selected and their σ_H was measured.

5.4.3 Simulation Results

5.4.3.1 Uncertainty due to noisy projection data

Figure 5.3 and Figure 5.4 show graphs of the signal-to-noise ratio, SNR of the simulations of reconstruction of the homogenous circle. Figure 5.3 represents the case where grouping of pixels was performed on the projection data, and hence prior to image reconstruction, and Figure 5.4 represents the case where grouping was performed after reconstruction of the image. The region of interest chosen represented the same data in each set, i.e. representing the same physical boundaries within the object simulated.

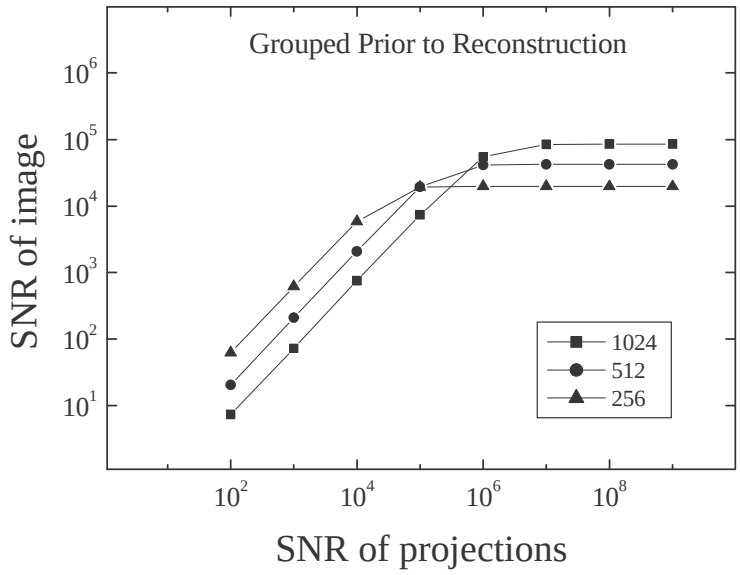

Figure 5.3 SNR in an image of a homogenous circle when data is grouped prior to reconstruction. The '1024' data represents the image reconstructed as 1024 × 1024 pixels. '512' and '256' follow the same convention.

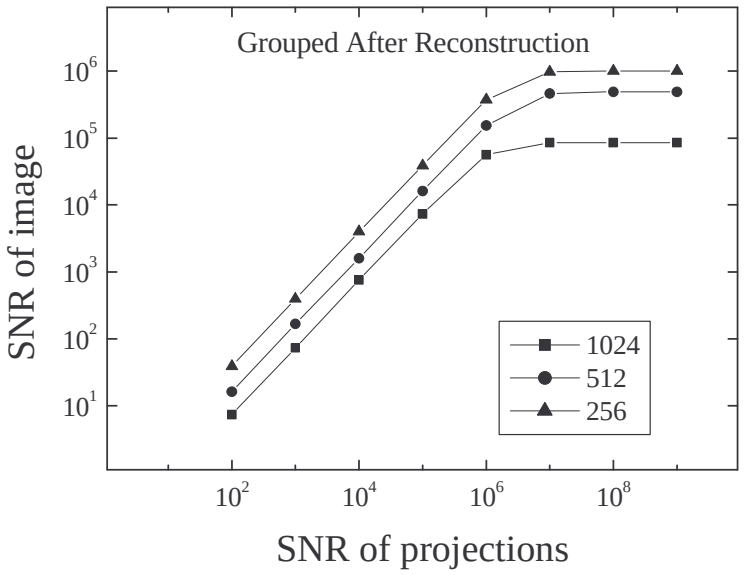

Figure 5.4 SNR in an image of a homogenous circle when data is grouped after reconstruction. The naming of each data set is by the same convention as Figure 5.3.

In Figure 5.3 and Figure 5.4 the effect of the stochastic component of image noise can be seen in the left side of the graphs, i.e. the portion where the SNR in the projection data is below 10^6. As the SNR in the projection data increases it can be seen in the figures that the SNR also increases in the final image due to the lesser relative uncertainty of effectively increased photon counts in the detectors and is consistent with the results of Figure 5.2. It can be seen that smaller pixel size (i.e. larger pixel matrix size) decreases the SNR due to an increase in σ_H of the final image. The increase in σ_H with smaller pixel sizes is due to a smaller number of photons passing through each voxel, thus increasing the relative uncertainty. Previous literature has examined the relationship between spatial resolution and stochastic noise [81, 84, 85] and has shown that the square of stochastic noise varies inversely with the cube of spatial resolution when the voxel size is constant, i.e. representing the same physical dimensions in space. The result is that the final image has a greater SNR when the pixel size is large.

Figure 5.5 compares the '512' data from Figure 5.3 and Figure 5.4. It can be seen that there is little difference in σ_H between grouping of data before or after reconstruction in the stochastic noise region of the graphs. Both methods result in the same pixel size representing the same photon flux per pixel and therefore the same σ_f.

In the case where SNR in the projection data is large it can be seen in Figure 5.5 that significant improvement in the SNR of the final image can be achieved by grouping the pixels after reconstruction. This will be discussed in the next subsection.

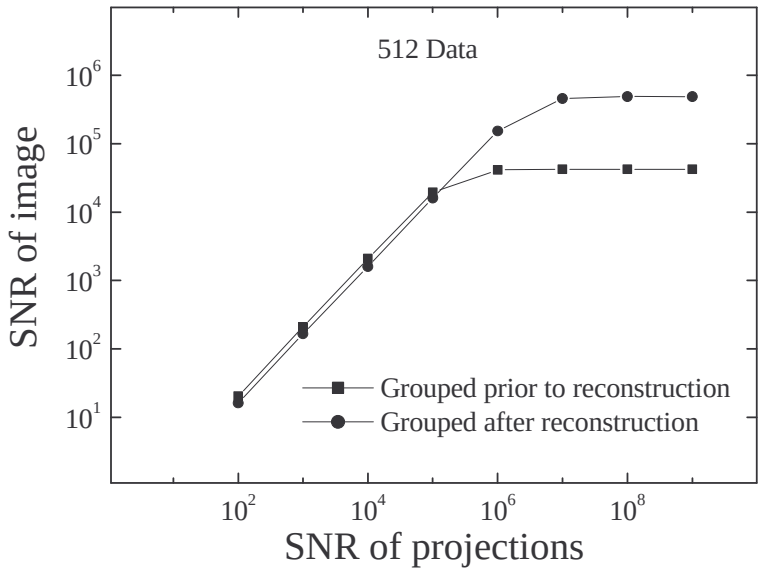

Figure 5.5 Comparison of the results for '512' data from Figure 5.3 and Figure 5.4.

5.4.3.2 Uncertainty due to image reconstruction

Increasing the number of detected photons will not entirely eliminate noise in a CT image [83]. If the noise amplitude in a CT image is plotted against the mAs the remaining noise can be estimated through simple extrapolation of the plot in the low mAs region [83]. This can be seen in the high SNR region of the graphs in Figure 5.3 and Figure 5.4 where increasing SNR (low noise) prior to reconstruction has an upper limit to the noise reduction which can be achieved in the final image.

This underlying noise is artifactual, and is generated in the inverse radon transform process during the image reconstruction phase. This component of image noise is dependent upon the number of ray-sums and projections used in the reconstruction of the image and is therefore a sampling artifact. In the filtered back projection method of image reconstruction projection data is filtered and ‘smeared’ across the image in the same geometry as it’s acquisition. When there is a less than infinite number of projections, or a less than infinite number of data in each projection, a moiré pattern will result.

Figure 5.6 to Figure 5.10 are the images generated in the simulations discussed previously, but without noise added to the projection data. The figures are windowed

to show the same pixel ranges. Figure 5.6 to Figure 5.8 represent the grouping of data prior to reconstruction, the results of which are seen in Figure 5.3. Figure 5.9 and Figure 5.10 represent grouping after reconstruction with the results seen in Figure 5.4.

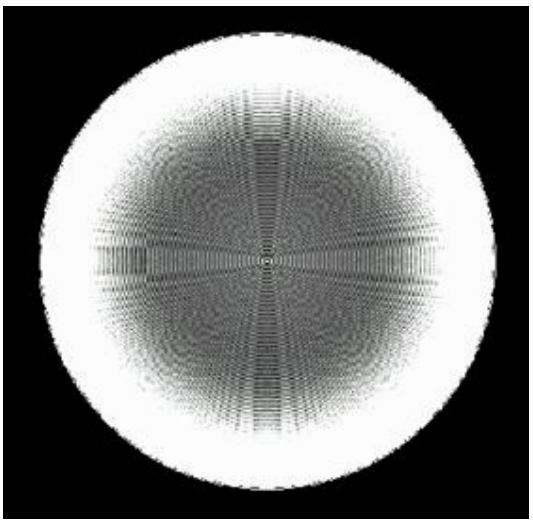

Figure 5.6 Reconstruction of an image of a circle with 1024×1024 pixels.

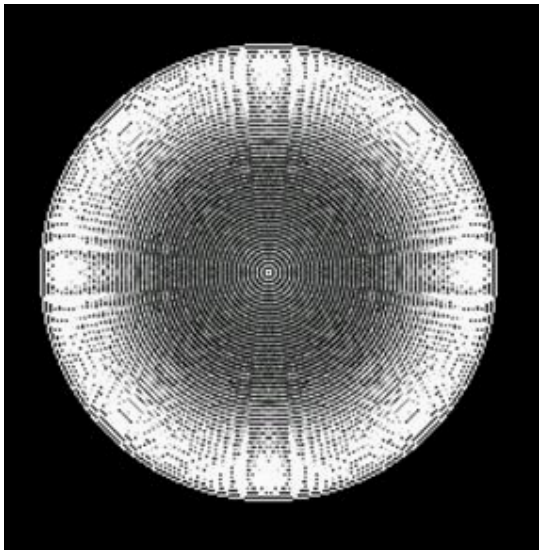

Figure 5.7 Reconstruction of an image of a circle with 512×512 pixels.

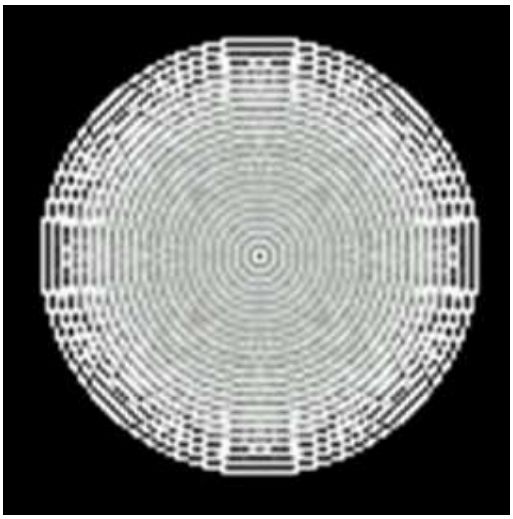

Figure 5.8 Reconstruction of an image of a circle with 256×256 pixels.

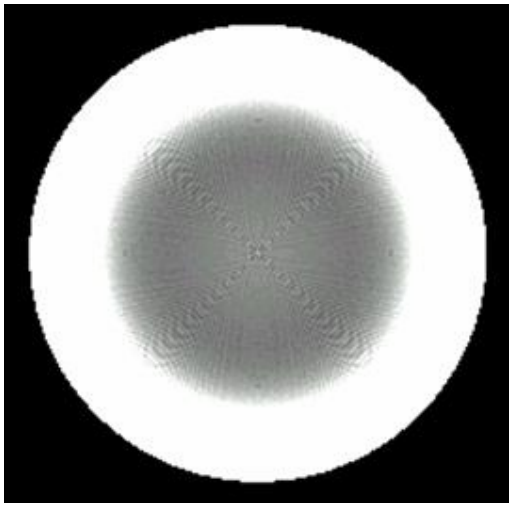

Figure 5.9 Image of the circle seen in Figure 5.6 after the pixels have been grouped to 2×2 sets.

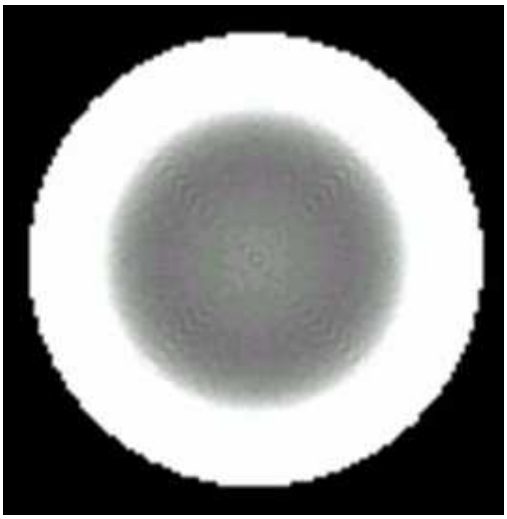

Figure 5.10 Image of the circle seen in Figure 5.6 after the pixels have been grouped to 4×4 sets.

Figure 5.6 to Figure 5.8 show that as the number of noiseless projections and amount of data in each projection decreases, the resulting moiré pattern becomes coarser and the amplitude of the individual streaks becomes greater, thereby increasing the variance of pixel values in the image. This results in the major contribution to σ_0. Further scanning beyond the stochastic noise range will not show any significant improvement to σ_H as the variance in this region is caused by the reconstruction itself. The result is seen in the right half of the graphs in Figure 5.3. However, grouping of data after reconstruction has a much-improved result on the SNR in the final image. Figure 5.4 shows that the SNR achieved through grouping after reconstruction has a significant improvement over grouping prior to reconstruction. The visual difference can be seen by comparison of Figure 5.7 and Figure 5.9.

5.4.4 Experimental Results

Figure 5.11 and Figure 5.12 show averages of 100 images of a water filled bottle as described in 5.4.2. Figure 5.11 shows the result when the image is reconstructed in a 512×512 matrix and then grouped into 2×2 pixel groups and Figure 5.12 shows a reconstruction in a 256×256 matrix. Both images are windowed to the same level. The subtraction technique described in Chapter 2 has not been performed. This was done in order to amplify and therefore better demonstrate the experimental results. A qualitative inspection of the images shows that moiré patterns

are more prominent close to the edges of the phantom in Figure 5.12 than in Figure 5.11 and is consistent with the results of the simulation. In the centre of the phantom there visually appears to be little difference between the images except that the ring artifacts are more defined when the image is reconstructed in larger matrix size and pixels subsequently grouped.

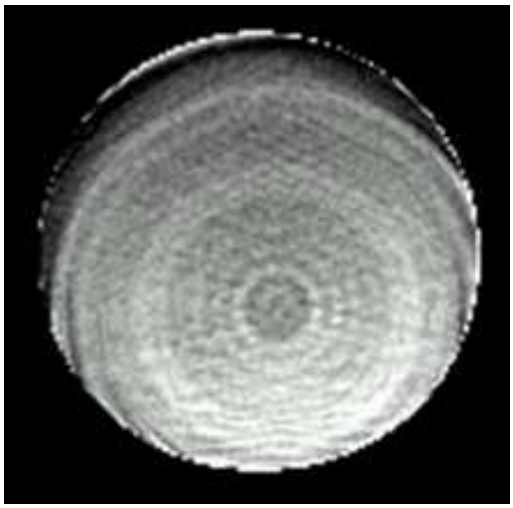

Figure 5.11 Image of a plastic bottle filled with water and without performing image subtraction. Original image was 512 × 512 pixels and has been reduced to 256 × 256 by grouping of pixels.

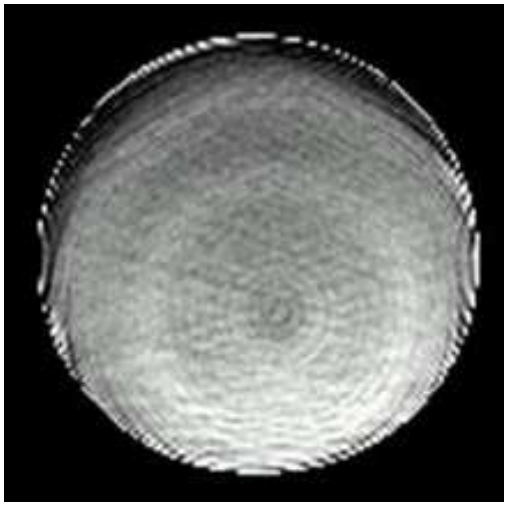

Figure 5.12 Image of a plastic bottle filled with water and without performing image subtraction. The image was acquired as 256 × 256 pixels.

A quantitative examination of experimental data can be seen in Figure 5.13 and Figure 5.14. In these figures the 'x axis' is proportional to the SNR of the projection data as described by Equation 5.5. Figure 5.13 shows comparison of SNR for an ROI close to the edge of the phantom and Figure 5.14 shows the same

comparison for a ROI close to the centre of the phantom. The figures are experimental representations of the simulation of Figure 5.5. The inserts of the figures show σ_H plotted against number of images averaged. Comparison of the figures shows differing results. When a ROI is measured close to the edge of the phantom the two data series cross, therefore showing the same trend as predicted by Figure 5.5, however this is not the case at the centre of the phantom. The difference can be attributed to coarser moiré patterns at the phantom edge seen in Figure 5.8 and Figure 5.12 and it appears that there is some radial dependency of the structured noise. This indicates that in polymer gel dosimetry the most important region of irradiation should ideally be located in the centre of the phantom during imaging to maximise the effectiveness of noise reduction.

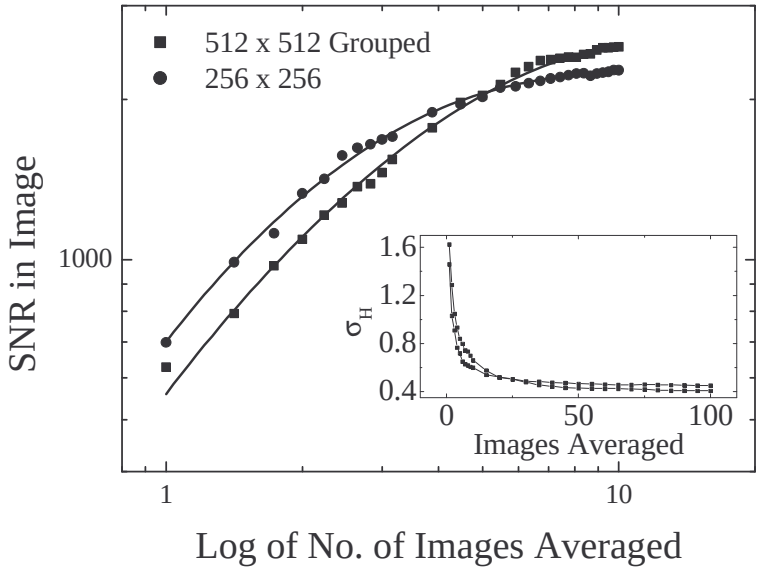

Figure 5.13 SNR in a ROI taken close to the edge of the phantom seen in Figures 5.11 and 5.12. The "x axis" is approximately proportional to SNR in projection data. The insert shows a plot of σ_H against number of images averaged. See text for details.

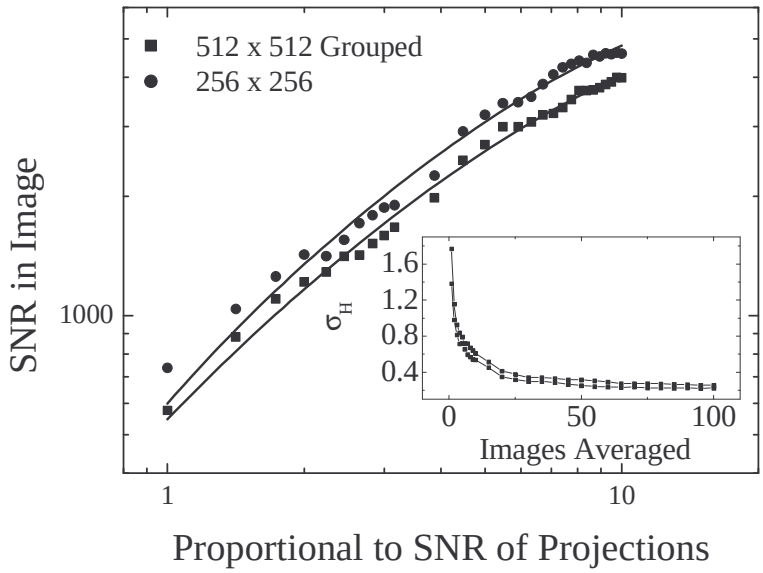

Figure 5.14 SNR in a ROI taken close to the centre of the phantom seen in Figures 5.11 and 5.12. The "x axis" is approximately proportional to SNR in projection data. The insert shows a plot of σ_H against number of images averaged. See text for details.

The experimental results indicate that reconstructing the image on a coarse 256×256 matrix has the advantage of slightly less stochastic noise. Conversely, if a large number of images are obtained and averaged the 256×256 image results in greater structured noise, however application of the image subtraction method described in Chapter 2 will reduce the structured noise. On the other hand, image reconstruction on a finer matrix gives the user practically the same set of data as reconstruction on a coarse matrix as well as an additional set of data (albeit noisier) with better spatial resolution. In fact, a technique has been recently published where the researchers used two superimposed data sets to image a gel dosimeter [36]. (It should be noted that although the technique does not involve varying spatial resolution within the data set, the point is made that addition of different quality images can be made to provide an improved final image.)

5.5 Chapter Summary

Stochastic noise in CT gel dosimetry can be reduced by averaging several images together. When the subtraction technique described in Chapter 2 is applied the

stochastic noise will be increased by a factor of $2^{1/2}$, however if a sufficient number of images are averaged stochastic noise will approach zero.

There is a lower limit to noise in a CT image which has been known since the 1970s. It has been shown that the main cause of this ‘noise floor’ is due to moiré patterns in the reconstruction.

Data can be grouped into sets of pixels either before or after reconstruction. Grouping of data prior to reconstruction is an automatic process within the scanner when the image is reconstructed as a coarser matrix and has slightly improved noise reduction in noisy images. In applications such as gel dosimetry numerous slices can be acquired as there is no concern for patient dose; and the slices can be averaged to virtually eliminate stochastic noise, leaving only the artifactual noise due to image reconstruction. In this case it has been theoretically shown that the most efficient option in reducing noise is to acquire the slices at best spatial resolution, or smallest pixel size, and group the pixels after reconstruction to achieve the spatial resolution requirements of the particular application.

The results of this chapter have been published in conference proceedings [78].

Chapter 6: Image Processing

6.1 Introduction

Chapter 5 established methods for reducing residual noise in a CT image of a polymer gel dosimeter by optimising scanner settings and techniques. Although the signal to noise ratio can be dramatically improved there may arise some situations where the noise still needs further reduction, or there may be limits to the improvement which can be achieved. In these situations the image itself may require further manipulation through filtering. Filtering an image is not without its disadvantages however; as the benefits gained through noise reduction may be costly in terms of spatial resolution or vice versa.

In this chapter an image processing algorithm is designed which utilizes combinations of several commonly available filters to reduce image noise whilst maintaining fine detail. The algorithm and individual filters are tested for their suitability for use in CT gel dosimetry. Comparisons in performance of the algorithm and filters are made using a previously published quantitative testing method. The same method is then used to compare the performance of the algorithm and filters by the simulation of filtering an image representing an irradiated gel dosimetry phantom. Finally, a pilot study of the technique is performed by applying the image processing algorithm to a real CT image of a gel dosimetry phantom.

6.2 Background

The common filters used in this chapter are the averaging filter, the median filter, and the adaptive Wiener filter. These filters are easily designed and readily available on software packages such as Matlab®. In this section each filter is described and in the following section an algorithm combining the common filters is designed.

6.2.1 The Averaging Filter

The averaging filter (AVE) simply assigns the mean value of a neighbourhood of pixels to the central pixel of each neighbourhood:

$$b = \frac{1}{q}\sum z \qquad 6.1$$

where b is the output pixel value, q is the number of pixels in the neighbourhood, and z is the value of each pixel in the neighbourhood. This filter is a lowpass filter, which performs best in homogenous image regions with Gaussian noise. Edges or sharp points in the image will be blurred and some loss of information may occur in these regions.

6.2.2 The Median Filter

The median filter (MED) assigns the median value of pixels in each neighbourhood to the central pixel. In this filter the greyscale pixel values within the neighbourhood are sorted into a list of ascending or descending order. The central pixel value of the list is assigned to the central pixel of the neighbourhood. The median filter is much less sensitive to extreme values than the averaging filter, has good edge preserving effects and performs well in removing “salt and pepper” type noise. However, fine image detail may be lost. If a median filter is repeatedly applied to an image, a root signal will be found for which further median filtering will have no effect [86].

6.2.3 The Adaptive Wiener Filter

The adaptive Wiener filter (WIEN) varies the amount of filtering applied to a neighbourhood according to the local image variance. If there is a large variance within the local neighbourhood, such as at an edge, there is little smoothing. On the other hand, if there is little variance more smoothing is performed. The algorithm used in Matlab® software is:

$$b(p_1, p_2) = w + \frac{\sigma^2 - v^2}{\sigma^2}(\alpha(p_1, p_2) - w) \qquad 6.2$$

where $b(p_1,p_2)$ is the output pixel value, w is the mean of the pixel values in the local neighbourhood, σ^2 is the local variance of pixel values in the neighbourhood, v^2 is the noise variance in the image, and $\alpha(p_1,p_2)$ is the input value of the local neighbourhood [45]. The Wiener filter acts very well as a noise reducing filter in homogenous image areas and has good edge preserving effects, however, noise around edges tends to receive little filtering

6.3 Methods

All image processing and simulations in this chapter were performed on a personal computer using the Image Processing Toolbox in Matlab® software version 6.0.0.88 Release 12 (The Mathworks, Inc), and hence all filters and random number generators used are those which are included in that particular software.

6.3.1 Image Processing Algorithm

The image processing algorithm designed in this chapter is diagrammatically represented in Figure 6.1, with an example of each step shown in Figure 6.2. The basic premise of the method is to break the image down into low and high frequency components to take advantage of the different performance characteristics of common filters, for example in Figure 6.2 the adaptive Wiener filter performance is improved by removing the low frequency components of the image (the step) through subtraction, resulting in a greatly reduced value for v^2 in Equation 6.2.

In the first step the low pass characteristic of the averaging filter is used to deliberately blur the edge of the object. The blurred image is then repeatedly filtered with a separable median filter until the root signal is found [87]. A separable median filter is simply a median filter which filters the horizontal and vertical elements of an image separately, rather than the usual case of neighbourhood blocks. The advantage of this method is the enhanced noise removal along edges that run parallel with either of the filtering directions of the filter [45].

After the root signal of the low-pass filtered image is obtained, it is subtracted from the original image to obtain a difference image as shown in Figure 6.2 to reduce v^2 as discussed above. The adaptive Wiener filter is then applied to the difference image to smooth out noise whilst maintaining edge information. In this algorithm the adaptive Wiener filter is operated in a similar fashion to the separable median filter. This ensures that along edges parallel to the filtering direction there will be heavy smoothing, whilst edges perpendicular to the filtering direction receive little filtering.

The filtered difference image is then added to the root signal of the lowpass filtered image to obtain the reconstituted image. If it is known *a priori* that there are no expected extreme points in the true signal, then some limited median filtering can be used to further remove any remaining noise.

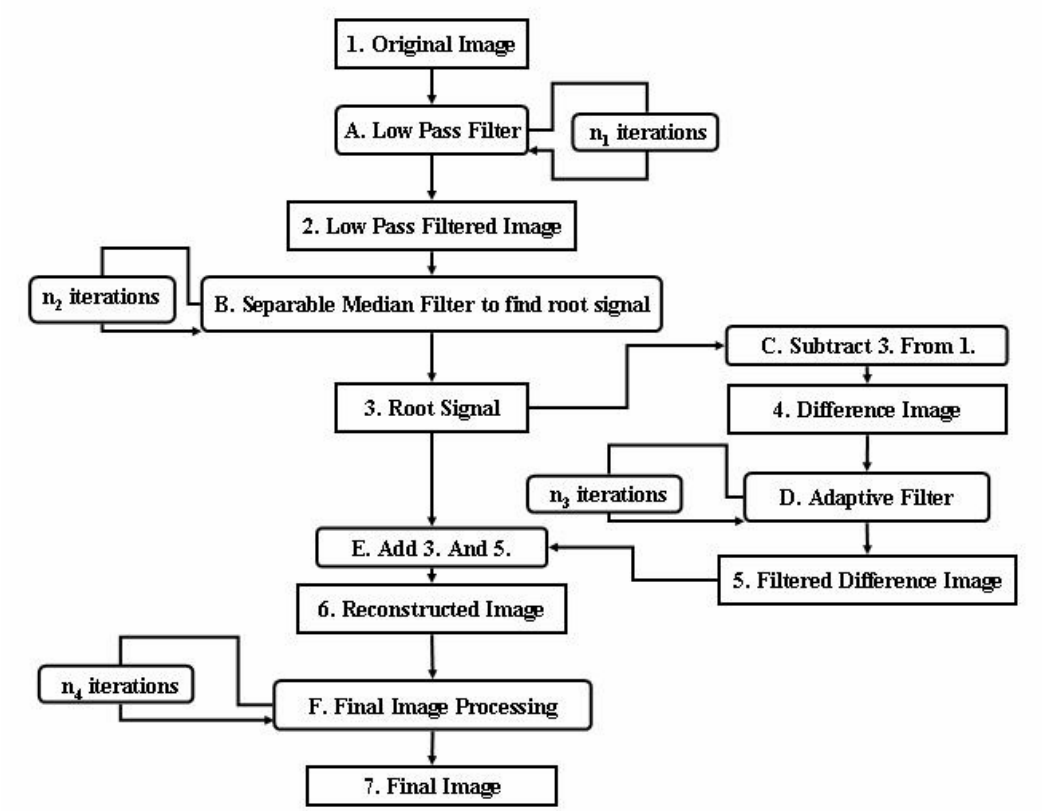

Figure 6.1 Diagrammatic representation of the image processing method used in this chapter.

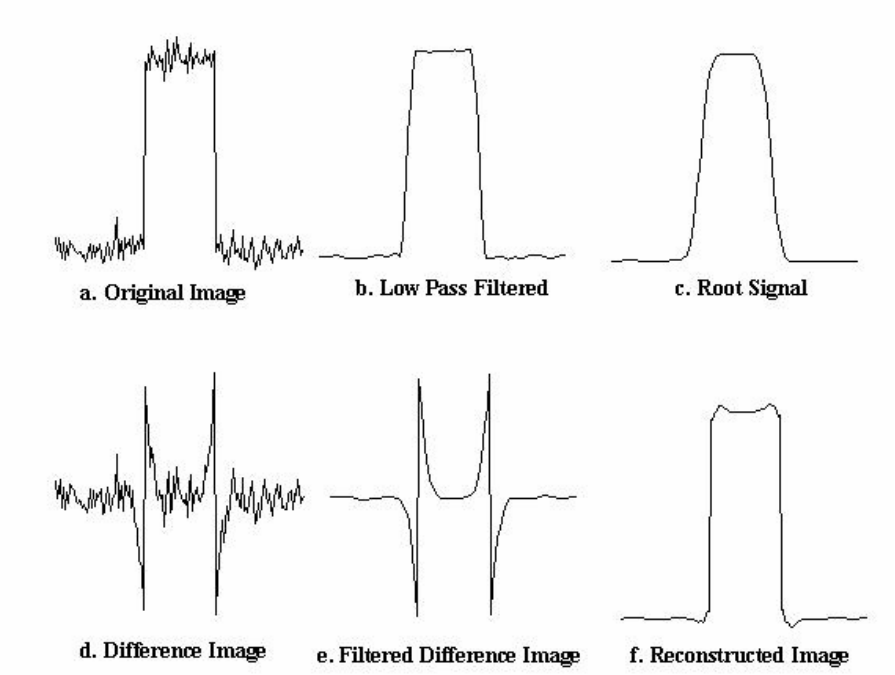

Figure 6.2 Demonstration of various stages of the image processing method on a noisy image.

6.3.2 Test Image

To test the performance of the filter a method was used which is similar to that applied by Chin & Yeh and Du Buf & Campbell [88, 89] which was adapted from Fram and Deutsch [90]. In this method a uniform disc is generated on a uniform background as shown in Figure 6.3. The edge of the disc has a variable gradient. The image size is 64×64 pixels and the radius of the disc is varied to examine the high spatial activity performance of the filtering algorithm. Gaussian noise was added to the image using the random number generator in Matlab® as seen in Figure 6.4. Care was taken to ensure the random number generator was reset between each test to ensure identical noise conditions.

In the method of Chin and Yeh the test image contains a region of high spatial activity around the edge of the disc and a region of low spatial activity away from the edge. To separate these regions a mask image was generated as shown in Figure 6.5. The mask image contains only two grey levels, each level corresponding to either high or low spatial activity. In the mask image used here, the high spatial activity

region included all pixels within a radius of ± 2 pixels of the edge slope as shown in Figure 6.5.

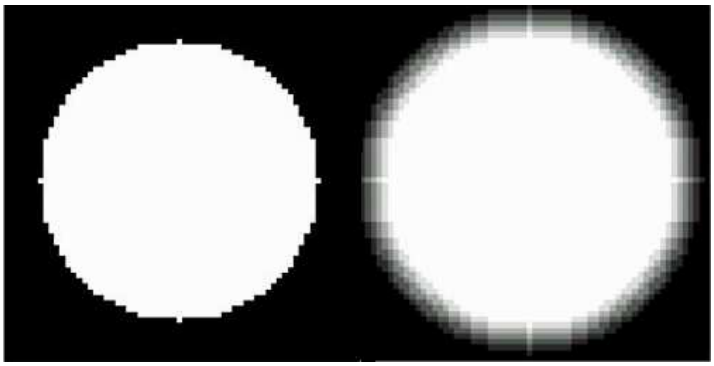

Figure 6.3 Test image with step edge (left) and 60 degree slope (right).

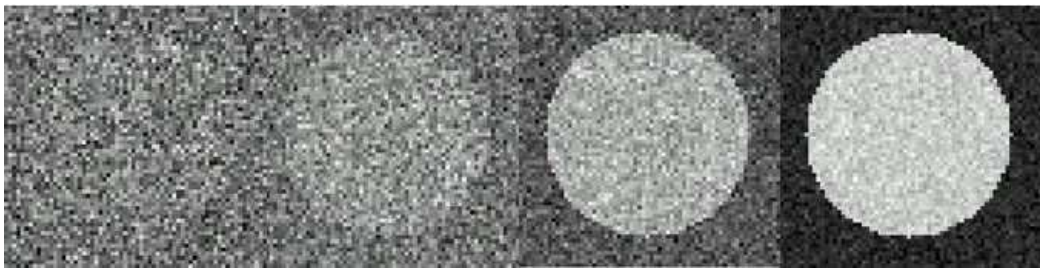

Figure 6.4 Test image with added noise resulting in SNR of 0.1, 1, 10 and 100 (left to right).

Figure 6.5 Mask image used to separate high and low spatial activity regions. The mask on the left is of a step edge and the mask on the right is of a 75 degrees edge.

The performance of a filter can be determined by the relative error in low or high spatial activity areas, ε_l or ε_h. The relative error is obtained by following the procedures of du Buf and Campbell. The test image is denoted I_1, the noisy image is denoted I_2, the filtered image is denoted I_3, and the mask image is denoted M. The relative error can be calculated as:

$$\varepsilon_i = \frac{\sum_{S_i} (I_3 - I_1)^2}{\sum_{S_i} (I_2 - I_1)^2}, i \in \{l, h\} \qquad 6.3$$

where S is the subset of pixels. If the filtering gives a perfect result the relative error will be 0.0, if the filtering results in no net improvement the relative error will be 1.0, and if the filtering results in a worsening of the image the relative error will be greater than 1.0 [89]. Pixels within a border two pixels wide from the edge of the image were not included in the evaluation process.

The test image was modified in various ways to examine filter performance under different conditions. The signal to noise ratio (SNR) was varied in the range 0.1 to 300. To achieve this the greyscale intensity within the radius of the disc, z_1, was set at a level of 10, the greyscale intensity of the surrounding background, z_2, was set at a level of 0 and the variance of the added noise, ω^2 was adjusted to obtain the desired SNR according to:

$$SNR = \left(\frac{z_1 - z_2}{\omega} \right)^2 \qquad 6.4$$

The slope of the edge was varied from 90° to 60°, where 90° is a step edge. When the slope of the edge was other than 90° the disc was varied such that the radius of the disc at z_1 (the top) remained constant, and the radius of the disc at z_2 (the bottom) varied according to the slope.

The central radius of the disc was varied to compare the performance of the algorithm designed in this chapter with that of the commonly available filters outlined above. The performance of the filters could then be compared operating on fine detail, for example, a median filter retains edges very well of a disc with a 25 pixel radius, however, information may be lost when the radius is very small.

6.3.3 Simulation of an Irradiated Phantom

To examine the performance of the image processing algorithm and the filters in an environment more closely related to gel dosimetry than the test image of the

previous section, an image of an irradiated gel dosimetry phantom was simulated, processed and evaluated.

The simulation shows the expected dose response of a polymer gel dosimeter in a 20 cm diameter circular phantom irradiated with three intersecting 5×5 cm 6 MeV photon beams. The first beam simulates a dose of 12 Gy and the other beams simulate doses of 8 Gy rotated 60° and 210° from the first. The beam values assume a dose sensitivity of 1 H/Gy [91]. Percentage depth dose data was calculated using measured values in water with an ion chamber from a Varian Medical Systems Clinac 600C linear accelerator located at Queensland Radium Institute, Mater Hospital, Brisbane. Beam penumbra data is taken from Johns and Cunningham [92]. Noise was generated using a random number generator and had a variance of 1.0 H. The example contains low to moderate spatial activity expected from non conformal radiotherapy.

A quantitative analysis of the performance of the image processing algorithm and the filters was completed using a modified version of the method described in Section 6.3.2. The same comparison of the noiseless image, noisy image and processed image was made by the use of Equation 6.3, however only pixels within the radius of the simulated phantom were evaluated. This made certain that only the effect of the simulated dose distribution contributed to the evaluation. To ensure that edge effects did not interfere with the results, pixels within a six pixel radius of the edge of the simulated phantom were excluded from the test.

For qualitative display isodose contours were overlaid on figures of the treatment plan, the processed image, and some of the images filtered with the common filters.

6.3.4 Pilot Study - Imaging of a Phantom

As a pilot study into the image processing technique, as well as the techniques discussed in Chapters 2 and 5, a gel dosimetry phantom was produced, irradiated, imaged and image processed.

6.3.4.1 Polymer Gel Manufacture

A gel dosimeter was produced in a nitrogen filled glovebox according to the procedures described previously and consisted of 5% gelatin (by weight), 4% BIS, 4% Acrylamide and 87% water. This formulation was chosen as it was expected, from the data of Chapter 3, to produce suitable dose sensitivity whilst remaining stable throughout production. The gel was poured into a 1.5 litre plastic container with a diameter of 15 cm. The container was sealed in Barex prior to removal from the glovebox to prevent oxygen contamination. The phantom was then cooled in at 4°C for 5 hours prior to irradiation.

6.3.4.2 Irradiation

The gel dosimeter phantom was removed from its Barex pouch and irradiated with three intersecting 2 cm × 4 cm 6 MV photon beams using a Varian Medical Systems Clinac 600C linear accelerator. Each beam had a dose of 4 Gy at d_{max}. The three beams were at angles of 0°, 30° and 90° and the centre of rotation was the centre of the phantom. This geometry gave regions of superposed radiation doses from one, two and three beams.

6.3.4.3 Imaging

Imaging was performed on a GE CT/*i* scanner using the water tank and technique described in Chapter 2. The phantom was imaged with a technique of 120 kV, 100 mAs per slice, a slice width of 10 mm and a field of view of 25 cm with 512 × 512 pixels. One hundred and fifty images were obtained of the phantom in the water tank and the same number of images was obtained of water. Further images were not taken due to time constraints on access to the scanner.

6.3.4.4 Post Acquisition Processing

Images were transferred to a personal computer and processed with Matlab® software. The water images were averaged and then subtracted from the averaged phantom images to reduce statistical noise as described in Chapter 5 and artifacts as described in Chapter 2. After the 512 × 512 subtracted image was produced the pixels in each image were grouped into 2 × 2 pairs as described in Chapter 5 to produce a

256 × 256 image. These grouped images were then processed with three passes of the image processing algorithm.

6.4 Results

6.4.1 Image Processing/Filtering

The individual parameters of the filtering method were tested to establish optimal neighbourhood size and number of iterations of each of the individual filters to be used within the algorithm (see section 6.4.1.1). To examine the validity of the testing method, the results of the common filters applied individually to the test image are compared to those previously published by Chin and Yeh and du Buf and Campbell [88, 89] (see section 6.4.2).

6.4.1.1 Effect of Filtering Parameters within the Algorithm

The pixel neighbourhoods and number of iterations of each step in Figure 6.1 was varied to examine their individual effect on the filtering algorithm, and the results are shown in the following figures for regions of high and low spatial activity. These tests were performed on a disc with 25 pixel radius, edges of 90°and 75° with SNR of 100.

6.4.1.1.1 Neighbourhood Size

Figure 6.6 shows the result when the neighbourhood of the averaging filter (step A, Figure 6.1) is varied. When there is high spatial activity the algorithm performs best with a small neighbourhood due to the lowpass nature of the averaging filter. With low spatial activity the performance declines to a greater error as the neighbourhood increases before gradually improving at large neighbourhood sizes.

Figure 6.7 shows that when the median filter (step B, Figure 6.1) is increased in size the performance oscillates in both high and low spatial activity regions, with best performance occurring in neighbourhood sizes of odd numbers (giving a definite median value within the neighbourhood). Figure 6.7 shows that the optimal performance in high spatial activity neighbourhoods occurs at a size of 5 pixels

whereas low spatial activity performance is best with large neighbourhoods. Examination of the scales shows that the performance is generally much better in low spatial activity neighbourhoods and therefore priority should be given to the high spatial activity regions, indicating that a 5 pixel median neighbourhood should be chosen.

Figure 6.8 shows that when the Wiener filter (step D, Figure 6.1) neighbourhood is increased the high spatial detail performance improves until a neighbourhood size of 3 is reached after which a decline in performance is observed. The adaptive nature of the Wiener filter means that the relative local variance will be greater around edges with small neighbourhoods and Equation 6.2 indicates that original data will be filtered to a lesser extent thus better retaining edges with small neighbourhoods than large. The low spatial detail performance oscillates in small neighbourhoods until a steady improvement is reached at those of larger size. In this case a small neighbourhood with an even number of pixels produces the best result.

In the final step of post reconstruction median filtering (step F, Figure 6.1) the performance of the algorithm is again seen to oscillate for high spatial frequency regions when the median filter neighbourhood is increased, with best performance being in neighbourhoods of odd size as seen in Figure 6.9. The best performance is obtained in a neighbourhood of 1 pixel, i.e. when this step is not applied. In low spatial activity areas the performance oscillates with increasing neighbourhood size with different rates of improvement of performance for odd and even numbered sizes. The selection of neighbourhood size for this step is a trade-off between high and low spatial activity performance.

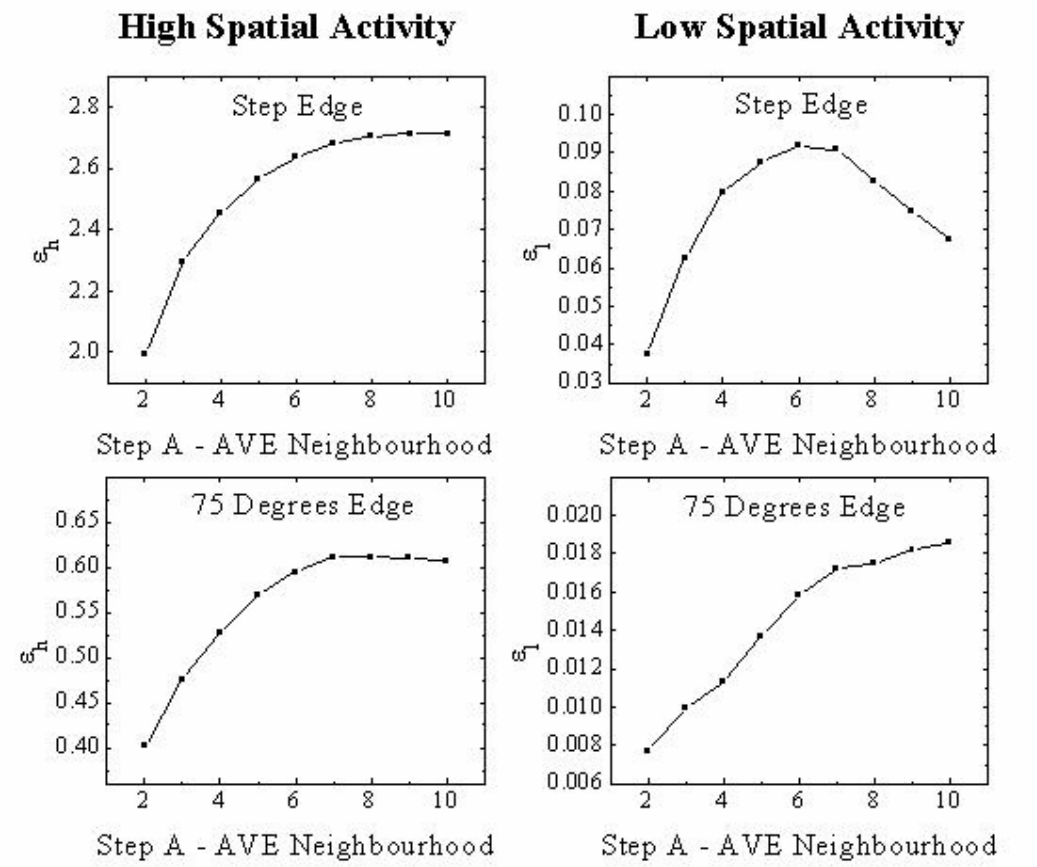

Figure 6.6 Error of the filtering algorithm when the averaging neighbourhood size is varied. High spatial activity regions are on the left and low spatial activity regions are on the right. Step edge is on the top row and 75 degrees edge is on the bottom row.

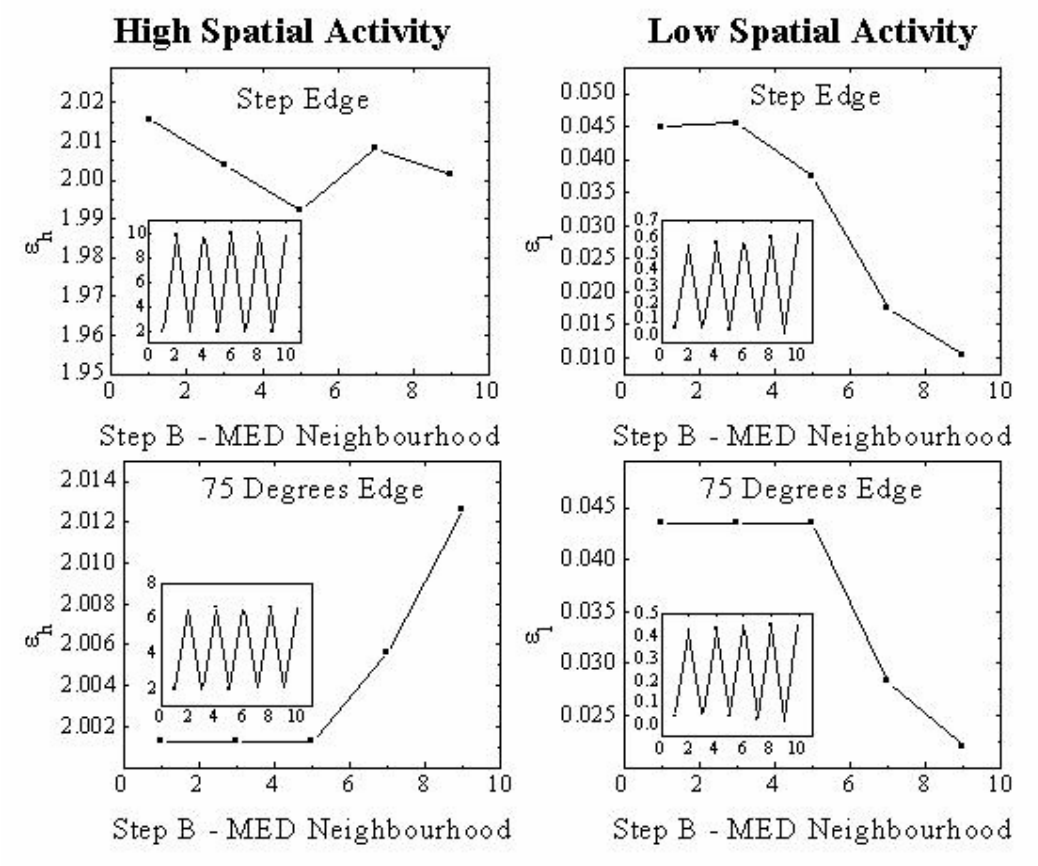

Figure 6.7 The relative error in performance of the filtering algorithm when the median filter neighbourhood is varied. The main graphs show results for odd dimension neighbourhoods, whereas the inserts show the oscillations that occur when both odd and even neighbourhoods are used.

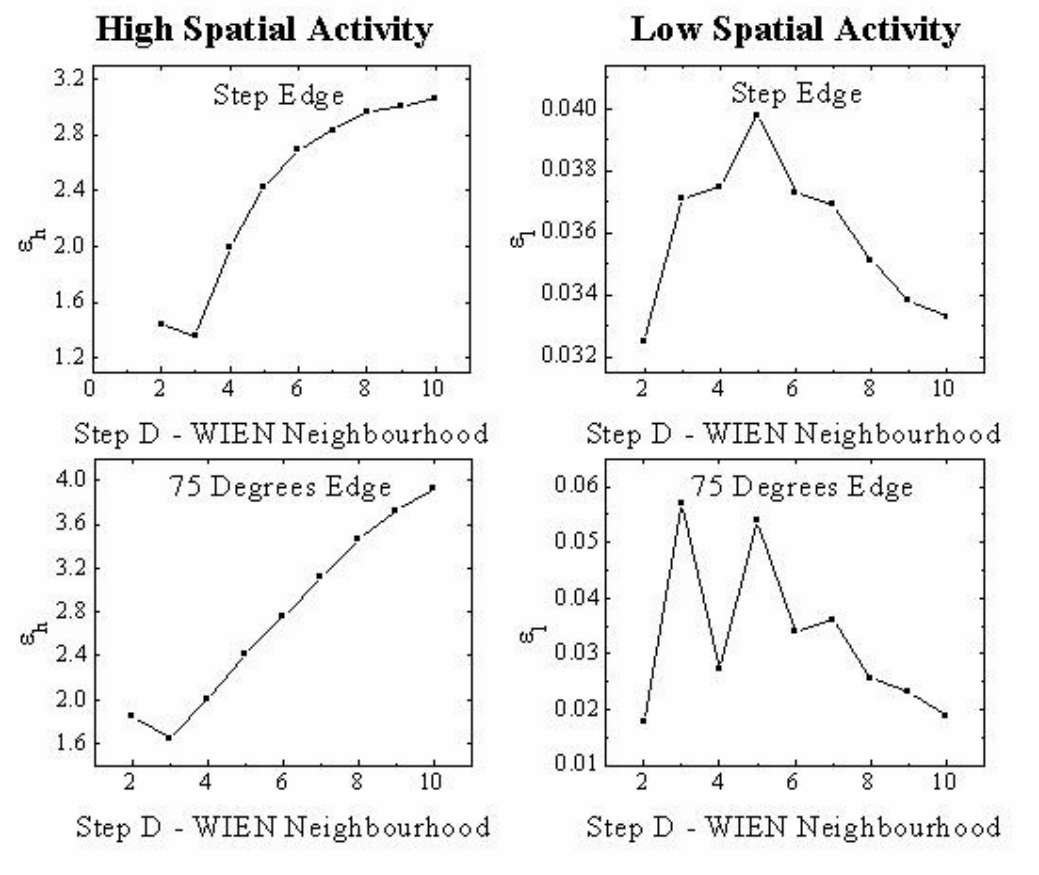

Figure 6.8 Relative error when the size of the Wiener filter neighbourhood is varied.

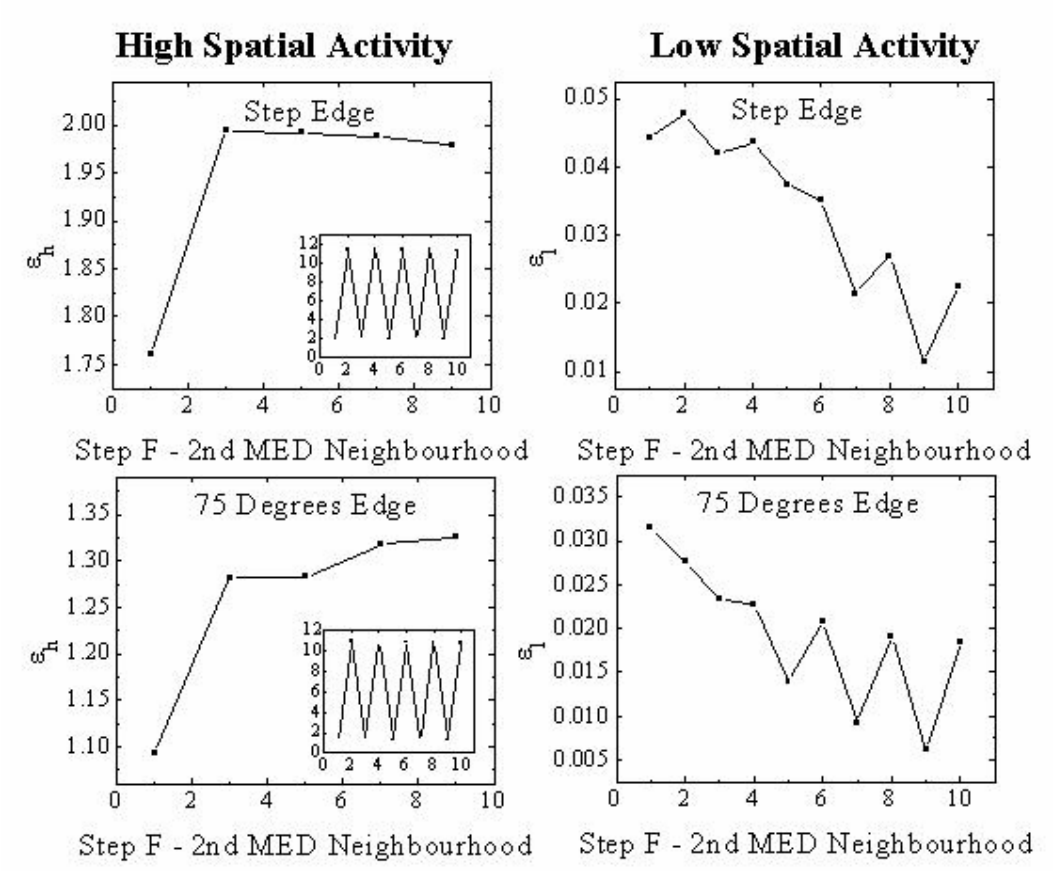

Figure 6.9 Relative performance of the algorithm when a median filter is passed over the image after recombination (step f from Figure 6.2).

6.4.1.1.2 Number of Iterations

Figure 6.10 shows that the number of iterations of the averaging filter (step A) does not affect the performance of the algorithm. This is because the purpose of the averaging filter is simply to deliberately blur the edges of the object so that the root signal found can be found by median filtering in step B, not to actually perform any noise smoothing. The average filter does not actually remove noise from the final image to any significant degree. Without this step some fine detail may be removed by the median filtering in step B.

When the number of iterations of the median filter (step B) is varied it can be seen that there is little change after 6 iterations, which indicates that the root signal has been found (Figure 6.11). The relative error achieves a minimum after 4 iterations in high spatial activity regions. With fewer than 4 iterations there is less filtering and when more than 4 iteration of the filter is applied there may be some distortion of the

signal around edges, indicating that 4 iterations is a trade-off between under filtering and edge distortion.

When the number of Wiener filter iterations are varied (step D) as shown in Figure 6.12 it can be seen that both high and low spatial activity performance declines with each iteration, although low spatial activity performance appears to show improvement after 16 iterations. The decline in performance is because repeated filtering tends to smooth out and spread the 'spikes' seen in the difference image (Figure 6.2) representing the difference at edges. Although little filtering is performed at sharp edges it does still occur and after each pass of the Wiener filter the edge spike blurs more so that on each pass more filtering occurs at edges than on the previous pass. This blurring of edges can extend into the low spatial activity region and increase ε_l.

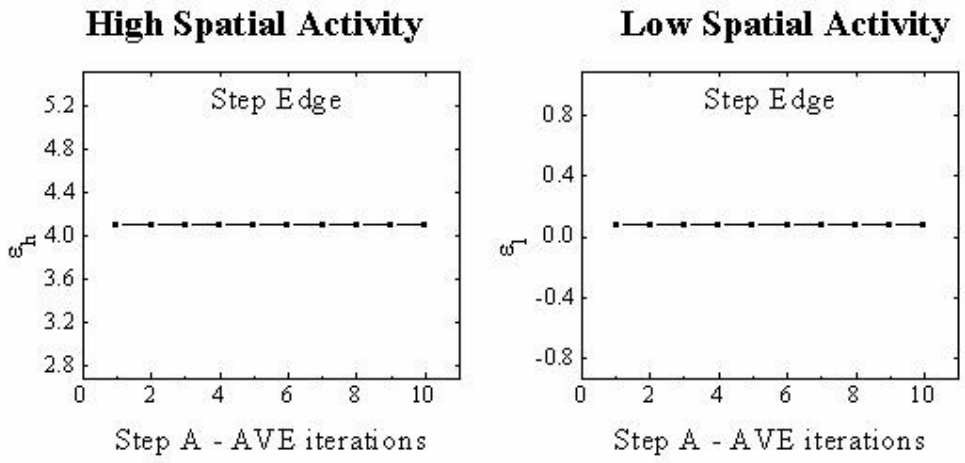

Figure 6.10 The performance of the algorithm on a step-edge object when the number of averaging filter iterations are varied.

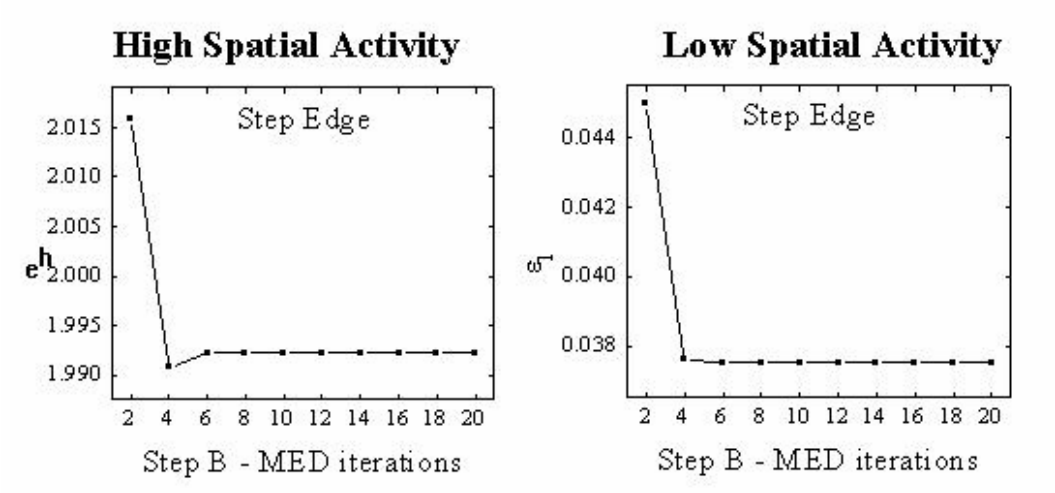

Figure 6.11 Relative error when the number of iterations of the median filter is varied.

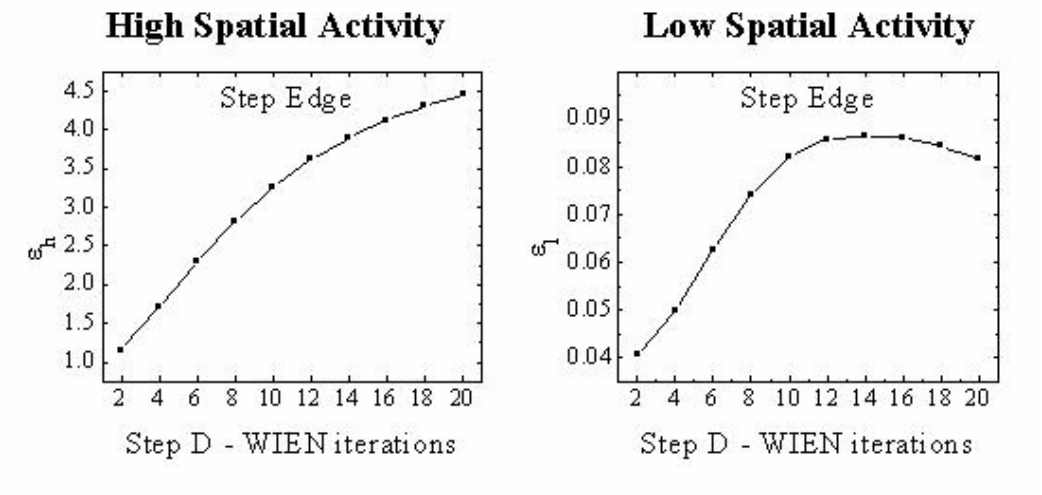

Figure 6.12 Relative error when the number of Wiener filter iterations are varied.

6.4.1.1.3 Parameters Chosen

For the remainder of this chapter performance of the image processing algorithm is based on the neighbourhood sizes and number of iterations of each step as shown in Table 6-1. Actual parameter values selected in different situations will vary depending upon the application for which the filter will be used, and performance will therefore also vary. The type of filter used in each step may also vary – again depending upon the application and outcome desired. Other variations can also include such things as finding the difference image by subtracting the low pass filtered image instead of the root signal etc.

Table 6-1 Filtering parameters used in the image processing algorithm

Step	Neighbourhood Size	Iterations
A. Averaging Filter	2	2
B. Median Filter	5	5
D. Wiener Filter	4	1
F. Median Filter	5	2

6.4.1.2 Comparison with Common Filters

In this section the performance of the image processing algorithm is compared with commonly available filters. The filters compared are named on the graphs and each filter has been compared using both a 3×3 and a 5×5 pixel neighbourhood. The algorithm used is designated within the graphs as “Algorithm”.

6.4.1.2.1 Effect of Signal to Noise Ratio

Figure 6.13 shows the relative error of the filters tested for varying SNRs. Shown are the results for step edge and disc radii of 1 and 25 pixels. By examining the relative error in a test image of 25 pixel radius and step edge the validity of the testing method can be established by comparing results to those achieved by previous authors [88, 89]. The performance of the median and averaging filters in high spatial activity is similar in characteristic to that reported by du Buf and Campbell in that the relative error increases with SNR, however the plateau reached by du Buf and Campbell at approximately SNR = 10 does not occur in these results. This may be due to the different manner in obtaining the mask image. Median and averaging filters in the low spatial activity region also display similar performance to du Buf and Campbell in that SNR has very little effect on the performance. Interestingly, the results reported in this chapter and those of du Buf and Campbell do not match those of Chin and Yeh, however Chin and Yeh do not specify their normalization procedure.

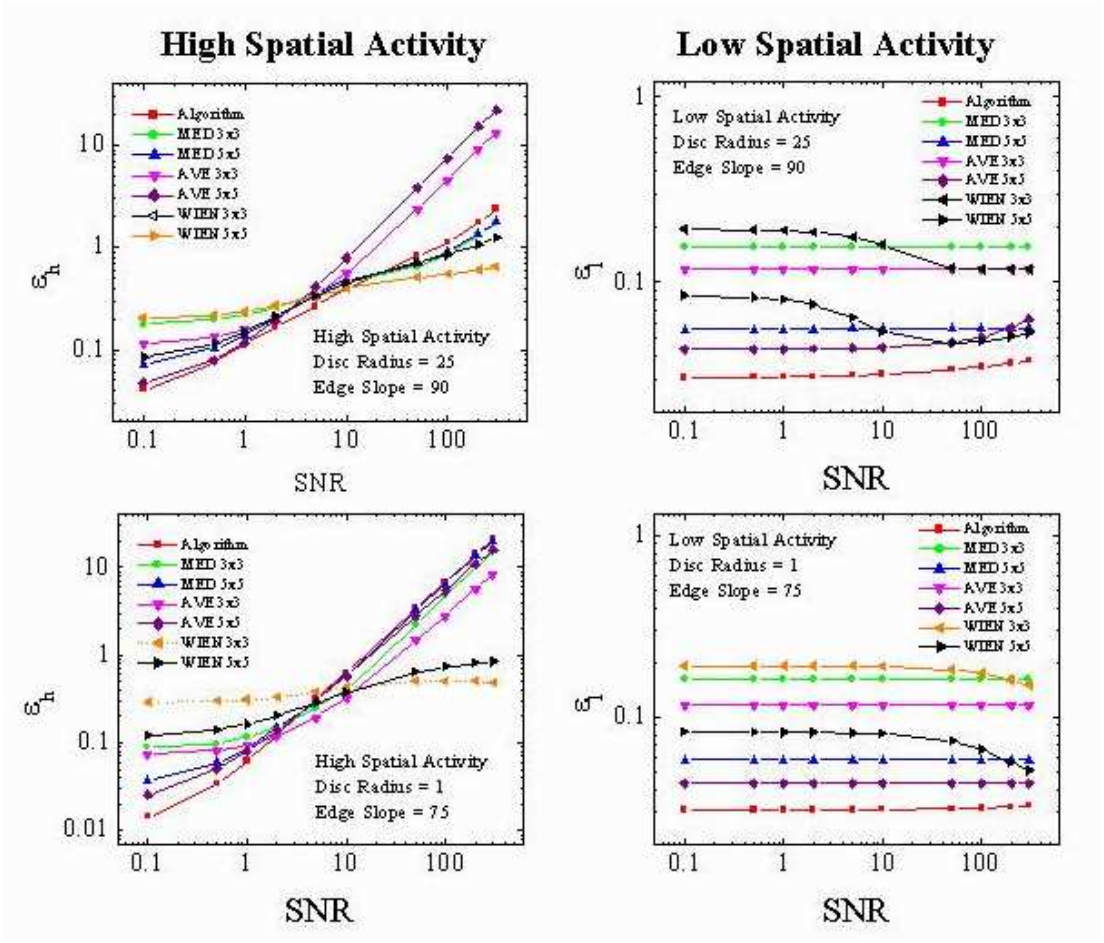

Figure 6.13 The relative error of commonly available filters and the algorithm designed in this chapter tested on a disc with step edge and varying SNR.

Figure 6.14 shows the same comparison of filters but for a disc with an edge gradient of 75° instead of a step edge. When testing on a large disc radius (25 pixels) and high spatial activity regions the algorithm of this chapter is the best performer up to an SNR of 100 in comparison to the results in Figure 6.13 where it performed better than other filters only up to SNR of 10. In both cases the best performer in regions above this was the 3 x 3 Wiener filter, however that particular filter was the worst performer in smaller SNRs. This is indicative of the fact that the Wiener filter is an adaptive filter and performs the least smoothing around areas of high spatial activity. From both figures it can be seen that the Wiener filter has the least effect on the noisy image and the better performance over other filters at high SNRs is due to the fact that the image is greatly degraded, rather than actual performance of the filter itself.

The performance of the algorithm designed in this chapter in high spatial activity regions appears to be best suited to edges rather than impulses (i.e. larger disc radii than smaller) in SNRs up to at least 10. The following sections will examine the effect of edge slope and disc radius in more detail.

When there is low spatial activity the relative error of the algorithm consistently outperforms the other filters, in fact the relative error decreases at SNRs greater than 10 and in some cases reduces to zero. This can be attributed to the fact that the algorithm is the result of several iterations of various types of lowpass filters and this result is therefore expected. Comparatively, the performance of the Wiener filter improves at high SNRs similarly to that in the high spatial activity case, and this may contribute to the increased performance of the algorithm.

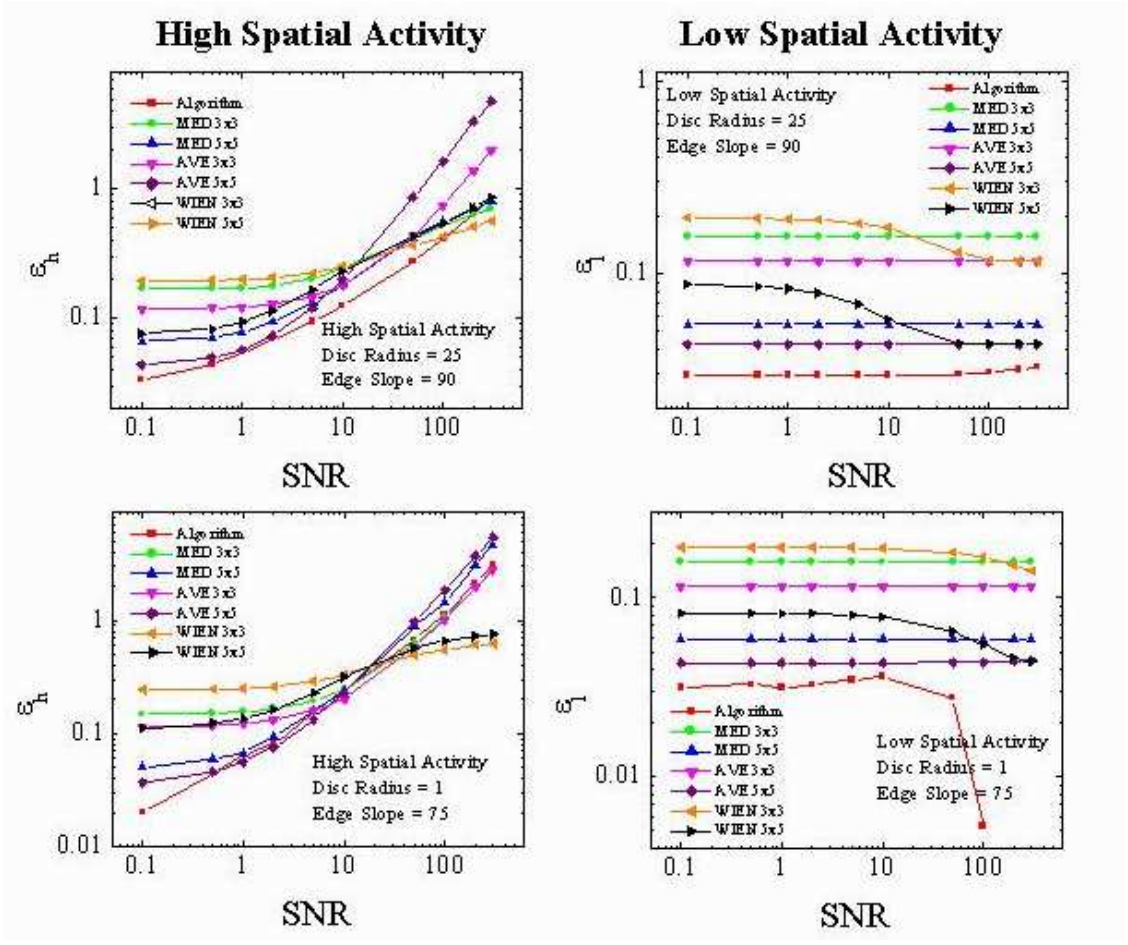

Figure 6.14 Relative error of various filters and the algorithm used in this chapter tested on a disc with 75 degrees ramp angle and varying SNR.

6.4.1.2.2 Effect of Edge Slope

Figure 6.15 shows that the performance of the average and median filters increases as the edge slope increases, similar to the results obtained by Chin and Yeh and du Buf and Campbell. The comparison is not exact as these results are shown for a SNR of 1, rather than 10 as investigated in the previous studies. This SNR was chosen as it is closer to that which would be expected in a CT gel dosimetry situation.

At the step edge and large edge gradients the algorithm outperforms the other filtering methods, however as the gradient decreases the performance becomes similar to the averaging filter in a 5×5 neighbourhood. The lowpass characteristic of the averaging filter tends to be well suited to the lower frequency components of a smaller edge gradient. Comparison of Figure 6.15 with Figure 6.13 and Figure 6.14 shows that the total change in performance of all filters with changing ramp angle tends to be small compared to changing SNR and implies that SNR has a much greater influence on the performance of all of the filters tested than the ramp angle. $\mathcal{E}_h$ measures the opposing effects of noise reduction and edge blurring simultaneously [89], and these competing effects may contribute to the lesser performance difference than observed with changing SNR.

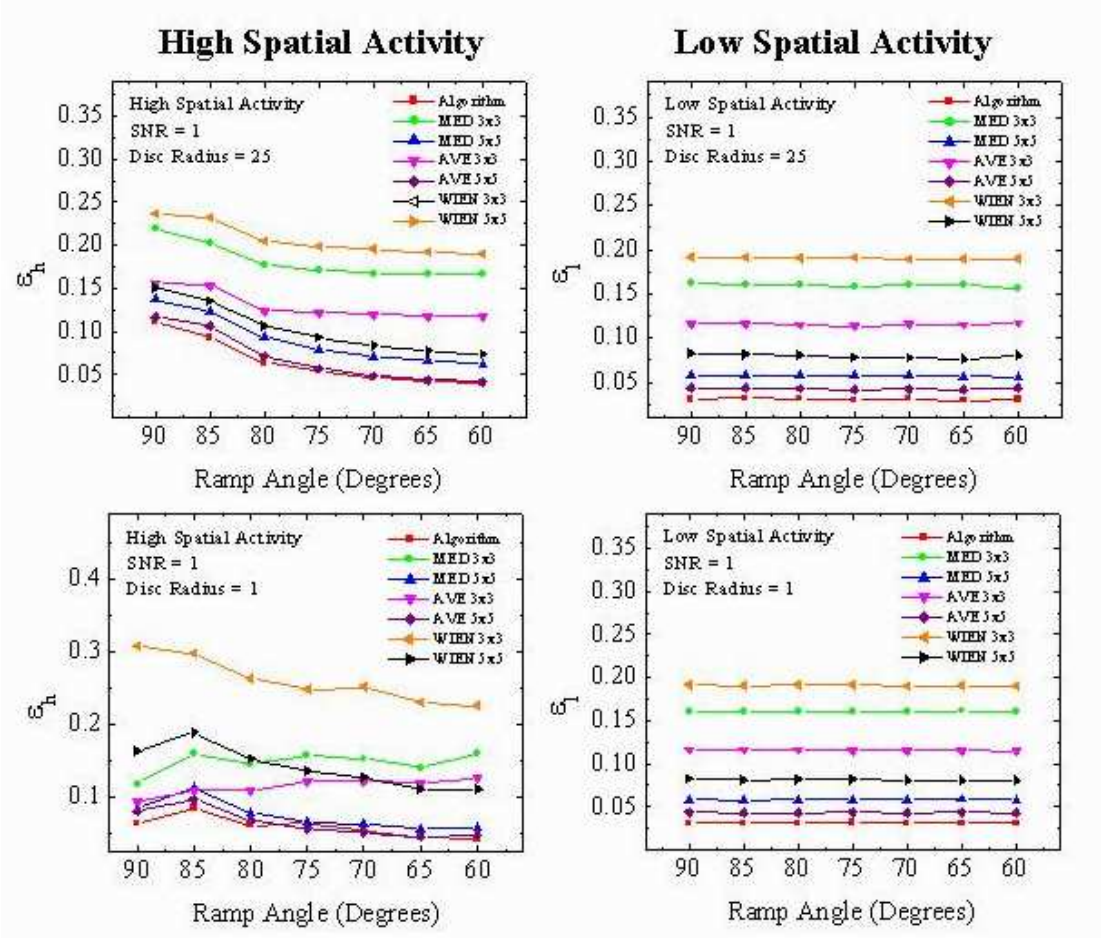

Figure 6.15 Relative error of various filters tested along with the algorithm of this chapter with various ramp angles. The disc radii are 25 pixels (top row) and 1 pixel (bottom row).

6.4.1.2.3 Effect of Disc Radius

Figure 6.16 shows that the performance of the developed image processing algorithm consistently outperforms the other filters for the disc radii tested. In regions of high spatial activity and SNR = 1 all filters except the adaptive Wiener filter appear to perform better at small disc radii than at large radii. At SNR = 0.1 the commonly available filters show the worst performance at a disc radius of 10 pixels but then stabilise (except WIEN5 which shows a steady increase in performance with increasing radius). When the spatial activity is low, disc radius appears to have very little effect on the performance of the filters tested. This is expected as these regions are away from the disc edge and hence the radius has little effect.

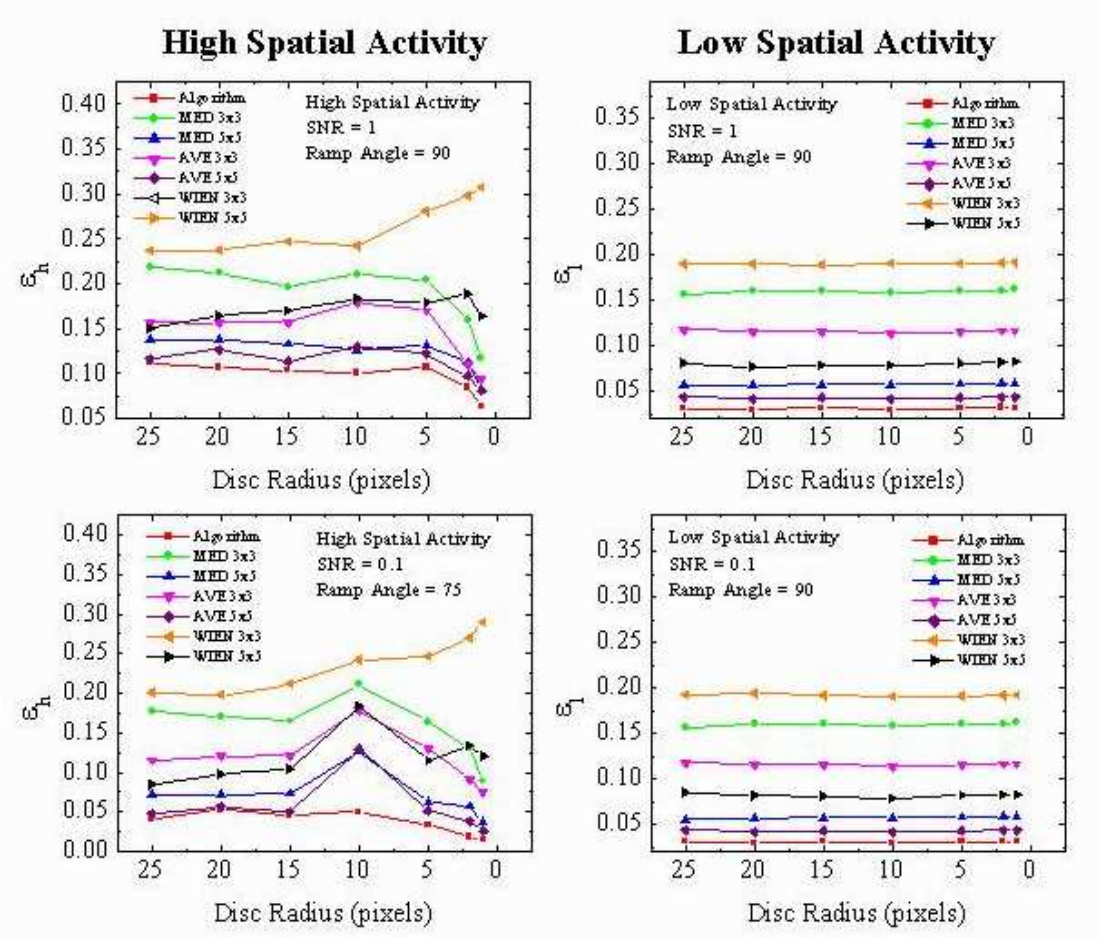

Figure 6.16 Relative error of various filters tested for varying disc radius with SNR of 1 (top row) and 0.1 (bottom row).

6.4.2 Simulation of an Irradiated Phantom

Figure 6.17 shows the noisy image of the simulated phantom windowed to a level suitable for viewing the noise and dose distribution. Figure 6.18 shows the noiseless simulated image overlaid with isodose contours for doses of 8 Gy, 7 Gy and 3 Gy. Figure 6.19 to Figure 6.22 show the result of processing Figure 6.17 with the method designed in this chapter and with some of the commonly available filters which were tested in this chapter.

The result of applying Equation 6.3 to the images is shown in Table 6-2. It is shown that on this image the best result is achieved by using the image processing algorithm. Because of the relatively low spatial frequencies within the image the most significant improvement is achieved by noise reduction and the competing factor of

edge blurring does not greatly affect the process. The repeated filtering within the algorithm ensured the noise reduction was greater than that of the common filters resulting in its better performance.

For the median, Wiener and averaging filters the best results are achieved by using larger neighbourhoods. This can again be attributed to the relatively low spatial activity of the image which indicates that blurring of sharp edges by the use of larger neighbourhoods did not make a significant contribution to the evaluation process. This is demonstrated by the fact that the same results are achieved for the Wiener filter and the averaging filter. Had there been sharp edges or extreme points within the simulated irradiation field the two filters would have produced different results.

The accuracy of the isodose lines in Figure 6.19 to Figure 6.22 in relation to those in Figure 6.18 is reflected in Table 6-2 as the lines are obtained directly from pixel values and ε is a measure of the improvement in the accuracy of pixel values after processing the noisy image.

Table 6-2 Quantitative results for the application of the image processing algorithm and commonly available filters to the simulated image.

Filter	ε
Image Processing Algorithm	0.0615
Median 5×5	0.0798
Median 3×3	0.1843
Wiener 5×5	0.0670
Wiener 3×3	0.1263
Average 5×5	0.0670
Average 3×3	0.1263

Qualitative effects of the filters can be assessed by examination of the isodose contours. Three contours have been highlighted in Figure 6.18. Contour 1 indicates a region of slowly changing pixel values and contours 2 & 3 indicate regions of

moderate spatial activity. Figure 6.19 to Figure 6.22 shows that contour 1 is better defined when the image is processed by the algorithm followed then by the averaging and adaptive filters, with the median filter being the worst performer. The contours resulting from filtering the image with the averaging filter and the adaptive filter are virtually identical owing to the fact that the adaptive filter tends towards becoming an averaging filter in low pass regions. In moderate spatial activity areas such as at contours 2 & 3 are more sharply defined when the image is processed with the algorithm, followed by the averaging and Wiener filters.

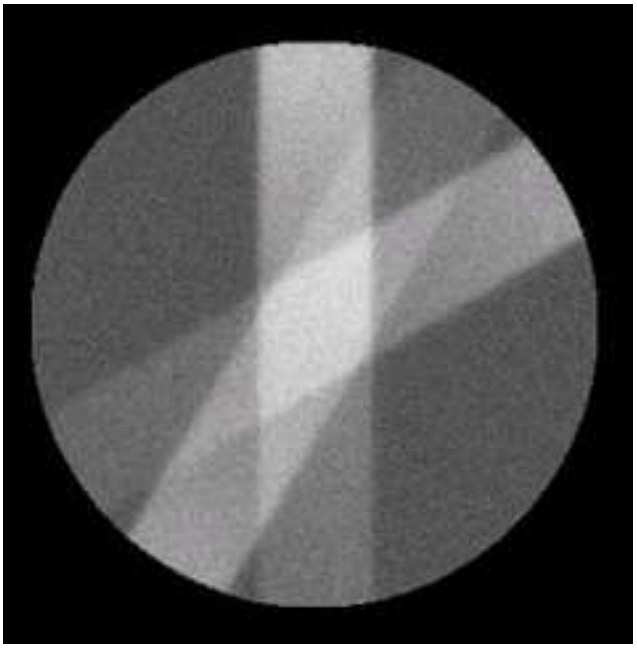

Figure 6.17 Simulation of an expected dose distribution in a 20 cm diameter phantom. See text for details.

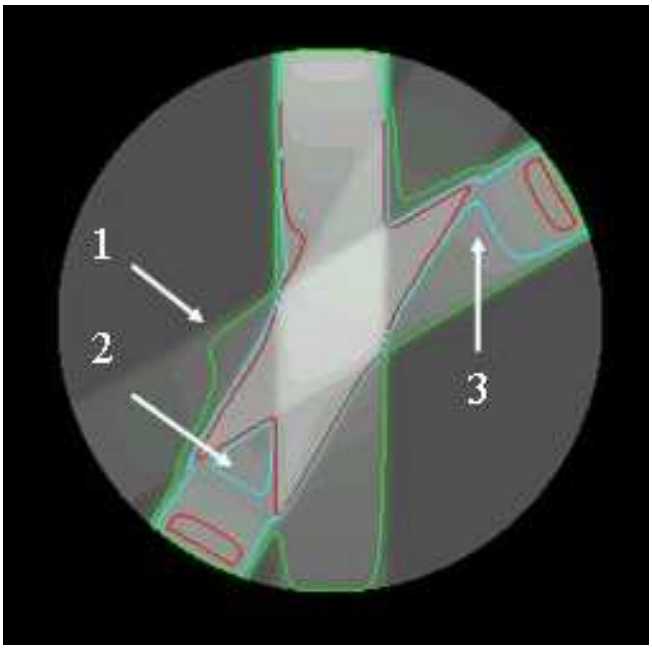

Figure 6.18 Pixel value contours for Figure 6.17. Isodose contours are shown for doses of 18 Gy, 17 Gy and 13 Gy. Regions 1, 2 & 3 simulate doses of 18 Gy, 17 Gy & 13 Gy respectively.

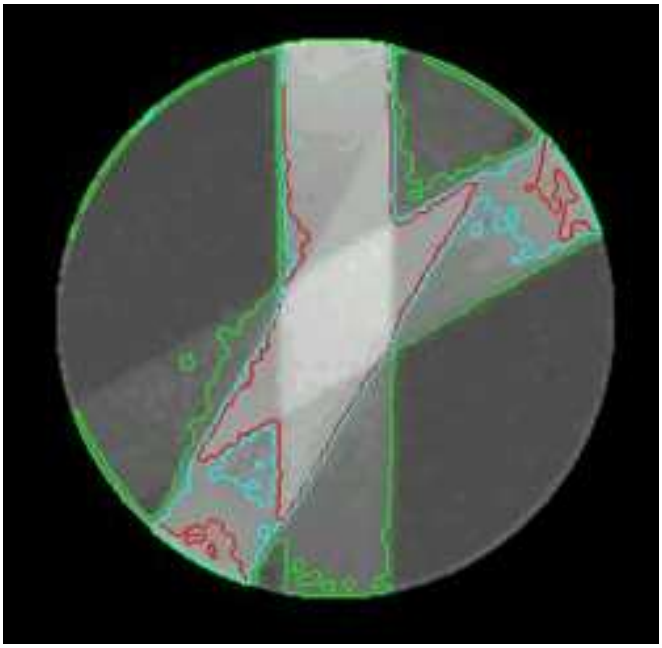

Figure 6.19 Result of filtering Figure 6.17 with the method designed in this chapter.

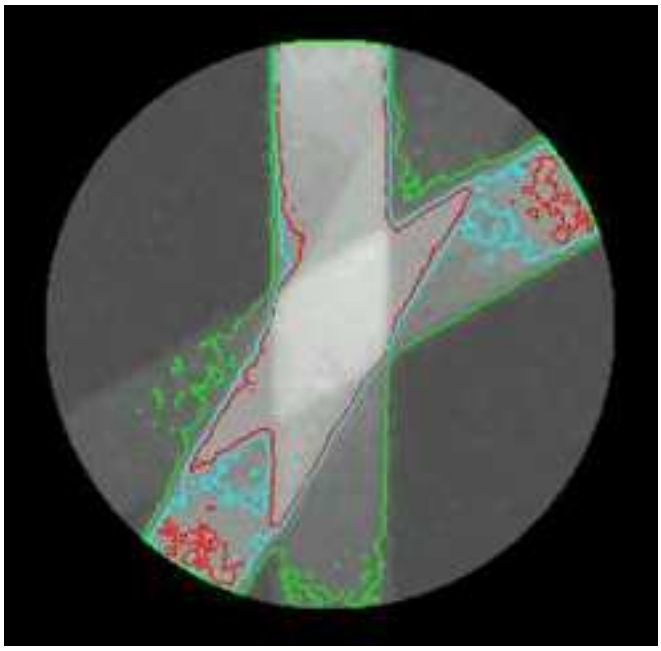

Figure 6.20 Results of filtering Figure 6.17 with a 5×5 median filter.

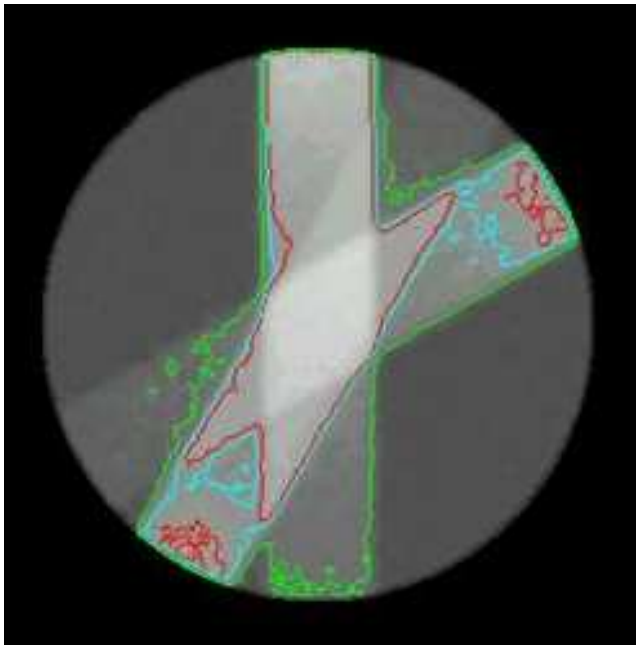

Figure 6.21 Result of filtering Figure 6.17 with a 5×5 adaptive Wiener filter.

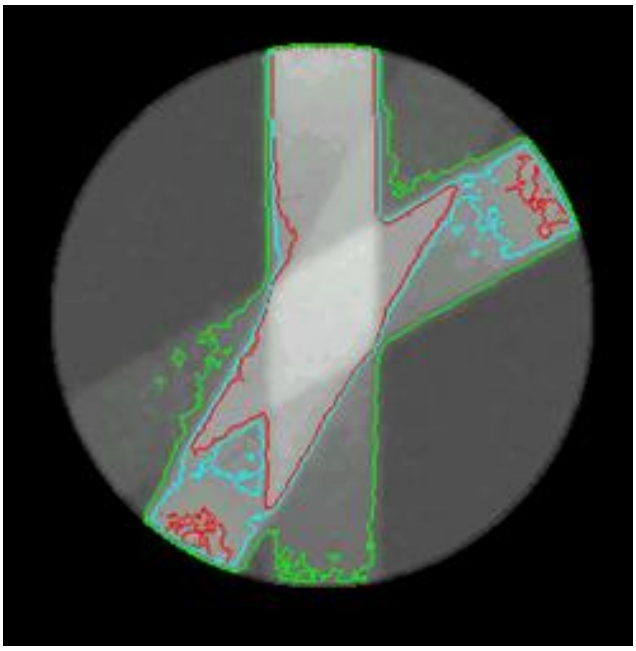

Figure 6.22 Result of filtering Figure 6.17 with a 5×5 averaging filter.

6.4.3 Image of an Irradiated Polymer Gel Dosimeter

Figure 6.23 to Figure 6.28 show the images of the phantom during the various stages of acquisition and processing as described throughout this document. All images are windowed to the CT number ranges 15-30 *H*. Figure 6.23 shows a single image of the phantom, unprocessed. The single image shows that the amplitude of the noise is large in comparison to the signal obtained by the irradiation. In fact, it is difficult even to see the irradiation, and any quantitative measurement would have a large associated uncertainty. The situation is greatly improved in Figure 6.24 where 150 images were averaged. The noise is greatly reduced and the change in the gel dosimeter after irradiation can easily be seen, but ring artifacts are present. The artifacts are subtracted through use of a second set of images of the water tank described in Chapter 2 and the results are seen in Figure 6.25. The grouping of pixels into 2×2 pairs was performed to produce a 256×256 image as described in Chapter 5 and is shown in Figure 6.26. Finally, the image processing algorithm is applied 3 times and the result is shown in Figure 6.27. CT number contour plots are overlaid on Figure 6.27 to produce Figure 6.28.

The improvement by use of the image processing algorithm can be seen by comparing Figure 6.26 and Figure 6.27; and the improvement by use of all of the

techniques described in this document can be seen by comparison of Figure 6.23 and Figure 6.27. Figure 6.28 shows CT number contours representing regions of relatively low dose (22 *H*), medium dose (25 *H*), high dose (28 *H*) and maximum dose (29 *H*). The 22 *H* contour shows that the low dose regions appear to be quite well defined, with greater accuracy around regions with steep dose gradient such as beam penumbra. Where dose gradients are less steep, such as when the contour crosses the beam, and on the exit side of the phantom, the contour appears to be less defined due to the presence of residual noise and the subsequent signal to noise ratio. This demonstrates the importance of selection of gel compositions which result in greater dose sensitivity – a greater sensitivity will increase the signal to noise ratio resulting in better defined CT number contours and subsequent isodose contours.

The 25 *H* CT number contour represents the dose gradient where two of the three beams are superposed. The contour appears to be well defined and comparison of the 'protruding' sections above and below the central high dose region demonstrates the effectiveness of the technique. The section above the high dose region shows that, as expected, the apex of the contour does not end in a 'sharp' point due to the superposition of beam penumbra. The contour towards the bottom of the image, which encloses a much smaller area than the top, shows that the technique was sufficient to detect the only difference between the two regions, i.e. the beams had traversed a greater gel depth resulting in their superposed intensities crossing the 25 *H* contour within the region rather than at its edge.

The results from this pilot study show that CT imaging has potential as a method for the extraction of absorbed dose information in polymer gel dosimeters. The image processing algorithm reduces noise whilst maintaining edge information and is best used in combination with the other techniques described throughout this document. Improved results can be achieved by the use of a scanner with greater kV, mAs per slice, or by averaging more images.

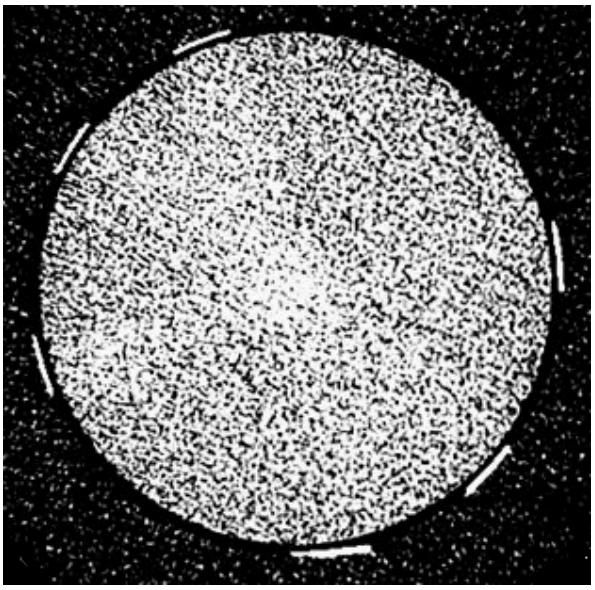

Figure 6.23 A single CT slice of the irradiated phantom.

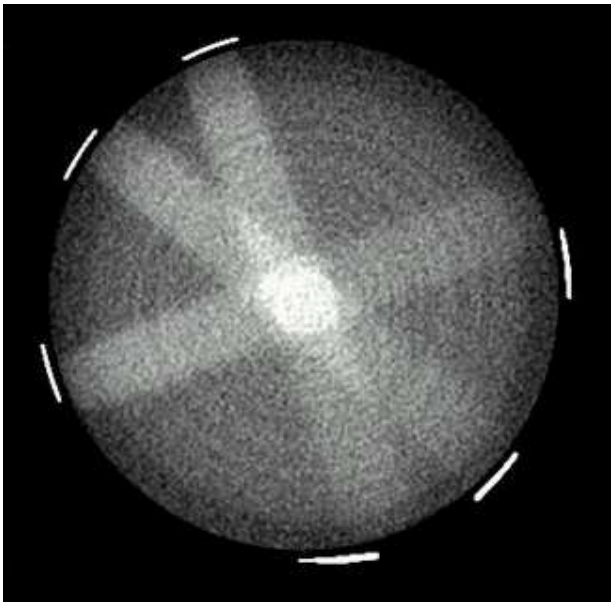

Figure 6.24 The average of 150 images of the phantom.

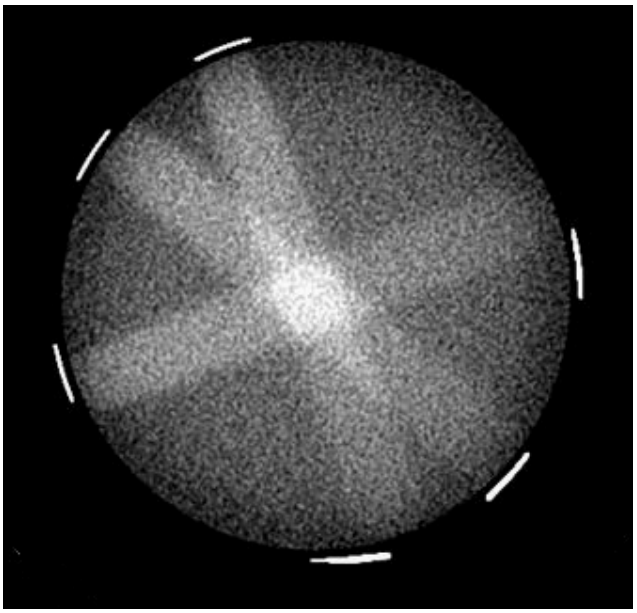

Figure 6.25 The difference between the averaged phantom image and the averaged water image.

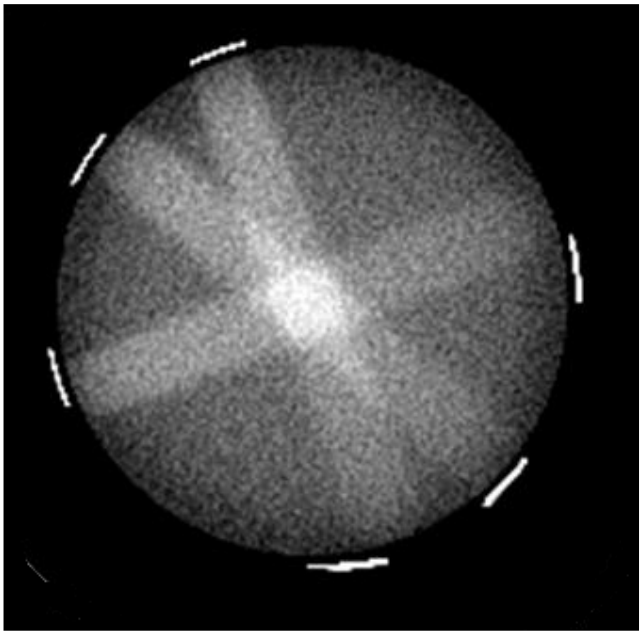

Figure 6.26 The subtracted averaged image of the phantom after 2×2 grouping of pixels as described in Chapter 5.

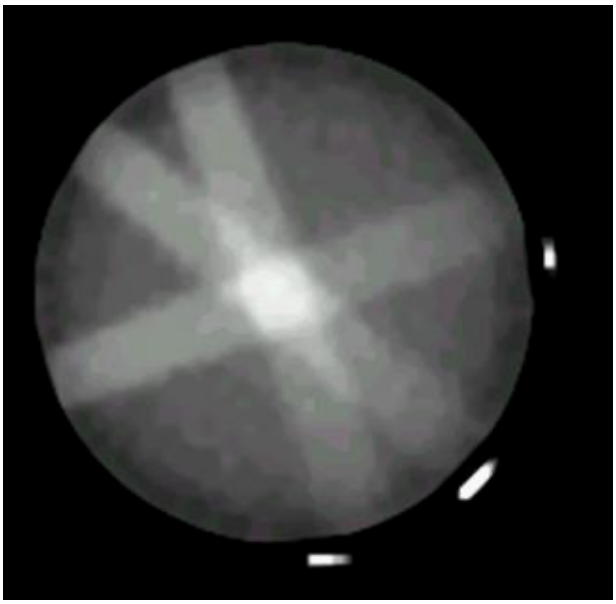

Figure 6.27 The final image after 3 passes of the filtering algorithm.

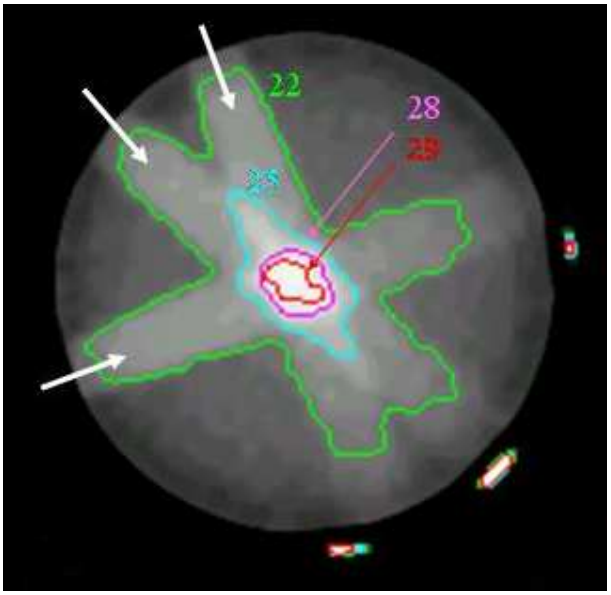

Figure 6.28 The final filtered image with CT number contours overlaid and labeled with their respective CT numbers. The direction of the beams is shown by the arrows.

6.5 Chapter Summary

In this chapter an image processing method was designed which employs a combination of common filters. The method was tested, along with the common filters by using a previously published technique. It was found that the designed image processing technique outperforms the common filters in most situations applicable to gel dosimetry in non conformal radiotherapy. The image processing

algorithm and the common filters were quantitatively tested on a simulated image of a non-conformal irradiation. A pilot study showed that CT imaging of polymer gel dosimeters has potential for success as a method for measuring dose distributions if the techniques described in this and other chapters are employed.

Chapter 7: Calibration Uncertainty

7.1 Introduction

After the noise in a CT gel dosimetry image has been sufficiently reduced the absorbed dose distribution can be examined. The absolute dose at any particular point can be determined by comparison of *H* with a calibration graph. The calibration consists of a function fitted to a graph of the dose response of gel dosimeters irradiated to known doses. Uncertainties will be introduced into the absorbed dose calculations through the uncertainty in *H* values measured in the image, uncertainty in the dose delivered to the calibration points in the calibration gel, and uncertainty in the goodness of fit of the calibration function to the data points.

In the literature to date there has been numerous contributions regarding calibration uncertainty in MRI of gel dosimeters. In this chapter these various methods of treatment are examined and a method is developed which is suitable for CT gel dosimetry and satisfies statistics theory and metrology recommendations of the International Organization of Standardization.

7.2 Background

When a series of measurements is acquired they are normally plotted on a graph with the independent variable on the abscissa (hereafter referred to as the ‘x axis’) and the dependent variable, or the measurement result on the ordinate (hereafter referred to as the ‘y axis’). In the case of gel dosimetry calibration data the delivered dose is normally plotted on the x axis, and the y axis indicates the measurement for each dose (e.g. *H* for CT measurements, R_2 for MRI etc). A calibration function is then fit to the data. There is

a degree of uncertainty in any physical measurement such as *H* and this will be shown as error bars in the y direction on the calibration data. The uncertainty in dose delivered to the gel dosimeter will be known from the uncertainty of the irradiation device.

In an image of an irradiated gel dosimeter the dose distribution will be determined by measuring *H* (in the case of CT). The values for *H* will be converted to values for dose by inversion of the calibration function. In this case the uncertainty in *H* will be known but the uncertainty in dose will not. It can be calculated by translating the uncertainty in *H* through the inverse of the calibration function (similar to the conversion of *H* to dose values). Figure 7.1 shows a simplified example of this process however it will be shown in the following sections that care must be taken to ensure that the uncertainty in the fit of the calibration function should also be reflected.

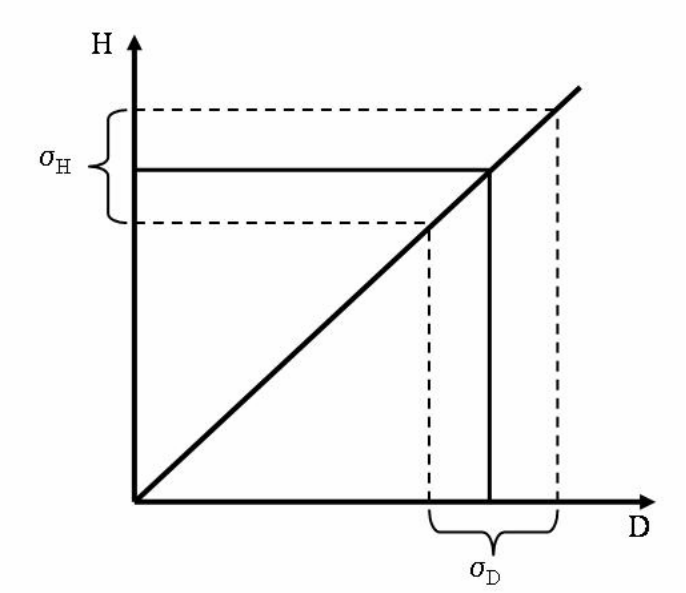

Figure 7.1 Demonstration of the propagation of an uncertainty in H to the uncertainty in D.

7.2.1 Calibration Uncertainty in MRI Gel Dosimetry

In MRI gel dosimetry many authors have simplified the calibration function by assuming a linearity of dose response up to a certain point [48, 93-96]. In this method the calibration function for a MRI image is described by [48]:

$$D = \alpha R_2 + R_{2,0} \qquad 7.1$$

where D is the absorbed dose, R_2 is the transverse relaxation rate, and the values of $R_{2,0}$ and α are determined by a linear least squares fit to the experimentally measured values for D and R_2. In this case the uncertainty in the delivered dose is given by [95]:

$$\sigma_D = \sqrt{R_2^2 \sigma_\alpha{}^2 + \alpha^2 \sigma_{R_2}{}^2 + \sigma_{D_o}{}^2 + 2R_2 \sigma_{\alpha D_0}} \qquad 7.2$$

An alternative treatment [96] of uncertainty in linear fits to the calibration function was the use of level-of-confidence intervals where Equation 7.1 has been inverted to $R_2 = R_{2,0} + \gamma D$:

$$\sigma_D = \sqrt{\frac{\sigma_{R_2}^2}{\alpha^2} + \frac{\sigma_{cal}^2}{\alpha^2 N_{ROI}} CCF^2} \qquad 7.3$$

where CCF is a calibration contribution factor, N_{ROI} is the number of pixels in a region of interest and σ_{cal} is the standard deviation of R_2 values in the region of interest.

Although an assumption of linearity in dose response allows simplification of calculations, a divergence from linearity after large doses has been repeatedly observed [47-51]. Accordingly, the requirement for linearity was removed and the uncertainty in dose using MRI became [77]:

$$u_c^2(D) = \frac{\partial D}{\partial T_2}^2 \sigma_{T2}{}^2 \qquad 7.4$$

where T_2 is the transverse relaxation time, and $u_c(D)$ is the combined expanded uncertainty [68]. A coverage factor, k_p was introduced, which is a multiplier to be used to determine uncertainty to a specific level of confidence, p [77]:

$$U_p(D) = k_p u_c(D) \qquad 7.5$$

where $U_p(D)$ is the expanded uncertainty to the required level of confidence.

The concept of dose resolution, D_{Δ}^{p} was introduced [77]. D_{Δ}^{p} is the minimal separation of doses at which their most probable values are different (i.e. the difference is greater than zero) to a level of confidence given by *p*:

$$D_{\Delta}^{p} = k_p \sqrt{2}\, u_c(D) = \sqrt{2}\, U(D) \qquad 7.6$$

where the $\sqrt{2}$ multiplier is due to an assumption that neighbouring dose distributions are approximately equal.

7.3 CT Calibration Uncertainty

For CT gel dosimetry it is proposed that the methods of treatment for calibration uncertainty as used for MRI gel dosimetry be combined and adapted to give an improved estimation of uncertainty which is consistent with the recommendations of the International Organization for Standardization [68]. The removal of linearity by Equation 7.4, combined with the uncertainty in the fitting parameters of the calibration function, as seen in Equation 7.2, will give a first order Taylor expansion of all parameters fit to the data.

It was shown in Chapter 3 that the dose response of a polymer gel dosimeter can be approximated by several functions. If a linear response in a limited range of doses is assumed the CT dose response can be approximated by:

$$H = H_0 + \alpha D \qquad 7.7$$

where α is a constant and H_0 is the CT number for the unirradiated gel. Equation 7.7 can be solved for *D* and the calibration uncertainty becomes the equivalent of equation 7.2, with R_2 terms exchanged for H. It was seen in Chapter 3 that over a wide range of doses a mono-exponential function can be fit to the data and the calibration function becomes:

$$H = v + u \exp\left(\frac{-D}{z}\right) \qquad 7.8$$

where *v*, *u* and *z* are fit parameters of the function. Solving equation 7.8 for *D* gives:

$$D = z\ln(u) - z\ln(H - v) \qquad 7.9$$

and a first order Taylor expansion of equation 7.9 gives $u_c(D)$, [68]:

$$u_C(D) = \sqrt{\sigma_H^2\left(\frac{\partial D}{\partial H}\right)^2 + \sigma_v^2\left(\frac{\partial D}{\partial v}\right)^2 + \sigma_u^2\left(\frac{\partial D}{\partial u}\right)^2 + \sigma_z^2\left(\frac{\partial D}{\partial z}\right)^2} \qquad 7.10$$

Alternatively, the data can be represented by a bi-exponential function:

$$H = v + u_1\exp\left(\frac{-D}{z}\right) + u_2\exp\left(\frac{D}{z}\right) \qquad 7.11$$

where u_1 and u_2 are the additional fit parameters for the function. Equation 7.11 does not have a unique solution when solved for *D*, therefore either the data should be plotted by reversing the axes prior to fitting the calibration function; or a linear or mono-exponential function should be used for calibration purposes. It will be shown in the following paragraphs that the incorrect function can be chosen with the result of an increased dose uncertainty. The examples in the remainder of this chapter are based on a mono-exponential fit of the calibration function to the data (Equations 7.8 – 7.10).

The use of a first order Taylor expansion considers the goodness of fit of the calibration function to the acquired data. The selection of an inappropriate calibration function will be evidenced by an increase in uncertainty. Figure 7.2 (insert) shows the data from Chapter 3 for PAG3. The solid line in the insert of Figure 7.2 is a calibration curve satisfactorily fitted to the data, and the dashed line represents an obviously poorly fitted calibration curve. The poorer fit results in larger values of σ_v, σ_u and σ_z in Equation 7.10 and larger values of *U(D)* are subsequently seen in Figure 7.2.

Had the goodness of fit not been considered, i.e. the adaptation of Equation 7.4 for CT, only the gradient of the calibration curve would have contributed to *U(D)*. The steeper gradient of the poor fit in low dose regions (the dashed line in Figure 7.2), compared to the gradient of the satisfactory fit (the solid line in Figure 7.2), would result

in a lesser *U(D)* for the poor fit, which is unacceptable. This can be visualised by re-examination of Figure 7.1 and observing the affect on σ_D after applying a steeper gradient to the function and maintaining constant σ_H. This demonstrates the inappropriateness of Equation 7.4 and shows that a first order Taylor expansion of the calibration function is essential for correct calculation of *U(D)*.

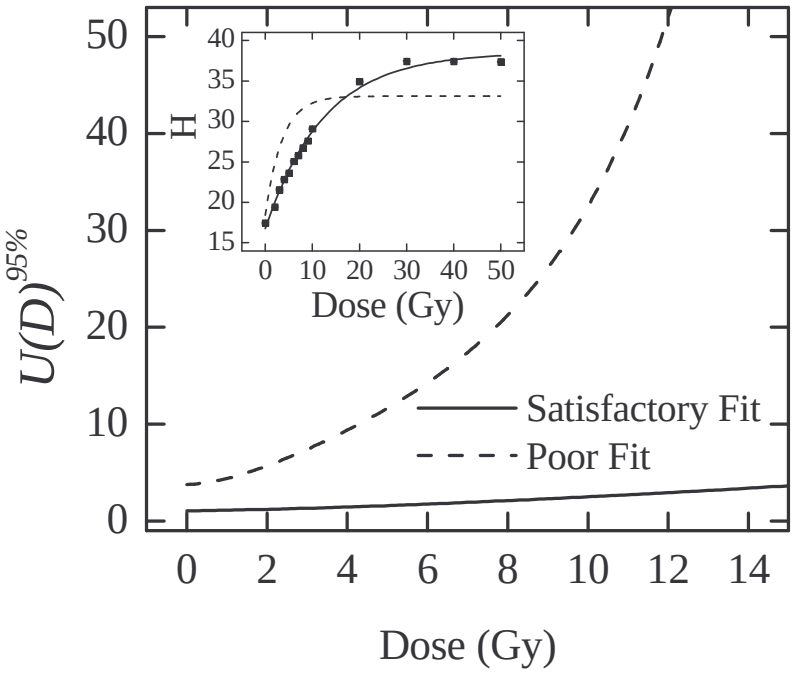

Figure 7.2 Comparison of the dose uncertainty between a satisfactorily fit calibration function and a poorly fit calibration function. The insert shows the original data with the two functions which have been fitted.

Figure 7.3 shows the same data as Figure 7.2, however the scatter of the data points has been artificially increased using a random number generator. *U(D)* is shown in the main figure for the cases of the original data, artificially increased scatter, and no scatter (data points artificially plotted exactly on the calibration function). This figure indicates that the scatter of data points is a significant factor contributing to the uncertainty of the calibration function. More scatter will increase $\sigma_{v,}$ σ_u and $\sigma_{z,}$ i.e. the goddess of fit is worse. In the case where there is no scatter of data points ($\sigma_v = \sigma_u = \sigma_z = 0$), Equation 7.10 will reduce to Equation 7.4 (with the R_2 terms exchanged for H). The

greatly reduced *U(D)* for this case is shown in Figure 7.3 and demonstrates that the use of Equation 7.4 will grossly underestimate *U(D)*, and that it is essential that the uncertainty in the fit parameters be included in uncertainty calculations.

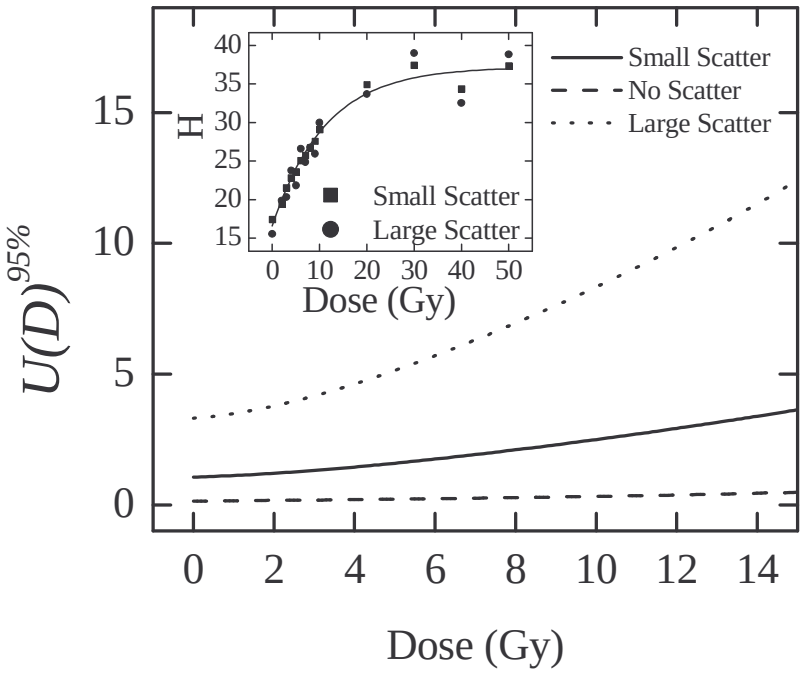

Figure 7.3 The effect of the scatter of data points on U(D). The scatter in the insert has been artificially increased using a random number generator. Also shown is the uncertainty when the calibration function fits the data perfectly.

A systematic error in the calibration function may result in an increased uncertainty. Figure 7.4 shows the results of the same data as the insert of Figure 7.2 with the addition of a systematic error in the 3-7 Gy range as seen in the insert. When Equation 7.10 is applied to the fit data it can be seen that there is a significant increase in the *U(D)*. Had the uncertainty in all the fit parameters not been considered there would have again been a dramatic underestimation of *U(D).*

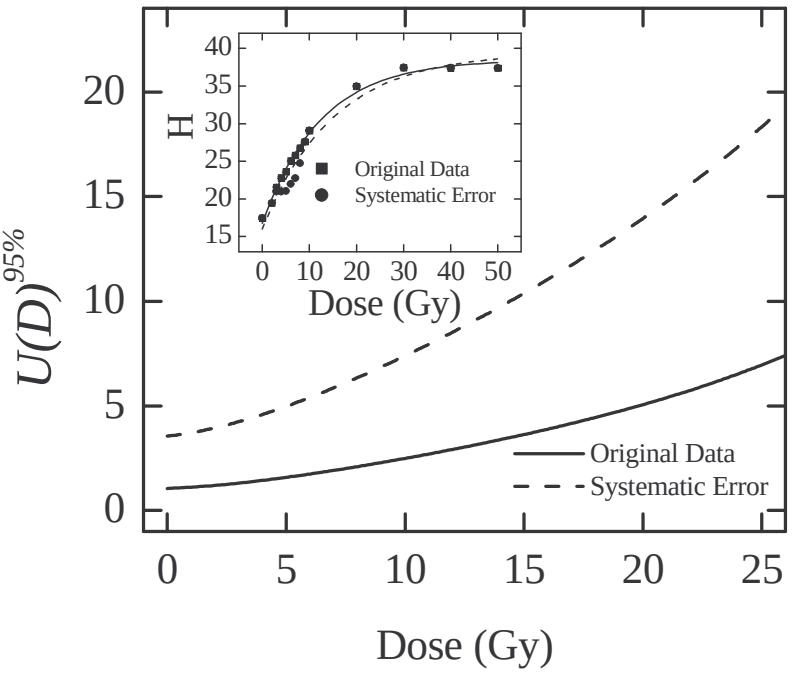

Figure 7.4 Calibration data with a systematic error introduced in the 3-7 Gy range (insert) results in an increased value of U(D).

Figure 7.5 is a plot of *U(D)* of the satisfactorily fitted calibration function to the data in the insert of Figure 7.2, but the uncertainty in individual data points, σ_H has been artificially varied. It can be seen that the use of a first order Taylor expansion indicates that even when the data points have no uncertainty (indicating a noiseless image) there is still a contribution to *U(D)* by the calibration function itself. In this case the first term in Equation 7.10 is reduced to zero, but there is still a contribution by the uncertainties in each of the fit parameters, as opposed to the current MRI gel dosimetry method (Equation 7.4) where *U(D)* would have yielded a result of no uncertainty. This result demonstrates that it is essential that all components of the calibration be considered when calculating uncertainty in gel dosimetry and that the greatest contribution to uncertainty is due to the fit of the calibration function and not image noise.

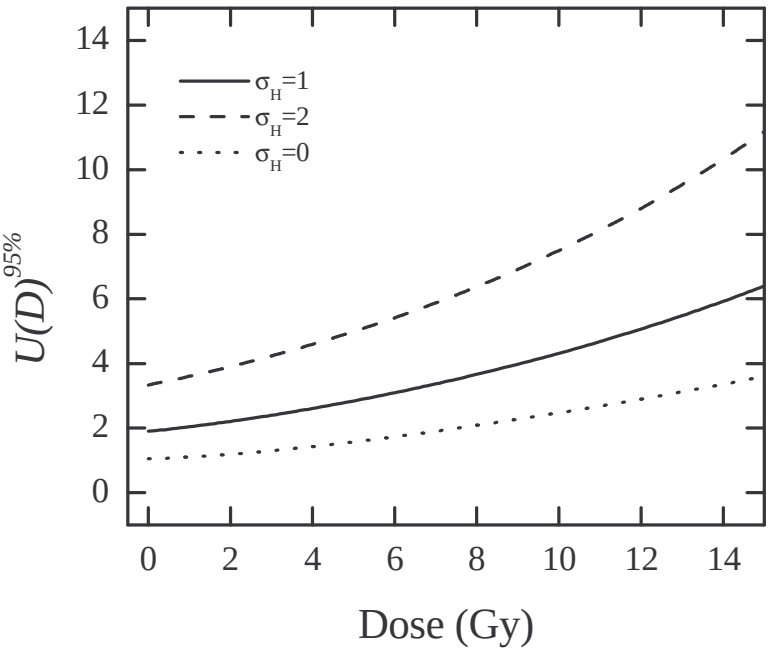

Figure 7.5 U(D) with a varying uncertainty in each data point.

7.4 CT Dose Resolution

Similar to MRI, it is proposed that dose resolution for CT gel dosimetry calibrations be defined by Equation 7.6, but with the value for $u_c(D)$ calculated by first order Taylor expansion of the calibration function as discussed in Section 7.3. Accordingly, Figure 7.6 shows $D_{\Delta}^{95\%}$ for selected gel dosimeters from Chapter 3 using a mono-exponential fit to the data. The particular gel dosimeters were chosen to represent a range of dose resolution.

It can be seen from Figure 7.6 that the smallest dose resolution of the gels tested is achieved by using HEA1. Although other gels such as PAG9 (5% monomer concentration) have greater sensitivity, the relatively little scatter of the HEA1 data points ensured that the calibration uncertainty remains small in comparison to the other gels. From the results of Chapter 3 the greatest sensitivity of all of the gel dosimeters was seen in the agarose based PAA2, however Figure 7.6 shows that this gel performs relatively

poorly in comparison to the other gels when calculating dose resolution. This is again due to the greater scatter of the data points within the calibration graph which results in greater values for σ_u, σ_v, and σ_z.

The results indicate that the dose resolution is dependant upon not only sensitivity and image noise, but also the accuracy of the measurement. The result is that the dose resolution can vary between gel dosimeters of the same chemical composition. Additionally, it is not inconceivable that the dose resolution for a particular gel dosimeter will vary between measurements. Therefore, it is essential that each gel dosimeter be calibrated if absolute dose is to be determined in an irradiation and good experimental practice must be employed to ensure accuracy and repeatability of measurements.

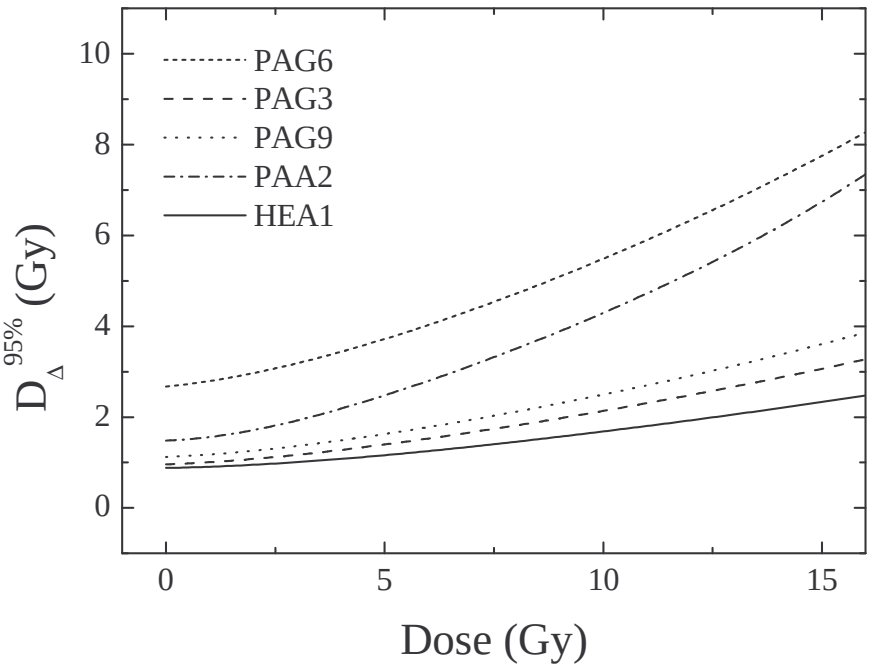

Figure 7.6 Dose resolution with 95% confidence levels for various gel dosimeters from Chapter 3.

7.5 Chapter Summary

Methods for treatment of calibration uncertainty in MRI gel dosimetry have been reviewed. A method has been proposed for CT gel dosimetry which considers the uncertainty in the fit of the function to the data as well as the uncertainty in the individual data points.

Further examination of the results of the gels examined in Chapter 3 demonstrated that the dose resolution of a particular gel dosimeter depends on a number of factors including the scatter of data points, gel sensitivity and image noise. If all parameters of the calibration are not considered the uncertainty will be underestimated. Good experimental method is necessary to improve accuracy and precision of measurements and a calibration is required for each gel dosimeter if absolute dose is required.

The work of this chapter has been published in the conference proceedings for 'DOSGEL 2001 – 2nd International Conference on Radiotherapy Gel Dosimetry' [67].

Chapter 8: Conclusion

8.1 Summary

It has been the objective of this thesis to investigate and develop CT imaging and noise reduction methods for specific use in gel dosimetry. The benefits of using CT as an imaging modality include speed, lack of temperature dependence and ease of use.

Although the main purpose of the project was to develop methods for the improvement of signal to noise ratio in CT gel dosimetry images, there were other issues which first needed to be resolved. The first step of any new process of measurement is to investigate whether there is actually a signal to be measured. However, prior to this some basic procedures required development to ensure that suitable measurements could be made. Chapter 2 examined some of the issues associated with making quantitative measurements using CT, namely the artifacts inherent in the modality. An artifact subtraction technique which was employed by a previous study was modified in such a way that individual calibration vials could be used for CT gel dosimetry. This modified subtraction technique uses a circular water tank which can be imaged with a phantom or calibration vials, or with water only. Provided the tank is not moved relative to the scanner the images of water can be subtracted from the images of the phantom and most of the artifacts will be removed.

Solving the issue of artifact reduction paved the way for a basic study on the CT dose response of gel dosimeters. It was shown in Chapter 3 that varying the chemical composition will affect the CT dose sensitivity, with an overall range of 0.26 ± 0.02 H/Gy to 1.43 ± 0.05 H/Gy for the compositions studied. The variation in sensitivity is dependant upon which ingredients are varied, for example, changing the gelatin concentration makes little difference whilst changing the monomer concentration will

produce significant changes. It was also shown that different chemicals can be used and a CT signal will result.

The characterisation of the CT dose response of gels requires an investigation into the cause of the signal. In Chapter 4 post-irradiation density was measured using Archimedes' Principle and linear attenuation coefficient was measured using a solid state detector and gamma spectroscope. It was shown that the cause of the CT signal is a post-irradiation increase in density. This increase in density must be related to a decrease in volume as there is no mass added to the gel dosimeter during photon irradiations. Therefore, there is a degradation of spatial resolution accompanying the absorbed radiation dose; however the increase in density for a fully polymerised gel was of the order of only 1 %.

Having characterised the CT signal, the direction of the project could then be shifted back to CT imaging techniques. Stochastic and structural noise was investigated in Chapter 5 both with computer simulations and experimentally. It was confirmed that the stochastic component of the noise in a CT image can be reduced by averaging a number of images. The improvements in noise reduction by this method are limited by the fact that there is structured noise due to sampling rates, i.e. the number of ray-sums in a projection and the number of projections in a scan. Computer simulations predicted that the structured noise can be greatly reduced by acquiring an image with as many ray-sums and projections as possible (reconstructing with a large image size) and grouping the pixels into 2×2 or 4×4 blocks. The simulation predicted increases in signal to noise ratio of up to two orders of magnitude. Experimental work was undertaken which produced some evidence to confirm an increase in signal to noise ratio but there the success of the technique shows a radial dependency.

As a final method to reduce the noise and hence improve signal to noise ratio in a CT gel dosimetry image, an image processing algorithm was designed and tested in Chapter 6. The algorithm consists of filtering the image in a number of steps using commonly available image filters. A quantitative test detailed in previous literature was slightly modified to test the algorithm and compare it with some common image

processing techniques. It was shown that, in most cases, the algorithm outperforms the methods currently available. The image processing algorithm and filters were then quantitatively tested on a simulation of a CT image of an irradiated gel dosimetry phantom and the algorithm was shown to provide the best performance for that test. Finally a pilot study was performed by producing a gel dosimeter, irradiating it with three intersecting photon beams and imaging it with a CT scanner using techniques developed throughout this project.

The final stage of development of CT gel dosimetry was to establish the correct method of calculation of calibration uncertainty. In Chapter 7 a brief review of the methods which have been used for calculations in MRI gel dosimetry calibration uncertainty was followed by the evaluation of experimental methods which are recommended by the International Organisation for Standardisation (ISO). Previously published methods for uncertainty calculations in MRI gel dosimetry have been in accordance with the recommendations when the dose response is assumed to be linear; however when higher doses are delivered to a gel dosimeter the response is not linear and uncertainty calculations published for MRI gel dosimetry assume a perfect fit of the calibration function. This results in significant underestimation of uncertainty and is not in accordance with the ISO recommendations. The correct method for treatment of experimental calibration uncertainty beyond the linear dose response range was demonstrated in Chapter 7. It is important that correct methods for this aspect of CT gel dosimetry be established early in the development of the modality, otherwise errors may be propagated throughout the literature as has been seen in MRI gel dosimetry by repetition of the incorrect method in recent papers.

In Chapter 7 the CT dose resolution was calculated for the gels examined in Chapter 3. It was found that the smallest dose resolution was not achieved by the gel composition with the greatest sensitivity. Although the sensitivity of PAG9 was 1.43 ± 0.05 H/Gy compared to 1.0 ± 0.2 H/Gy for HEA1, the minimum dose resolutions were 1.12 Gy and 0.88 Gy respectively. This indicates that the precision of a gel dosimeter is dependent upon factors besides dose sensitivity.

8.2 Discussion

The advantages of CT as an imaging modality for polymer gel dosimeters include speed, relative insensitivity to temperature, and accessibility (most clinics already have access to scanners for planning). Prior to this project disadvantages of CT included the existence of image artifacts and poor signal to noise ratio. The work of this project endeavoured to address these disadvantages.

The reduction of artifacts was the first step towards successful use of CT in gel dosimetry. Although the previously existing method of artifact removal worked well, the water tank designed in this project is an improvement because it does not suffer the disadvantages of requiring a second unirradiated phantom and its accurate realignment. Another advantage is that calibration vials can be imaged in the water tank. Disadvantages are that glass walled phantoms still can not be used in the water tank due to the beam hardening within the phantom walls, and the necessary additional diameter of the tank over that of the phantom reduces the number of photons arriving at detectors, thus either increasing statistical noise or requiring an increased number of scans to be averaged to reduce the statistical noise to a practical level. For a phantom irradiation the ideal solution would be to produce a water tank with a diameter specific to requirements. A suggested future research project might involve the investigation of a variable diameter cylinder which could be achieved by either varying the outer diameter of the water tank, placing air-filled rings or tubes inside the diameter of the tank, or by changing the shape of the tank to a cone.

The CT signal can be increased or decreased by changing the monomer concentration. The useful CT number range of 10-15 *H* indicates that most improvements in signal to noise ratio will be either through the reduction of noise or future research into the development new gel dosimeter compositions with a greater sensitivity over a useful range of CT numbers. A promising result for the future of gel dosimetry is that normoxic gels will produce a CT signal. Two of the factors impeding the routine clinical use of gel dosimeters are the difficulty in manufacture and difficulty in access to MRI scanners. A normoxic gel can be easily produced ‘on the bench top’ and CT scanners are available to

most clinics. Any future research resulting in normoxic gel dosimeter compositions with increased CT sensitivity will be welcomed in the gel dosimetry 'community' as a significant step towards widespread acceptance of gel dosimetry as a clinical tool.

A post-irradiation increase in density of gel dosimeters of the order of 1% implies that spatial uncertainty will be introduced to any irradiated gel dosimeter and occurs regardless of imaging modality. Although the change is relatively small, accurate modelling is required in the future to examine the process both microscopically and macroscopically. A microscopic examination of the changes which cause the density increase might enable researchers to design gel compositions to maximise the increase in density. However, an increased density change will lead to increased spatial uncertainty. Macroscopic modelling of particular dose distributions in phantoms will show whether spatial uncertainty remains within acceptable limits, and might provide a guide to spatially manipulating the final image so that the effects of the volume decrease may be reversed to some degree.

Noise can be reduced in a CT image to a fraction of its original amplitude. This work has demonstrated that averaging a sufficient number of images together will reduce stochastic noise to a level small in comparison to that of structured noise in the image. It has also been shown that the structured noise can be further reduced by averaging groups of pixels together. The method theoretically improves the signal to noise ratio by orders of magnitude. Experimental results support the theory; however there appears to be a radial dependency of the phenomenon. There is scope for future experimentation by extending image averaging into the structured noise region when more powerful scanners are available than those used in this project.

Although the image processing algorithm developed here is computationally expensive, it shows promise as a signal processing technique. Once the parameters within the algorithm were chosen they were not varied and it would be unwise to suggest that these parameters are optimal for every situation. A suggestion for future work is to change the component filters used within the algorithm. Alternatively, because the algorithm is based on separately manipulating low and high frequency components of the

image, there may be some advantages in performing operations in the frequency domain. The main idea behind the algorithm is that the image can be split into components (in this case low and high frequency), and the components can be individually filtered with techniques which are optimal for the individual components, and then the image is reconstructed. It is suspected that a full investigation of the properties of the algorithm and all its possible variations would be a significant piece of work in itself.

The pilot study in Chapter 6 showed that the techniques developed in this project can be used to obtain an image of a radiation dose distribution. The study was in no way intended to produce an anthropomorphic phantom of clinical standard, simply to show the progress to date resulting from this project. It was therefore pleasing to see that CT number contours in Figure 6.28 were relatively well defined; in fact, had a more powerful scanner been available at the time the results would have been even better (the noise in the image was still in the stochastic noise region). This indicates that clinical viability of CT gel dosimetry is perhaps closer than expected.

References

1. Hilts, M., et al., *Polymer Gel Dosimetry Using X-ray Computed Tomography: A Feasibility Study.* Phys. Med. Biol., 2000. **45**: p. 2559-2571.
2. Ambrose, J. and G.N. Hounsfield, *Computerized transverse axial tomography.* British Journal of Radiology, 1973. **46**: p. 148.
3. Hounsfield, G.N., *Computerized transverse axial scanning (tomography): Part 1. Description of system.* British Journal of Radiology, 1973. **46**: p. 1016-1022.
4. Michael, G., *X-ray computed tomography.* Phys. Educ., 2001. **36**: p. 442-451.
5. Newton, T.H. and D.G. Potts, eds. *Radiology of the skull and brain.* Vol. 5. 1981, The C.V. Mosby Company: St Louis, USA.
6. Day, M.J. and G. Stein, *Chemical Effects of Ionizing Radiation in Some Gels.* Nature, 1950. **166**: p. 1146-1147.
7. Mesrobian, R.B., et al., *Gamma-Ray Polymerization of Acrylamide in the Solid State.* J. Chem. Phys., 1954. **22**: p. 565-566.
8. Andrews, H.L., R.E. Murphy, and E.J. LeBrun, *Gel Dosimeter for Depth Dose Measurements.* Rev. Sci. Inst., 1957. **28**: p. 329-332.
9. Gore, J.C., Y.S. Kang, and R.J. Schulz, *Measurement of Radiation Dose Distributions by Nuclear Magnetic Resonance (NMR) Imaging.* Phys. Med. Biol., 1984. **29**: p. 1189-1197.
10. Olsson, L.E., et al., *Diffusion of ferric ions in agarose dosimeter gels.* Phys. Med. Biol., 1992. **37**(12): p. 2243-2252.
11. Maryanski, M.J., et al., *NMR Relaxation Enhancement in Gels Polymerized and Cross-linked by Ionizing Radiation: A New Approach to 3D Dosimetry by MRI.* Magn. Reson. Imaging, 1993. **11**: p. 253-258.
12. Maryanski, M.J., et al., *Magnetic Resonance Imaging of Radiation Dose Distributions Using a Polymer-Gel Dosimeter.* Phys. Med. Biol., 1994. **39**: p. 1437-1455.
13. Maryanski, M.J., J.C. Gore, and R.J. Schulz, *Three-Dimensional Detection, Dosimetry and Imaging of an Energy Field by Formation of a Polymer in a Gel.* 1994, Yale University: USA.
14. Maryanski, M.J., Y.Z. Zastavker, and J.C. Gore, *Radiation Dose Distributions in Three Dimensions from Tomographic Optical Density Scanning of Polymer Gels: II. Optical Properties of the BANG Polymer Gel.* Phys. Med. Biol., 1996: p. 2705-2717.
15. Rae, W.I., et al., *Chelator effect on ion diffusion in ferrous-sulfate-doped gelatin gel dosimeters as analyzed by MRI.* Med. Phys., 1996. **23**: p. 15-23.

16. Gore, J.C., et al., *Radiation Dose Distributions in Three Dimensions from Tomographic Optical Density Scanning of Polymer Gels: I. Development of an Optical Scanner.* Phys. Med. Biol., 1996. **41**: p. 2695-2704.

17. Baldock, C., et al., *Fourier Transform Raman Spectroscopy of Polyacrylamide Gels (PAGs) for Radiation Dosimetry.* Phys. Med. Biol., 1998. **43**: p. 3617-3627.

18. Mather, M.L., A.K. Whittaker, and C. Baldock, *Ultrasound evaluation of polymer gel dosimeters.* Phys. Med. Biol., 2002. **47**: p. 1449-1458.

19. Fong, P.M., et al., *Polymer gels for magnetic resonance imaging of radiation dose distributions at normal room atmosphere.* Phys. Med. Biol., 2001. **46**: p. 3105-3113.

20. DOSGEL'99. *Proc. 1st Int. workshop on Radiation Therapy Gel Dosimetry*. 1999. Lexington, USA: Canadian Orgainization of Medical Physicists.

21. Lepage, M., et al., *Dose resolution optimization of polymer gel dosimeters using different monomers.* Phys. Med. Biol., 2001. **46**: p. 2665-2680.

22. Pappas, E., et al., *A new polymer gel for magnetic resonance imaging (MRI) radiation dosimetry.* Phys. Med. Biol., 1999. **44**: p. 2677-2684.

23. Vollmert, B., *Polymer Chemistry*. 1973, New York: Springer-Verlag.

24. Baldock, C., et al., *Experimental Procedure for the Manufacture and Calibration of Polyacrylamide Gel (PAG) for Magnetic Resonance Imaging (MRI) Radiation Dosimetry.* Phys. Med. Biol, 1998. **43**: p. 695-702.

25. Hepworth, S., M.O. Leach, and S.J. Doran, *Dynamics of Polymerization in Polyacrylamide Gel (PAG) Dosimeters: (II) Modelling Oxygen Diffusion.* Phys. Med. Biol., 1999. **44**: p. 1875-1884.

26. McJury, M., et al. *Ageing and Long-term Stability in Polyacrylamide Gel (PAG) Dosimeters.* in *DosGel'99 - Proc. 1st International Workshop on Radiation Therapy Gel Dosimetry*. 1999. Lexington, Kentucky, USA: Canadian Organisation of Medical Physics.

27. Bonnett, D.E., A.J. Farajollahi, and P.F. Harding. *An Investigation Into Wall Materials for Polymer Gel Phantoms.* in *DosGel'99 - Proc. 1st International Workshop on Radiation Therapy Gel Dosimetry*. 1999. Lexington, Kentucky, USA: Canadian Organisation of Medical Physics.

28. Baldock, C., et al., *A Dosimetry Phantom for External Beam Radiation Therapy of the Breast Using Radiation-Sensitive Polymer Gels and MRI.* Med. Phys., 1996. **23**(6): p. 1490.

29. Maryanski, M.J., et al. *Magnetic Resonance Imaging of Radiation Dose Distributions in Tissue-Equivalent Polymer-Gel Dosimeters.* in *Society for Magnetic Resonance in Medicine*. 1994.

30. Oldham, M., et al., *High resolution gel-dosimetry by optical-CT and MR scanning.* Med. Phys., 2001. **28**(7): p. 1436-1448.

31. Jirasek, A.I., et al., *Characterization of monomer/crosslinker consumption and polymer formation observed in FT-Raman spectra of irradiated polyacrylamide gels.* Phys. Med. Biol., 2001. **46**: p. 151-165.

32. Jirasek, A.I. and C. Duzenli, *Effect of crosslinker fraction in polymer gel dosimeters using FT Raman spectroscopy.* Phys. Med. Biol., 2001. **46**: p. 1949-1961.

33. Lepage, M., et al., *^{13}C , ^{1}H NMR and FT-Raman study of the radiation-induced modification in radiation dosimetry polymer gels.* J. Appl. Polym. Sci., 2001. **79**: p. 1572-1581.

34. Lepage, M., et al., *The relationship between radiation-induced chemical processes and transverse relaxation times in polymer gel dosimeters.* Phys. Med. Biol., 2001. **46**: p. 1061-1074.

35. Trapp, J.V., et al., *An experimental study of the dose response of polymer gel dosimeters imaged with x-ray computed tomography.* Phys. Med. Biol, 2001. **46**(11): p. 2939-2951.

36. Audet, C., et al., *CT gel dosimetry technique: Comparison of a planned and measured 3D stereotactic dose volume.* Journal of Applied Clinical Medical Physics, 2002. **3**(2): p. 110-118.

37. De Deene, Y., et al., *Dose-response stability and integrity of the dose distribution of various polymer gel dosimeters.* Phys. Med. Biol., 2002. **47**: p. 2459-2470.

38. Mather, M.L., et al., *Investigation of ultrasonic properties of PAG and MAGIC polymer gel dosimeters.* Phys. Med. Biol., 2002: p. In Press.

39. Maryanski, M.J., C. Audet, and J.C. Gore, *Effects of crosslinking and temperature on the dose response of a BANG polymer gel dosimeter.* Phys. Med. Biol., 1997. **42**: p. 303-311.

40. De Deene, Y. and C. De Wagter. *Gel Dosimetry in Conformal Radtiotherapy: Validation, Optimization and MR Artifacts.* in *DosGel'99 - Proc. 1st International Workshop on Radiation Therapy Gel Dosimetry*. 1999. Lexington, Kentucky, USA: Canadian Organisation of Medical Physics.

41. Pullan, B.R., R.T. Ritchings, and I. Isherwood, *Radiology of the skull and brain: Chapter 111 - Accuracy and meaning of computed tomography attenuation values*, in *Radiology of the skull and brain*, D.G. Potts, Editor. 1981, The C.V. Mosby Company: St Louis, USA. p. 3904-3917.

42. Joseph, P.M., *Radiology of the skull and brain: Chapter 114 - Artifacts in computed tomography*, in *Radiology of the skull and brain*, D.G. Potts, Editor. 1981, The C.V. Mosby Company: St Louis, USA. p. 3956-3992.

43. Joseph, P.M. and R.D. Spital, *A method for correcting bone induced artifacts in computed tomography scanners.* J. Comp. Assist. Tomogr.. 1978. **2**: p. 100-108.

44. Duerinckx, A.J. and A. Macovski, *Classification of artifacts in x-ray CT images due to nonlinear shadows.* IEEE Transactions on Nuclear Science, 1979. **NS-26**(2): p. 2848-2852.

45. Lim, J.S., *Two-dimensional signal and image processing*. Signal Processing, ed. A.V. Oppenheim. 1990, Englewood Cliffs, NJ, USA: Prentice Hall. 694.

46. TPL, *The Phantom Laboratory Catphan Manual*. 1998, The Phantom Laboratory: Salem, USA.

47. Ibbott, G.S., et al., *Three-Dimensional Visualization and Measurement of Conformal Dose Distributions Using Magnetic Resonance Imaging of BANG Polymer Gel Dosimeters.* Int. J. Radiation Oncology Biol. Phys, 1997. **38**(5): p. 1097-1103.

48. Oldham, M., et al., *Improving calibration accuracy in gel dosimetry.* Phys. Med. Biol., 1998. **43**: p. 2709-2720.

49. De Deene, Y., et al., *An investigation of the chemical stability of a monomer/polymer gel dosimeter*. Phys. Med. Biol., 2000. **45**: p. 859-878.

50. Lepage, M., et al., *^{13}C-NMR, ^{1}H-NMR, and FT-Raman Study of Radiation-Induced Modifications in Radiation Dosimetry Polymer Gels.* J. Appl. Polym. Sci., 2000. **79**: p. 1572-1581.

51. Murphy, P.S., et al., *Proton spectroscopic imaging of polyacrylamide gel dosimeters for absolute radiation dosimetry.* Phys. Med. Biol., 2000. **45**: p. 835-845.

52. Attix, F.H., *Introduction to Radiological Physics and Radiation Dosimetry*. 1986, New York: John Wiley & Sons Inc.

53. BP_Amoco, *Barex Barrier Resins Barrier Properties*. 2000, BP Amoco p.l.c.: Naperville, Il, USA.

54. Baldock, C., et al. *Polymer Gel Composition in Magnetic Resonance Imaging Dosimetry*. in *Proceedings of the Fourth Scientific Meeting of the International Society for Magnetic Resonance in Medicine*. 1996. New York, USA.

55. Baldock, C., et al., *Calibration of Gammacell Irradiator for Irradiation of Radiotherapy Polymer Dosimetry Gel.* Med. Phys., 1999. **26**(6): p. 1130.

56. Maryanski, M.J., et al., *Radiation Therapy Dosimetry Using Magnetic Resonance Imaging of Polymer Gels.* Med. Phys., 1996. **23**(5): p. 699-705.

57. Baldock, C., et al. *Investigation of Polymerization of Radiation Dosimetry Polymer Gels*. in *DosGel'99 - Proc. 1st International Workshop on Radiation Therapy Gel Dosimetry*. 1999. Lexington, Kentucky, USA: Canadian Organisation of Medical Physics.

58. Lepage, M., et al., *Modelling of post-irradiation events in polymer gel dosimeters.* Phys. Med. Biol., 2001. **46**: p. 2827-2839.

59. Zacher, R. *Resolution Limits for Reconstruction Tomography Based on Photon Attenuation*. in *Proceedings of the workshop "Reconstruction Tomography in Diagnostic Radiology and Nuclear Medicine"*. 1977. San Juan, P.R.: University Park Press.

60. De Deene, Y., et al., *A basic study of some normoxic polymer gel dosimeters.* Phys. Med. Biol., 2002. **47**: p. 3441-3463.

61. Trapp, J.V., et al., *Dose Resolution of Polymer Gel Dosimeters Imaged by X-ray Computed Tomography.* Med. Phys, 2001. **28**(8): p. 1830.

62. Trapp, J.V., et al., *X-ray computed tomography of gel dosimeters: characterization of gels.* Australas. phys. eng. sci. med, 2000. **23**(4): p. 169.

63. Trapp, J.V., et al. *X-Ray Computed Tomography of Gel Dosimeters: Characterization of Gels*. in *The Annual Conference of Engineering and the Physical Sciences in Medicine*. 2000. Newcastle, Australia.

64. Trapp, J.V., et al. *X-ray Computed Tomography of Polymer Gel Dosimeters*. in *Joint Local Symposium, Australasian College of Physical Scientists and Engineers in Medicine*. 2000. Brisbane.

65. Hubbell, J.H., *Photon cross sections, attenuation coefficients, and energy absorption coefficients from 10 keV to 100 GeV NSRDS-NBS 29.* 1969, US Department of Commerce - National Bureau of Standards.

66. McCullough, E.C., *Photon attenuation in computed tomography.* Med. Phys, 1975. **2**(6): p. 307-320.

67. Trapp, J.V., G. Michael, and C. Baldock. *Uncertainty calculations determined from calibration data for CT imaging of polymer gel dosimeters*. in *Preliminary Proceedings of DOSGEL 2001 - 2nd International Conference on Radiotherapy Gel Dosimetry*. 2001. Brisbane, Australia: Queensland University of Technology.

68. ISO, *Guide to the Expression of Uncertainty in Measurement*. 1995, Geneva: International Organization for Standardization: International Organization for Standardization.

69. Brandrup, J. and E.H. Immergut, eds. *Polymer Handbook*. 1966, John Wiley & Sons: New York, USA.

70. Erdtmann, G. and W. Soyka, *The Gamma Rays of the Radioniclides, Tables for Applied Gamma Ray Spectroscopy*. Topical Presentations in Nuclear Chemistry, ed. K.H. Lieser. 1979, New York, USA: Verlag Chemie.

71. Knoll, G.F., *Radiation detection and measurement.* 3rd ed. 2000, New York: John Wiley & Sons, Inc.

72. Ortec, *Modular Pulse-Processing Electronics and Semiconductor Radiation Detectors*. 1994, EG & G Ortec: Oak Ridge, USA.

73. Tenney, F.H., *Idealized pulse pileup effects on energy spectra.* Nucl. Instrum. Meth., 1984. **219**: p. 165-172.

74. Keall, P. and C. Baldock, *A Theoretical Study of the Radiological Properties and Water Equivalence of Fricke and Polymer Gels Used for Radiation Dosimetry.* Australasian Physical & Engineering Sciences in Medicine, 1999. **22**(3): p. 85-91.

75. Trapp, J.V., et al., *Attenuation of diagnostic energy photons by polymer gel dosimeters.* Phys. Med. Biol. (In Press), 2002(In Press).

76. Mather, M.L., et al., *Investigation of ultrasonic properties of PAG and MAGIC polymer gel dosimeters.* Phys. Med. Biol., 2002. **47**: p. 4397-4409.

77. Baldock, C., et al., *Dose Resolution in Radiotherapy Polymer Gel Dosimetry: Effect of Echo Spacing in MRI Pulse Sequence.* Phys. Med. Biol., 2001. **46**(2): p. 449-460.

78. Trapp, J.V., et al. *Spatial uncertainty of absorbed dose information in 3D polymer gel dosimeters by x-ray computed tomography. In Press*. in *International Symposium on Standards and Codes of Practice in Medical Radiation Dosimetry*. 2002. Vienna, Austria.

79. Trapp, J.V., et al., *Investigation of density and linear attenuation coefficient changes in polymer gel dosimeters.* Med. Phys., 2002. **29**(6): p. 1370.

80. Trapp, J.V., et al. *Photon attenuation and density in polymer gel dosimeters*. in *2002 Local Symposium XII - Physical Sciences and Engineering in Medicine*. 2002. Brisbane, Australia: QUT.

81. Riederer, S.J., N.J. Pelc, and D.A. Chesler, *The Noise Power Spectrum in Computed X-ray Tomography.* Phys. Med. Biol., 1978. **23**(3): p. 446-454.

82. Hanson, K.M., *Radiology of the skull and brain: Chapter 113 - Noise and contrast discrimination in computed tomography*, in *Radiology of the skull and brain*, D.G. Potts, Editor. 1981, The C.V. Mosby Company: St Louis, USA. p. 3941-3955.

83. Cohen, G. and F.A. Di Bianca, *The Use of Contrast - Detail - Dose Evaluation of Image Quality in a Computed Tomographic Scanner.* J. Comput. Assist. Tomogr., 1979. **3**(2): p. 189-195.

84. Brooks, R.A. and G. Di Chiro, *Statistical Limitations in X-ray Reconstructive Tomography.* Med. Phys, 1976. **3**(4): p. 237-240.

85. Chesler, D.A., S.J. Riederer, and N.J. Pelc, *Noise due to photon counting statistics in computed x-ray tomography.* J. Comp. Asst. Tomo., 1977. **1**(1): p. 64-74.

86. Nodes, T.A. and J.R. Gallagher, *Two-dimensional root structures and convergence properties of the separable median filter.* IEEE Transactions on Acoustics, Speech, and Signal Processing, 1983. **ASSP-31**(6): p. 1350-1365.

87. Gallagher, N.C. and G.L. Wise, *A theoretical analysis of the properties of median filters.* IEEE Trans. Acoust. Speech signal process, 1981. **ASSP-29**(6): p. 1136-1141.

88. Chin, R.T. and C. Yeh, *Quantitative evaluation of some edge-preserving noise-smoothing techniques.* Computer Vision, Graphics, and Image Processing, 1983. **23**: p. 67-91.

89. Du Buf, J.M.H. and T.G. Campbell, *A quantitative comparison of edge-preserving smoothing techniques.* Signal Processing, 1990. **21**: p. 289-301.

90. Fram, J.R. and E.S. Deutsch, *On the quantitative evaluation of edge detection schemes and their comparison with human performance.* IEEE Trans. Comput., 1975. **c-24**(6): p. 616-628.

91. Trapp, J.V., G. Michael, and C. Baldock. *Theoretical considerations for scan parameters appropriate for CT imaging of polymer gel dosimeters*. in *Preliminary Proceedings of DOSGEL 2001 - 2nd International Conference on Radiotherapy Gel Dosimetry*. 2001. Brisbane, Australia: Queensland University of Technology.

92. Johns, H.E. and J.R. Cunningham, *The Physics of Radiology*. 4th ed. 1983, Springfield, Il: Charles C Thomas.

93. Oldham, M., et al., *An investigation into the dosimetry of a nine-field tomotherapy irradiation using BANG-gel dosimetry.* Phys. Med. Biol., 1998. **43**: p. 1113-1132.

94. Baldock, C., P. Murry, and T. Kron, *Uncertainty analysis in polymer gel dosimetry*. Phys. Med. Biol., 1999. **44**: p. N243-N246.

95. Low, D.A., et al., *Noise in Polymer Gel Measurements using MRI.* Med. Phys., 2000. **27**(8): p. 1814-1817.

96. De Deene, Y., et al., *Mathematical analysis and experimental investigation of noise in quantitative magnetic resonance imaging applied in polymer gel dosimetry.* Signal Processing, 1998. **70**: p. 85-101.